LA-UR- *09-07275*

Title: | Design Fundamentals for Cost-Optimized Neutron Detectors Based on an Array of Helium-3 Tubes

Author(s): | Randy J. Spaulding

Intended for: | LANL and sponsor-appropriate version of Randy J. Spaulding's Master's Thesis from Idaho State University, LA-UR-09-01860, August 2009.

Los Alamos
NATIONAL LABORATORY
—— EST.1943 ——

Form 836 (7/06)

Design Fundamentals for Cost-Optimized Neutron

Detectors Based on an Array of Helium-3 Tubes

By

Randy J. Spaulding

A thesis submitted in partial fulfillment of the

requirements for the degree of

MASTER OF SCIENCE

IN

PHYSICS

IDAHO STATE UNIVERSITY

August 2009

Acknowledgements

Dr. Chris Morris: Thank you for conceiving the arrayed neutron detector and all the invaluable help and insights you gave me in making it happen. You are a mountain of knowledge and I couldn't have asked for a better example.

Dr. Steve Greene: Thank you for all your knowledge, guidance, reassurance, and especially your ability to deal with the red tape and get things done.

Dr. Frank Harmon: For your years of brilliant guidance and tutelage. I only wish I remembered half the things you taught me.

Dr. Tony Forest, Dr. Phil Cole, and Dr. George Imel: Thank you so much for being on my graduate committee. Lest I forget, Dr. Alan Hunt for almost being on my committee.

Jeffrey D. Bacon: For always knowing where to find it and always knowing what "it" was when I didn't. Bacon! Bacon! Bacon!

Daren Norman: For all the discussions we had and your insights that planted the seed for the chapter on efficacy. I hope you are as glad as I am to see them finally came to fruition all these years later.

To everyone at P-25, D-5, and LANSCE: you guys rock! There is definitely a reason you hold the positions you do.

To my parents, brothers, and their families: For being there any time I just needed someone positive to talk to.

To my children: For putting up with me through all of this. I genuinely regret not being more available throughout this process, but I can also promise you the sacrifices were well worth it. Hopefully I'll be able to help to put up with your own graduate work someday.

Finally, most important of all, my girlfriend Sherrie: thank you so much for being who you are and for all the joy you bring into my life. Words can truly never express how much you mean to me.

Just think, we (only) have to go through this one more time. God help us all!

Table of Contents

List of Figures

List of Tables

Dedication

To all those who think they lack the talent, or think they are

getting too old and have forgotten too much, or just can't

seem to find the desire and drive anymore:

Shut up and DO IT. I was there, and I did it. True, it wasn't fun

a lot of the time, but there truly is no better feeling of satisfaction

than through accomplishment.

Abstract

Helium-3 gas has long been a popular medium for neutron detection because of its enormous 5320 barn thermal cross-section. Unfortunately, helium-3 does not naturally occur in significant quantities on Earth. Increasing competition over the world's finite helium-3 reserves has recently created an urgent need to utilize our existing supplies of the gas in the most efficient manner possible. A concept called cost efficiency is introduced to quantify this. In cost efficiency, the amount of helium-3 gas used and geometric constraints are considered costs and detector efficiency is considered a return-on-investment. Two figures of merit (FOM) are introduced to compare the cost efficiency of various detector designs.

A new design concept for moderating neutron detectors has been developed at Los Alamos National Laboratory (LANL). This design uses an array of detectors nestled inside a polyethylene lattice. This design is demonstrated to provide an increase in cost efficiency of a factor of 2.5 to 3.5 over previous systems. In this thesis, low-pressure helium-3 drift tubes are compared to the high-pressure tubes currently in widespread use. However, the concept can be applied to many other types of detectors as well.

A prototype detector containing 72 low-pressure helium-3 tubes was constructed at LANL for benchmarking purposes as well as supporting standoff interrogation experiments. A semi-deterministic method for quantifying detector responses to environmental neutron scattering, called efficacy, is introduced as a means of customizing detector implementations for specific open-laboratory

applications such as standoff interrogation. This thesis reports the results of several

benchmarking tests to compare empirical detector performance with the predictions

of the Monte-Carlo program MCNPX. The overall goal of this thesis is to illustrate a

detector design concept which maximizes the utilization of high-cost and/or rare

detection media such as helium-3.

Chapter 1 : Introduction

1.1 History of the Neutron

The discovery of the neutron is credited to J. Chadwick in 1932. Chadwick was following up on an observation made by I. Curie-Joliot and F. Joliot in 1931; in 1930, Bothe and Becker had first produced radiation that they assumed consisted of "very penetrating gamma rays" by bombarding light elements such as boron and beryllium with polonium alpha rays. Curie-Joliot and Joliot placed sheets of paraffin in the path of this yet-unknown radiation, which produced radiation that behaved like energetic protons. The photon energy they calculated to produce these assumed protons through a process similar to the Compton effect was an unrealistic 55 MeV. Chadwick confirmed that these were indeed protons and postulated that they were being produced by massive, energetic particles having a neutral electric charge instead of photons. The lack of electric charge of these "neutrons" explained their ability to penetrate matter with little absorption [1].

Unfortunately, the lack of electric charge also makes it impossible to measure the mass of the neutron using a conventional mass spectrometer. It was not until two years later in 1934 that Chadwick and Goldhaber were able to first measure the mass of the neutron by splitting deuterons with Thorium gamma-rays [2]. The neutron rest mass, now commonly used as a physical mass reference constant[1], is

$$m_n = 1.6749286 \times 10^{-24} \text{ g}.$$

---

[1] In the modified nuclear system of units commonly used in computer codes, the neutron mass is defined to be equal to 1 mass unit. In this system, the mass of carbon-12 equals 11.8969142 units and Avogadro's number is 5.9703109×10^{23} [3].

UNCLASSIFIED – ADC Review by Alexander Saunders, P-25, on 3/23/2009

1.2 Neutron Detection

The very long interaction length resulting from the zero net electric charge of the neutron also makes it very difficult to detect them directly. However, neutrons do have a significant cross-section for many nuclear interactions such as elastic scattering, inelastic scattering, (n, γ), (n, p), (n, n'), $(n, \text{fission})$ etc. Neutrons are easily detected via interactions of the secondary charged particles produced during one of the preceding nuclear reactions.
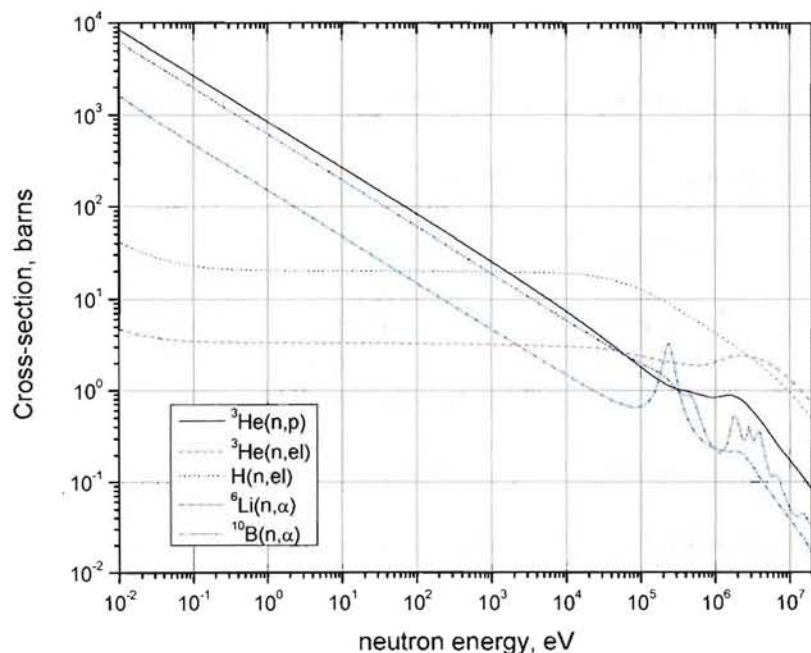
Figure 1: Cross section versus neutron energy for several common neutron-detection processes. Data retrieved from ENDF web site [13] on 7/28/2009.

Figure 1 shows the cross-section for several of the most common reactions used in neutron detection. The strong energy dependence shown by these examples is characteristic of all neutron interactions.

1.2.1 Some examples of neutron detectors

The reaction products from a neutron-induced reaction are detected either in real time via direct charge conversion, or offline, by activation of a sample and monitoring of its radioactive decay [4]. Charge-conversion methods are predominant in most nuclear experiments because they give immediate or near-immediate results, while activation techniques [3] remain popular for small-scale experiments, high-radiation environments, and applications where the neutron spectrum needs to be known, such as boron-neutron capture therapy (BNCT) [6]. This document will focus on a handful of the real-time techniques that offer the highest practical detection efficiencies for epithermal neutrons; see reference [4] for a more complete discussion.

Reactions whose cross-sections dominate at low neutron energies can be used effectively for detecting high-energy neutrons by adding moderating material around the detector. The moderating material slows the neutrons down through multiple scattering events. The energy lost by the neutron in scattering from a nucleus of mass A is readily calculated from kinematics:

$$\frac{E'}{E} = \frac{A^2 + 1 + 2A\cos\theta}{(A+1)^2} \qquad (1.1) \quad [8]$$

where E is the initial energy of the incident neutron, E' is the final energy, and θ is the scattering angle in the center-of-mass frame. The relationship between energy loss and mass of the nucleus is more apparent when this equation is rewritten as:

$$\Delta \equiv 1 - \frac{E'}{E} = \frac{2A}{(A+1)^2}(1 - \cos\theta) \qquad (1.2)$$

Equation (1.2) shows that the energy transfer decreases as atomic mass

---

UNCLASSIFIED – ADC Review by Alexander Saunders, P-25, on 3/23/2009

increases ($\Delta \propto 1/A$). Thus, light nuclei, in particular hydrogen, make the most effective neutron moderators, as they remove a greater fraction of the incident neutron's momentum per collision. This form also shows that the maximum energy loss occurs when $\theta = \pi$ (pure backscattering) and no energy transfer occurs for $\theta = 0$ (no collision). The most popular moderating material is polyethylene (($CH_2)_n$), or PE. PE has a density similar to water (~0.89-0.97 g/cm^3) and is rich in hydrogen content (14% by mass). PE is substantial enough to be an effective moderator while being less bulky than heavy metals and easier to handle in the laboratory than water or liquid hydrogen. It is also inexpensive to produce and machine. The density of polyethylene increases as the average length of the ethylene chains grows. Polyethylene sold commercially is sorted by chain length and categorized by density. High-density polyethylene (HDPE) obtained in such fashion typically has a guaranteed average density of 0.93-0.95 g/cm^3.

1.2.1.1 Scintillator-based neutron detectors

A scintillator is a material that fluoresces when bombarded with ionizing radiation. Many materials scintillate, including various aromatic liquids, amorphous solids such as plastics and glasses, and inorganic crystals such as NaI and CsI. All of these materials detect ionizing radiation in the same fashion; the total optical energy produced is directly related to the energy transferred to the scintillator. The optical photons are then collected and converted into an electrical signal by a photomultiplier tube (PMT).

Organic and other hydrogenous scintillators are inherently sensitive to neutrons because of the large cross-section of the n-p elastic scattering reaction (denoted H(n, el) in Figure 1). They are thus called proton recoil detectors. See Figure 2. Scintillators can also be combined with a neutron-sensitive material such as gadolinium, boron-10, or lithium-6, all of which have large cross-sections for thermal neutrons[2]. These are referred to as doped scintillator detectors.

Neutron detection with scintillators is a highly-efficient process. However, scintillator detectors are also sensitive to all other forms of ionizing radiation, and thus any incident flux of gammas, betas, etc. can create a large background which competes with the neutron signal. The inclusion of appropriate high-Z shielding materials around the detector can reduce the background, as such materials absorb photons and charged particles but are highly transparent to neutrons. Additionally, in some cases the neutron signals can be separated from the gammas and betas by pulse-

---

[2] In this document, "thermal" neutrons refers to $T = 293.15K$ ($kT = 0.02526174$ eV)

shape discrimination techniques. Efficiencies in the epithermal and fast regimes (E_n >~1 keV) are on the order of 30-50% [9][3]. Efficiencies in the thermal regime for doped scintillators can effectively reach 100% [11, 12].
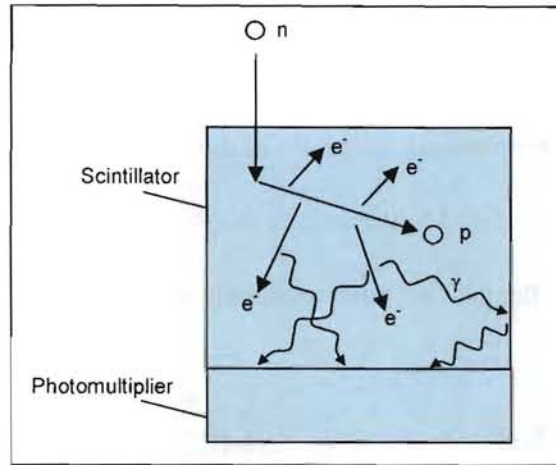
Figure 2: Organic scintillation detectors detect fast neutrons via proton recoil.

1.2.1.2 Helium-3

Helium-3 is a monatomic gas having density 0.134×10^{-3} g/cm^3 at standard temperature and pressure (STP). The He-3(n, p)t reaction has a cross-section of 5320 barns [13] for thermal neutrons--fourth-greatest among the stable nuclides behind only Gd-157 (2.54×10^5 bn), Gd-155 (6.09×10^4 bn), and Eu-151 (9.2×10^3 bn) [14]. The large cross-section and modest energies of the daughter particles make He-3 an ideal candidate for use in gaseous detectors. The helium-3 gas is typically mixed with a proportional gas and possibly also a quench gas to improve signal-to-noise and stabilize the Townsend avalanche. Historically, detectors have been typically

---

[3] The theoretical efficiency for direct detection of fast neutrons with plastic scintillator is as high as 90%. Imperfect discrimination of gamma-rays reduces the effective efficiency considerably [10].

---

operated at a pressure of 2-10 bar[4] to maximize neutron detection efficiency.

However, this practice is very wasteful of the He-3 gas because of decreasing returns

in efficiency as pressure is increased (see Figure 7 on page 20). There is a significant

ongoing effort at Los Alamos National Laboratory (LANL) studying the use of

atmospheric-pressure tubes containing a few hundred mbar of helium-3 in hopes of

reducing this wastefulness on a widespread scale[5].
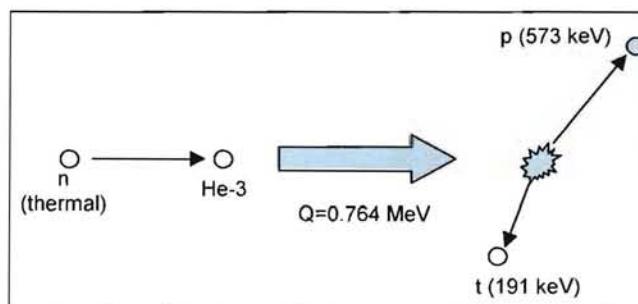
Figure 3: The ^{3}He(n,p)t reaction for thermal neutrons

---

[4] In the CGS system of units, 1 bar = 10^5 Pa = 1 / 1.01325 atm.

[5] See §1.3 and §1.3 for a full discussion.

UNCLASSIFIED – ADC Review by Alexander Saunders, P-25, on 3/23/2009
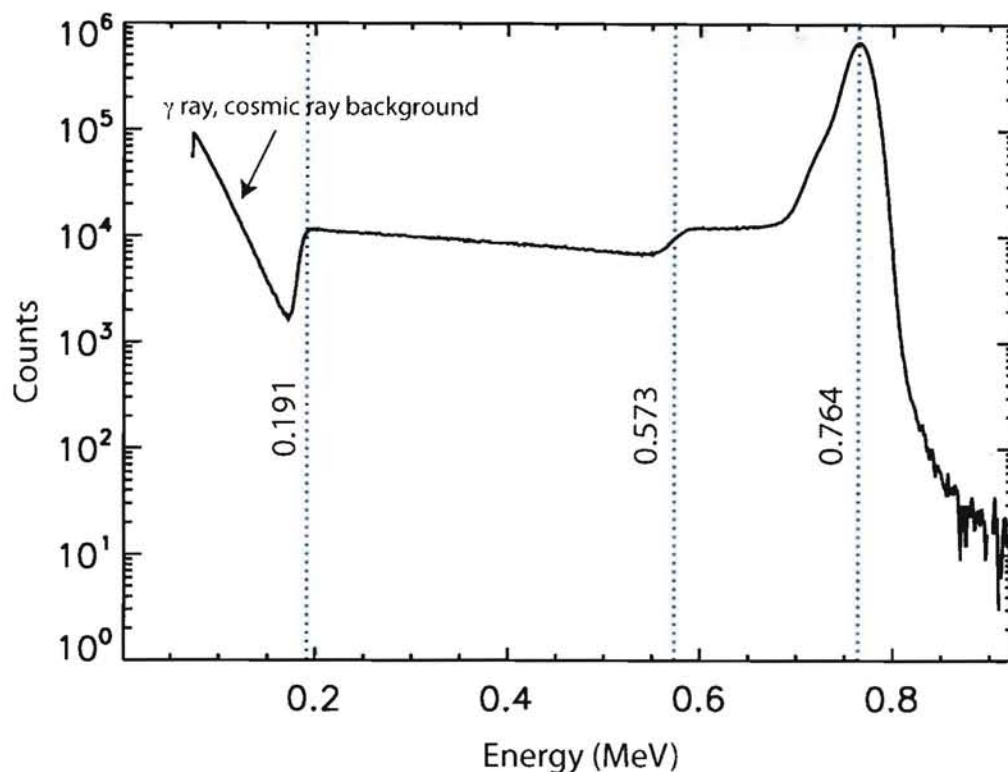
Figure 4: Energy spectrum of 2"-dia. x 48"-long detector containing 200-mbar He-3 and 800-mbar proportional gas. Neutron counts appear above 191-keV and background counts from gamma-rays, cosmic rays, and electronic noise appear at lower energies, as indicated. Wall effects from both p (573 keV) and T (191 keV) daughters are clearly resolved.

Figure 4 shows an energy spectrum from an atmospheric-pressure detector containing a mixture of He-3 and proportional gas. The proportional gas produces a sharp full-energy peak having a full-width-at-half-maximum (FWHM) ~5% [15]. The low-energy background peak is produced by electronic noise, gamma-rays, and cosmic-ray muons and is typical of all gaseous detectors. The two "shelves" at 191-keV and 573-keV are produced when one of the energetic daughter particles (proton or triton, respectively) intersects the wall of the tube and does not deposit its entire energy in the gas. These shelves are referred to as wall effects. The energetic proton

from the He-3 reaction has a range of ~1.5 cm in atmospheric-pressure tubes, while

the triton's range is ~0.5 cm. These wall effects, which are present in all gaseous

neutron detectors, cause a minor loss in counting efficiency, as counts that do not

contribute to the full-energy peak could be lost in the noise/cosmic-ray background

peak that appears at low energies. This is not a great concern for a fairly new tube, as

the wall effects represent a small fraction of the total counts and the background is

easily discriminated out. However, the noise level tends to increase as the tube ages

because of effects such as gas spoiling, or gradual replacement of the proportional gas

with air by leakage and diffusion through the wall of the tube. Gas spoiling also

causes wall effects to increase slightly because the air is less dense and has less

stopping power than the proportional gas. Consequently, the range of the charged

particles increases as proportional gas is lost. Researchers at LANL are currently

developing techniques that will be applicable to all gaseous proportional counters, to

monitor the health of the tube and predict its remaining lifetime [15].

1.2.1.3 Boron-10

Boron-10 is another popular medium for thermal neutron detection due to its

high cross-section (3845 bn [13]) and high Q-value (see Figure 5). As depicted in the

figure, the B-10(n,α)Li-7 reaction can populate either the ground state of the Li-7 ion

or the first excited state. In the latter case, the excited Li-7 nucleus immediately

decays to ground[6], emitting a 477-keV gamma ray. Boron-10 is only 19.9% abundant

---

[6] The half-life of the first Li-7 excited state is 73 fs [12].

in natural boron, the remainder being Boron-11. For this reason, it is typical to use isotopically-enriched boron-10 in neutron counters.
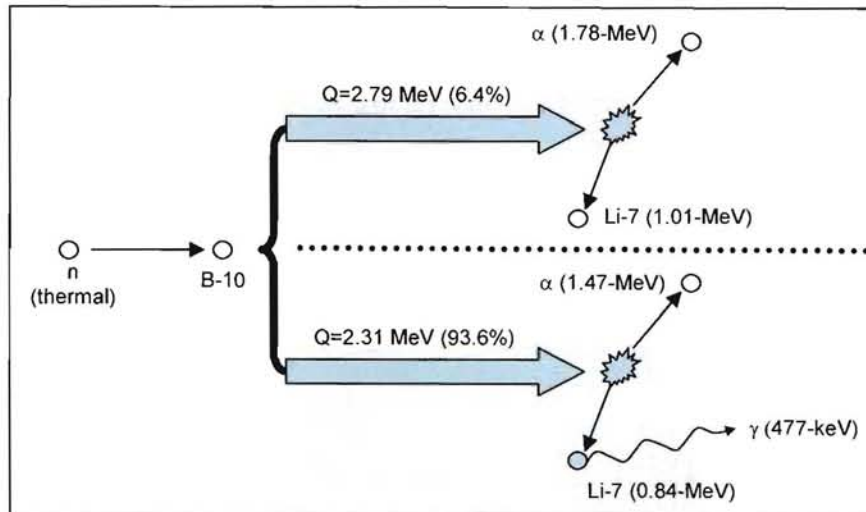
Figure 5: Thermal neutron capture on Boron-10

Boron is used for neutron detection in several schemes involving both solid and gaseous forms [4]. The most common form used is gaseous boron triflouride (BF$_3$). BF$_3$ used for this purpose is typical enriched in B-10 to near 100%. At STP, (B-10)F$_3$ has a density of 2.99 x 10^{-3} g/cm^3 at STP at and contains 14.9% B-10 by mass. The sensitivity of gaseous BF$_3$-filled detectors is somewhat lower than that of He-3. However, Stokes, Meal, and Myers showed that BF$_3$ detectors are particularly radiation-resistant and can be operated in gamma fluxes of 1000 R/hr or more [17], making them attractive for mixed-waste and reactor applications.

1.2.2 Detector Efficiency

The concept relating the measured count rate in an experiment to the current of interacting incident particles present is called efficiency[7]. There are several methods of defining detection efficiency; the terminology used in this document for the most common definitions will be: a) conversion efficiency, b) intrinsic efficiency, and c) total efficiency. Another quantity commonly used by commercial detector manufacturers is sensitivity, which is defined as counts per second per unit incident particle flux. Many of these quantities involve assumptions about the energy and/or angular distribution of the incident particles, as will be explained in following sections.

Conversion efficiency refers to the ability of a detection system to convert the energy from a reaction into recordable signals, and is defined by:

$$\varepsilon_C(E) \equiv \frac{\#\text{ of usable signals produced}}{\#\text{ of interactions involving particles having energy } E} \leq 1$$

Conversion efficiency is thus the probability of obtaining a useful signal each time the desired reaction occurs. Written another way, conversion efficiency equals unity less losses to various processes:

$$\varepsilon_C(E) = 1 - \sum(\text{losses to electronic noise}) - \sum(\text{losses to background}) - \sum \text{other losses}$$

Conversion efficiency plays a fundamental role in determining the count rate from a nuclear experiment. In general, the contribution to the count rate dC in a

---

[7] The reader should continually keep in mind that the context of this development is emphasized toward detection of high-energy neutrons from active-interrogation methods, although much care has generally been taken to present the concepts in a way applicable to all nuclear counting experiments.

volumetric detector for particles having energy between E and E + dE in the volume

element dV is the reaction rate dR times the conversion efficiency, or:

$$dR = N(\vec{r}) \cdot \frac{d\sigma}{dE}(E) \cdot \Phi(\vec{r}, E) dE dV \qquad (1.3)\ [4]$$

$$dC = \varepsilon_c \cdot dR = \varepsilon_c(E) \cdot N(\vec{r}) \cdot \frac{d\sigma}{dE}(E) \cdot \Phi(\vec{r}, E) dE dV \qquad (1.4)$$

where $N(\vec{r})$ = number of target atoms per unit volume

$\dfrac{d\sigma}{dE}$ (E)   = reaction cross-section at energy E

$\Phi(\vec{r}, E)$ = flux per unit energy interval, defined as

$$\Phi(\vec{r}, E) \equiv v \cdot n(\vec{r}, E) \qquad (1.5)\ [7]$$

where $n(\vec{r}, E)$ = number density, the number of particles of interest per unit volume,

and v is the velocity of the particles.

In practice, determination of the conversion efficiency can be quite

complicated, as most physical detectors employ multiple energy conversion schemes

to produce the final signal and many of the reactions themselves involve multiple

chains, e.g. B-10 (n, α) {Li-7, Li-7*}. Thus, experimenters frequently neglect direct

determination of the conversion efficiency. However, it should not be neglected

when monte-carlo particle transport codes such as MCNPX[8] are used, as these codes

typically only estimate the reaction rate—not the actual count rate in the detector. In

many cases, the losses are small and ε_c can be assumed to be equal to or near unity

over the entire applicable energy range. The detectors described in this document

generally all fit this requirement.

---

[8] See § 3.1 for a description and discussion of the MCNPX code.
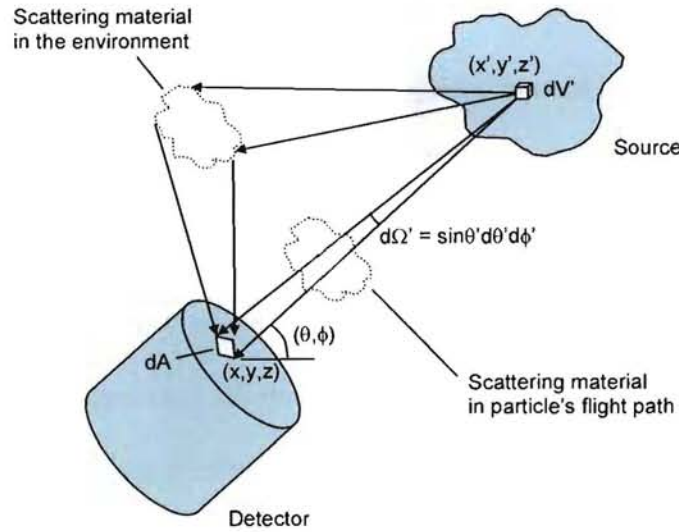
Figure 6: Detection of particles in a nuclear physics experiment

The total efficiency, ε_T, and the intrinsic efficiency, ε_I, are inherently related

quantities describing the count rate for a particular experimental configuration. Total

efficiency is defined as counts per particle emitted from the source, while intrinsic

efficiency is defined as counts per particle crossing the detector boundary. In the

broadest sense, the relationship between the two involves the angular emission

characteristics of the source; the geometry of the experiment, including the physical

sizes and placement of source and detector; and the presence of scattering materials in

the flight path of the particle and the environment:

$$\varepsilon_T(E) \equiv$$

$$\frac{\int dV' d\theta' d\phi' dA \cdot \varepsilon_I(E',\vec{r},\theta,\phi) \cdot \Im(E,E',\theta',\phi',\theta,\phi) \cdot \frac{\partial^2 I}{\partial\theta'\partial\phi'}(E,\vec{r},\theta',\phi')}{\int \frac{\partial^2 I}{\partial\theta'\partial\phi'}(E,\vec{r},\theta',\phi') dV' d\theta' d\phi} \qquad (1.6)$$

where I is the source emission rate of particles originating from the point (x', y', z'),

having energy E, into the cone $d\Omega' = \sin\theta'd\theta'd\phi'$; ε_I, the intrinsic efficiency, is the

fraction of particles having energy E', crossing the point (x, y, z) on the detector's

surface, at the angles of incidence θ and ϕ, that create useful signals in the detector;

and $\Im(E,\theta,\phi,E',\theta',\phi')$ is the transfer function that envelops all interactions

experienced by the source particles during their flight from the source to the detector

(see Figure 6). The transfer function accounts for attenuation and up- or down-

scattering during transmission; environmental effects such as off-angle particles

scattered toward the detector; secondary particle production; etc. In this form, the

integral in the numerator is over the source volume, all source angles, and the detector

surface area. The integral in the denominator is over the source volume and all

source angles. The latter integral is written out explicitly to emphasize that, in order

to achieve the proper normalization of "per source particle" one must normalize to the

total source activity. Note that $|\Im|$, the magnitude of the scattering function, can be

>1, particularly for showers created by high-energy particles, representing

multiplication of the source particles by reactions such as (n, xn).

Equation (1.6) represents the formal relationship between ε_T and ε_I. In

practice, nearly all nuclear physics experiments employ a general strategy of reducing

the effects of finite source size and scattering objects, both in-flight-path and

environmental, to negligible levels or eliminating them entirely. When this is true,

the above expression can be greatly simplified to the form:

$$\varepsilon_T(E) = \varepsilon_I(E) \cdot \frac{\Omega_{sd}}{4\pi} \tag{1.7}$$

or alternatively, for small solid angles:

$$\varepsilon_T(E) = \varepsilon_I(E) \cdot \frac{A}{4\pi R^2}, \qquad \pi R^2 \gg A \tag{1.8}$$

where Ω_{sd} is the solid angle of the volume source subtended by the detector, A is the

surface area of the detector, and R is the distance to the source. As shown by

Eq.(1.8), if the detector is small relative to the square of the source distance, the

fractional solid angle is well approximated by the ratio of the projected area of the

detector to the surface area of a sphere having radius R. This assumption goes hand-

in-hand with one of the assumptions used in writing Eq.(1.7), that angular effects at

the detector surface are negligible. In practice, efficiency is further simplified by

averaging the convolution of the detector's efficiency and the energy spectrum of the

source over the applicable energy range, so that the efficiency can be conveniently

quoted by a single number[9]:

$$\overline{\varepsilon_{T,I}} \equiv \frac{\int \varepsilon_{T,I}(E) \cdot \frac{d\Phi}{dE}(E)dE}{\int \frac{d\Phi}{dE}(E)dE} \tag{1.9}$$

---

[9] Note on terminology: whenever the term 'efficiency' appears by itself throughout
the remainder of this document, it refers to the average intrinsic efficiency of Eq.(1.9)

UNCLASSIFIED – ADC Review by Alexander Saunders, P-25, on 3/23/2009

1.2.3 Note on calibration using check sources

The experimenter often desires to measure detector efficiency directly by means of a calibrated standard source. For fast neutron measurements with filled-gas-tube detectors such as He-3 and B-10, information about the source neutron's energy is generally lost before detection. As a direct result, it is only possible to measure the flux-convoluted average efficiency as in Eq. (1.9). When doing so, the experimenter must keep in mind that the energy spectrum of the neutrons present in the experiment can be, and generally is, quite different from that of the source used in the calibration. A nonuniform detector response over the applicable energy range can result in the experimental efficiency being different from the calibrated efficiency. This is typically the case for gas-tube detectors. See Figure 56 on page 106 for some examples of energy-efficiency curves. Depending on the application, it may sufficient to simply make note of awareness of this situation. However, for applications that require precise knowledge of the efficiency, it is crucial to quantify this effect by introducing a source-correction factor:

$$\overline{\varepsilon_{l\,exp}} = \gamma_\varepsilon \cdot \overline{\varepsilon_{l\,src}}$$

$$\gamma_\varepsilon \equiv \frac{\int dE \cdot \left[\Phi_{exp}(E)\right] \cdot \varepsilon_l(E)}{\int dE \cdot \left[\Phi_{src}(E)\right] \cdot \varepsilon_l(E)} \qquad (1.10)$$

where Φ_{exp} is the experimental neutron energy spectrum and Φ_{src} is that of the source. The square brackets in Eq. (1.10) denote that the energy spectra are required to have the same normalization—both are typically normalized to unity.

Determination of Φ_{exp} and subsequently, γ_ε, is commonly performed by

Monte-Carlo computer simulations. Some example calculations comparing several

neutron energy spectra to a Cf-252 standard are presented in Table 1. These

calculations do not assume to be representative of all situations an experimenter will

encounter in the laboratory; they merely demonstrate that γ can easily vary over a

wide range that spans at minimum $0.56 < \gamma < 1.72$ [18].

Source Description	Source Correction Factor, γ (all ±5%)
Cf-252	1.00
^{238}U ($n_{epithermal}$, fission)	0.560
AmBe	0.958
800-MeV protons on ^{238}U target (room return)	1.720
800-MeV protons on ^{238}U target (delayed neutrons)	1.444

Table 1: Typical source correction factor values from LANL experiments

In Table 1, the ^{238}U epithermal fission spectrum is presented for comparison

purposes only. The two values from 800-MeV protons are taken from different

periods of time within the same experimental setup. The "room return" value

represents $1\,\text{ms} < t < 20\,\text{ms}$ and the "delayed neutron" value was taken from

$100\,\text{ms} < t < 20\,\text{s}$. The 20% difference between the two demonstrates the added

complexity of source correction effects in active interrogation experiments.

Obviously, great care must be taken when calculating neutron yields from such

experiments.

1.3 Maximizing the efficiency cost factor for He-3 tubes

Historically, use of He-3 drift tubes in the laboratory has been governed by the mantra "maximum efficiency in minimum space." This has driven manufacturers to produce tubes containing as much as 40 atm He-3 [42]. Unfortunately, such high pressures result in inefficient use of the He-3 gas due to processes such as self-shielding and increased background stemming from increased n-^{3}He elastic scattering and increased sensitivity to gamma-rays and charged particles.
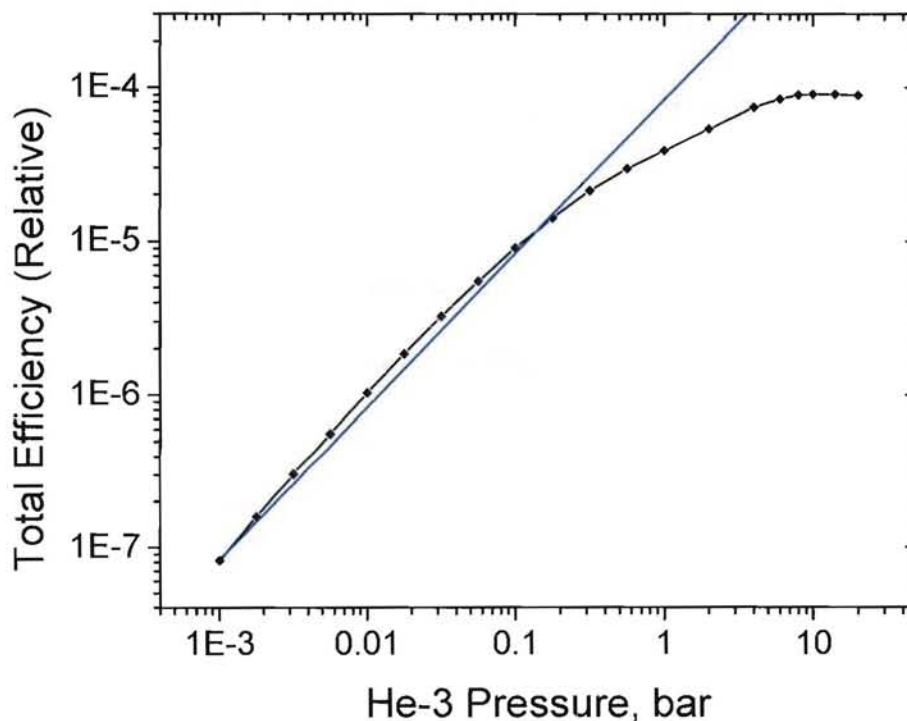
Figure 7: Efficiency of a 1" x 12" cylindrical He-3 detector versus He-3 partial pressure predicted by MCNPX. The straight line represents proportionality. At low pressures the tube is filled to 1 bar with a proportional gas consisting of Argon, CF$_4$, and ethane (C$_2$H$_6$). The slope of the curve is greater than unity at very low pressures due to improved moderation provided by the fill gas itself. Statistical error bars are less than 1%.

$$\text{FOM} = \varepsilon^m / p_{He\text{-}3}$$
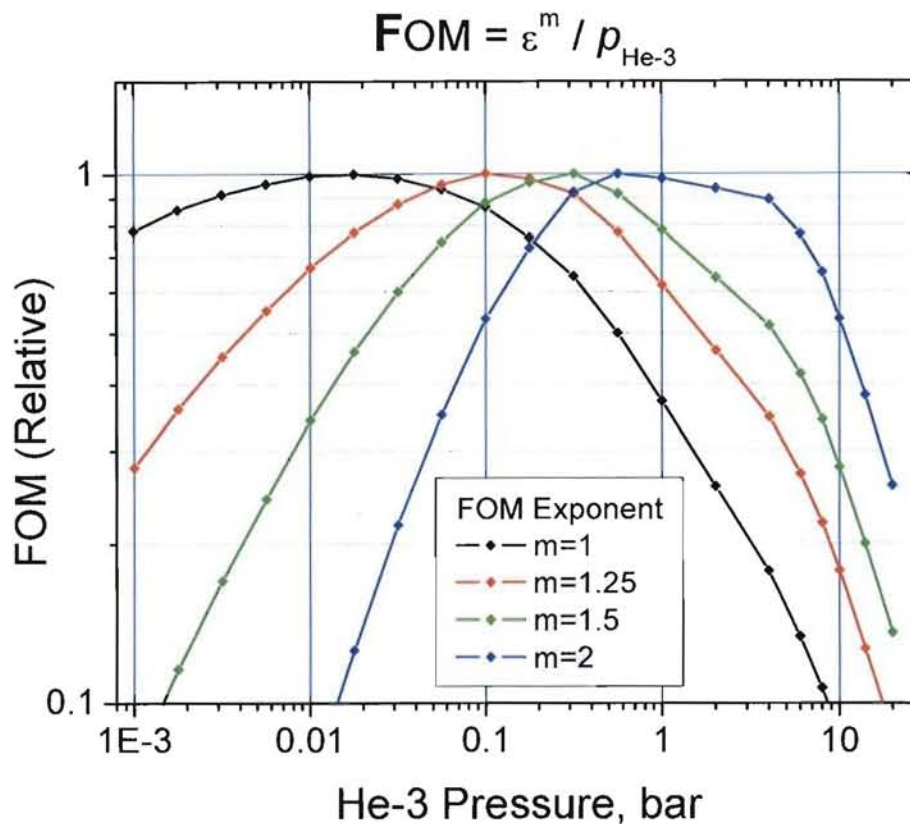
Figure 8: Efficiency of a 1" x 12" cylindrical He-3 detector versus He-3 partial pressure in terms of cost efficiency. The efficiency figure-of-merit (FOM) used in cost efficiency is defined as weighted efficiency per unit He-3 gas. The exponential weighting factor m controls the relative emphasis between efficiency and amount of gas used. Statistical error bars are less than 1%.

Figure 7 demonstrates the decreasing return in efficiency as helium-3 pressure

is increased for a typical cylindrical research detector used at LANL. To emphasize

the situation, a figure-of-merit (FOM) is developed that relates the efficiency, ε, to

the partial pressure of helium-3 gas in the tube, $\rho_{He\text{-}3}$. This FOM is referred to as

cost efficiency. The *m*=1 case in Figure 8 represents equal priority given to the

intrinsic efficiency and the quantity of gas used. The optimal partial pressure of He-3

in this regime is $P_{He\text{-}3} < 100$ mbar. Figure 7 shows that the intrinsic efficiency in this

scenario is at least a factor of 10 less than traditional high-pressure He-3 tubes. Thus, one geometric interpretation of this scenario assumes that total efficiency requirements can be satisfied by increasing the detector's active area indefinitely. Values of m greater than unity represent increased emphasis on efficiency over amount of gas used. At the high end of the scale, $m>2$ represents the traditional viewpoint that the amount of He-3 used is of no importance at all. This scenario is not without merit; constraints on laboratory space typically limit the size of detectors so that maximizing the volumetric count rate is crucial. However, this is not feasible for large-area detectors such as those required for standoff interrogation applications because (1) the cost of packing more gas into the tubes outweighs the cost of adding additional detectors, and (2) the amount of He-3 required to deploy such a high-pressure detector system nationwide simply does not exist terrestrially. However, traditional single-tube detector designs are not efficient enough at low pressures to satisfy count rate requirements. This dilemma prompted LANL researchers to search for a new detector design that can better meet both requirements.

1.3.1 Track length and the arrayed detector[10] concept

Monte carlo computer codes employ the concept of track length in estimating particle flux in a volume as in Eqs. (1.3) and (1.4). Using (1.5) and $ds = vdt$, the time-integrated flux is given by:

---

[10] Important terminology distinction: the term 'detector' is confusing as it can refer to anything from a single counter to a huge assembly consisting of hundreds of counters involving multiple particle species. To avoid confusion, every effort has been made throughout this document to limit the use of the word 'detector' to an entire assembly of shielding, moderation, and counters. Individual He-3 proportional counter are referred to as 'tubes.'

$$\iiint_{V,E,t} \Phi(\vec{r}, E, t) \cdot dt \cdot dE \cdot \frac{dV}{V} = \iiint_{V,E,t} n(\vec{r}, E, t) \cdot ds \cdot dE \cdot \frac{dV}{V} = T_l/V \qquad (1.11) \quad [7]$$

where T_l is the total track length, or the total distance traveled by all particles of

interest throughout the volume. It is important to note that T_l includes reentrant

tracks as well as secondary tracks made by particles produced in the volume.

Therefore, there is an alternative to the classical method of increasing the count rate;

instead of increasing N in (1.3) and (1.4) by packing more gas into the tube, increase

T_l by causing the neutrons to pass through the tube several times and/or pass through

multiple tubes. This is accomplished by placing an array of He-3 tubes inside a

lattice of material having a high neutron albedo[11] and good moderating

characteristics. The most effective moderating/reflecting materials are HDPE and/or

carbon (see Figure 9).
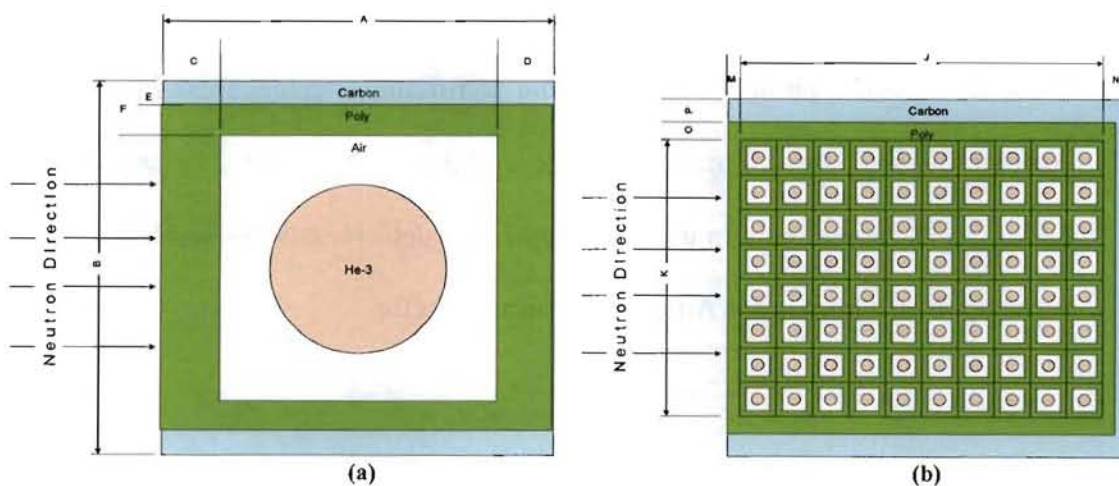
Figure 9: (a) Lattice cell containing a single He-3 tube, and (b) lattice configuration including an outer carbon reflector.

---

[11] In nuclear applications the term *albedo* describes the fraction of incident particles that are reflected from an object's surface.

In this design, the thickness of the separating layers between the cells, or separators (C and D in Figure 9) is chosen so there is a 20-30% chance of reflection from each layer (roughly 1-2 g/cm2 for HDPE or 2-5 g/cm2 for Carbon, see Figure 10). The neutrons are thus allowed to penetrate several layers within the detector before losing a significant fraction of their initial kinetic energy. Figure 11 shows that the albedo increases after each collision due to the energy loss. Thus, the neutrons are effectively trapped within the interior of the lattice. Once trapped inside, the neutrons continue to scatter from the walls, passing through the helium-3 tubes multiple times while thermalizing gradually. The neutrons ultimately either escape or are absorbed in one of the He-3 tubes or captured by a hydrogen atom[12]. The outer walls of the detector (with the exception of the front face) are made quite thick to minimize neutron loss by escape.

The enormous increase in track length allows the experimenter to use relatively low He-3 partial pressure without sacrificing detector efficiency. The detector thus makes much more efficient use of the gas in the detector, as shown in Figure 7. The common term used to refer to such detector designs is ANDY, which is based upon an acronym for ArraYed Neutron Detector.

---

[12] The neutrons can also be captured by atoms in the air or the tube constituents; however, these effects are negligible compared to hydrogen capture $H(n, \gamma)d$. The fraction of neutrons lost in this fashion is briefly discussed in following chapters.
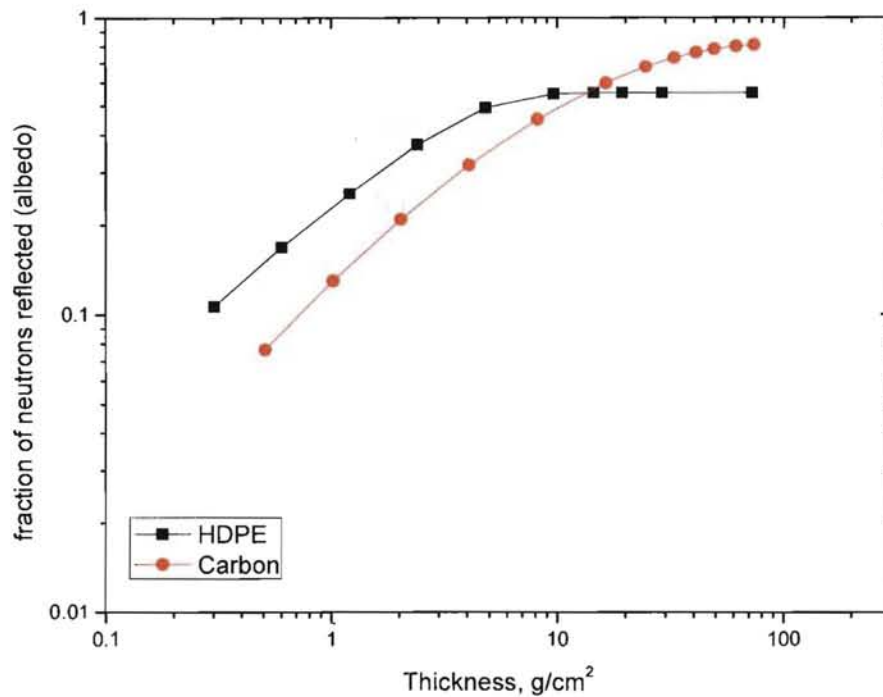
Figure 10: Neutron albedo for HDPE and Carbon slabs. The albedo increases monotonically with thickness and eventually saturates. The incident neutron field was a semi-isotropic Watt fission spectrum from thermal neutrons on U-235: $f(E) = C\exp(-E/0.988)\sinh(2.249E)^{1/2}$
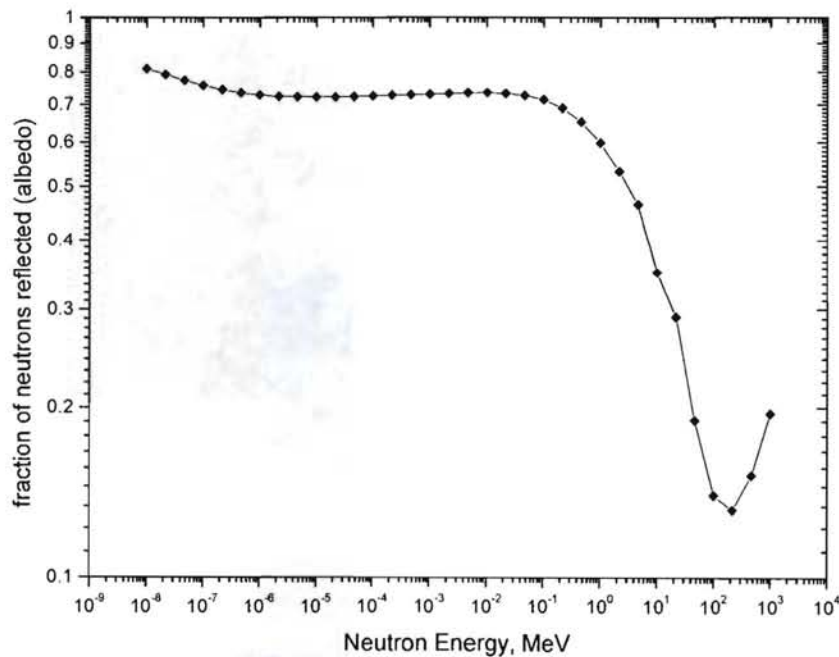
Figure 11: Neutron albedo versus incident neutron energy for an infinite HDPE slab.

1.4 Motivation for this work

The goals of traditional portal monitoring systems are to monitor and control

the movement of specific items throughout the country, and on a larger scale,

worldwide. In this modern era of heightened terrorist activity, systems such as these

have become pivotal in keeping the world's people, governments, and economies safe

and providing peace of mind for the general public. Of particular interest is the

possible threat of a nuclear attack on United States soil. Prevention of such an attack

requires (1) the detection of the Special Nuclear Material (SNM) in a safe and

effective manner and (2) interception and neutralization of the material before it
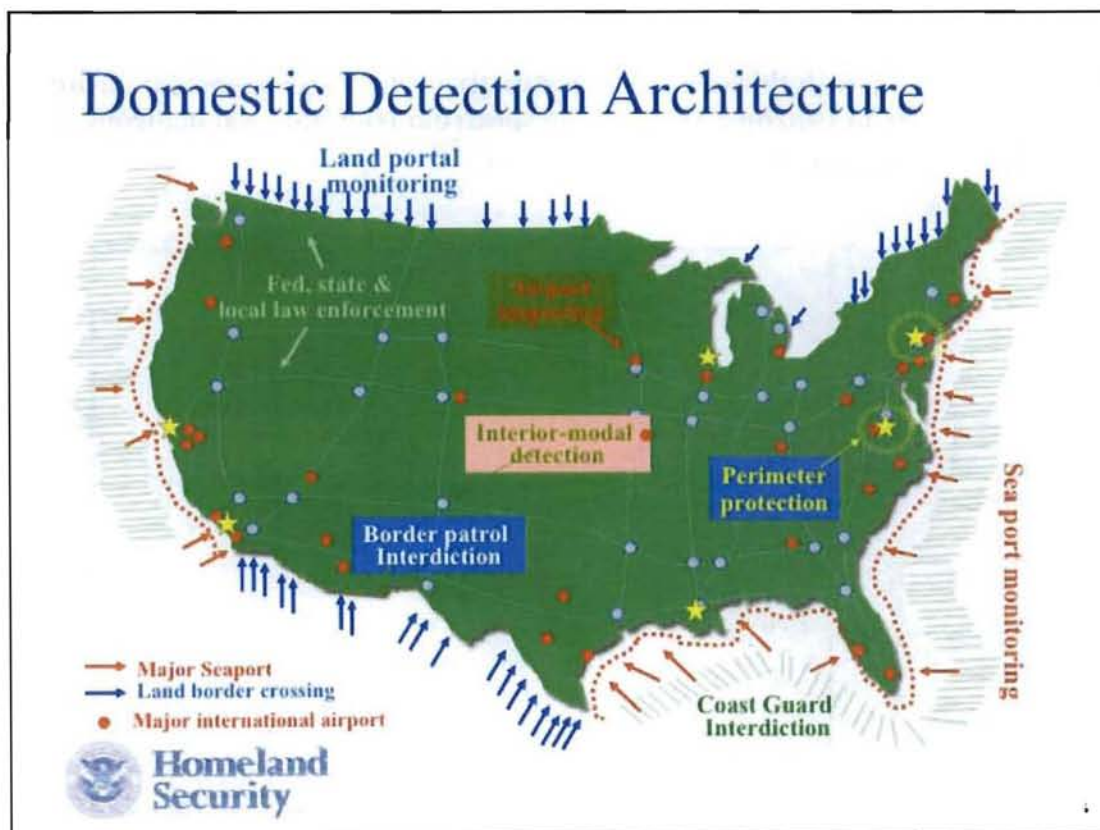
Figure 12: The Department of Homeland Security (DHS) employs multiple levels of detection and interdiction to thwart terrorist attacks in the United States [28]

reaches the primary target and before it can be released on a secondary target. The difficulty in the detection stage is that while nuclear materials emit unique and known radiation signatures, these signals are fairly weak and easily shielded from radiation detectors. An additional problem is the enormous scale of the task. Any comprehensive solution must therefore offer maximum efficiency at minimal cost and must also provide sufficient flexibility and scalability for deployment in a wide variety of portal monitoring scenarios.

1.4.1 Active interrogation

Existing passive-interrogation methods are assumed to be largely ineffective at interdicting smuggled fissionable materials, particularly on national and worldwide scales [29]. Ironically, the difficulty in this task arises in part from the success of the existing safeguards that make it extremely difficult for terrorist organizations to obtain dangerous quantity of SNM. Terrorists having possession of a large amount of nuclear material would certainly go to extreme lengths to protect it [30]. The solution to the weak radiation signature emitted by SNM is to use an active probe—an energetic beam of particles. Active techniques include x-ray imaging and signal enhancement through induced nuclear fissions in the target. The latter technique can employ neutrons, bremsstrahlung photons from high-energy electrons, or protons to produce signatures unique to SNM in the form of beta-delayed fission neutrons [31, 32, 33]. These signatures can also be used to identify the species of the nuclear material [34], which can aid in determining the threat level.

Figure 13: Mammoth cargo container ships, or "boxships" carry millions of containers across the world's oceans annually.

One of the greatest conceived threats is the smuggling of a nuclear device via ocean-going vessel [35]. Millions of containers per year enter the USA by cargo container ship, bound to destinations nationwide [36]. The largest existing cargo container ships are capable of carrying over 15,000 8'x8'x20' boxes. The danger is that these container ships provide a way for the terrorists to defeat land-based interdiction by detonating the device in or around the seaport of a major city. An additional potential threat is a nuclear device being delivered to a neighboring country and transported to the U.S. shore on a smaller vessel such as a private yacht. Researchers at LANL are currently investigating means of interrogating these vessels at a safe distance from shore. This technique is referred to as *standoff interrogation*.

Figure 14: Many private vessels have an extensive range and provide another potential means of delivering a nuclear device to the United States.

1.4.2 Standoff interrogation

Standoff interrogation involves long-range active scanning with a source-to-target distance ranging from 100 m to perhaps 1 km or more[13]. Ideally, the beam spot would be small enough for surgical scans--perhaps several feet in diameter at the target distance. Furthermore, the beam needs to be capable of penetrating several feet of dense material in order for scanning of boxships to be practical. The most viable candidate that meets all of these criteria is a beam of protons in the kinetic energy range 800 MeV $< T < 4$ GeV[14]. A high-energy proton beam is readily produced with sufficient current and a small enough beam profile to perform the scan at such distances. It is extremely difficult to meet all of the above criteria with

---

[13] The original goal was 5 kilometers; this is now considered to be impractical [37].

[14] Another potential method exists, quasi-passive interrogation using muonic x-rays [38]. The applicability of this technique to standoff interrogation is presently being studied at LANL.

UNCLASSIFIED – ADC Review by Alexander Saunders, P-25, on 3/23/2009

bremsstrahlung and neutron beams; the range of low- to medium-energy photons is limited by absorption in air and a neutron beam would require an impractical amount of high-energy flux. A high-energy photon beam could potentially satisfy all of the requirements to accomplish the scan, but it would not be less expensive to produce than a proton beam and it would be more difficult to meet radiological requirements because photons are much more penetrating than protons.

The dose delivered by the proton beam potentially poses a significant radiological risk to crewmembers on the ship and/or illegal immigrants who may be stowed aboard the ship. This imposes a limit on the amount of beam current that can be used, and hence the available signal. Thus, maximization of neutron detection capability is crucial to this technique. Helium-3 is the most attractive medium from a detection standpoint due to its superior efficiency compared to B-10 and lesser sensitivity to photon and charged-particle backgrounds compared to plastic scintillators. Unfortunately, He-3 is fairly expensive because it is quite rare on Earth. Additionally, competing demands for He-3 such as proposed power generation via nuclear fusion threaten to make it difficult to obtain large quantities in the years to come. Combining these factors it becomes immediately apparent that there is a substantial cost factor associated with deploying He-3 detectors on any kind of national scale.

1.4.3 Fusion power and the worldwide He-3 shortage

The He-3 fusion reaction has been under extensive study for over 20 years and is now widely regarded to be one of the best long-term solutions to the world's

energy crisis. Reactor engineering and development aside, the overwhelming

problem is that we simply do not have enough helium-3. Early studies estimated that

tens of metric tons of He-3 would be required per year to supply the USA's electricity

demands. However, current worldwide He-3 production, being almost entirely

limited to radioactive decay of tritium collected from spent nuclear fuel, is only in the

tens of *kilograms* per year [39, 40, 41] —1000 times less than what is required to

provide a viable fuel. Moreover, the quantity of He-3 required to build a research

reactor would essentially exhaust the entire present worldwide stockpile [40]. The

solution to this problem is beyond the scope of this work; however, its implication to

the Homeland Security effort is clear: He-3 use must be minimized by identifying and

implementing the most efficient use of He-3 *on the basis of the quantity used.*
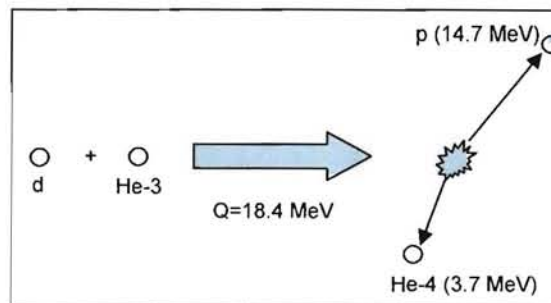
Figure 15: The d-He3 fusion reaction
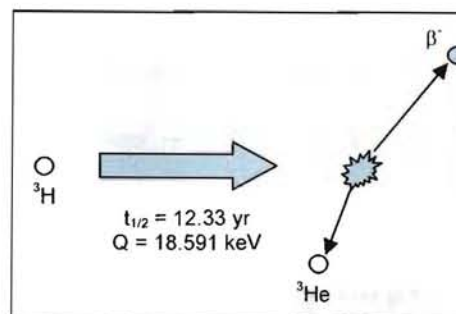
**Figure 16: Virtually all helium-3 in present worldwide stores has been produced
as a product of tritium β-decay.**

Chapter 2 : Theory of environmental effects:

The Efficacy[15]

In an experimental apparatus, interactions of source particles with any constituent of the apparatus other than the active face of the detector are called environmental interactions. Environmental interactions frequently cause an appreciable change in experimental count rates. This is called an open-laboratory scenario. Environmental interactions are particularly troublesome for fast-neutron $(0.1\,MeV \le E_n \le 10\,MeV)$ counting experiments such as those described in this thesis. Opposing scenarios, in which environmental interactions either are not present or they do not change the experimental count rate, are called closed laboratories. Open laboratories are problematic for experimenters because it is very difficult to accurately quantify the change in expected count rate due to the environmental interactions. This chapter defines a new semi-deterministic method for estimating environmental effects, the efficacy method.

A radiation source, a target, and a detection system are the main components of an experimental apparatus which directly impact its efficacy. An experiment which utilizes well-known and controlled source and target is referred to as a closed-source experiment. A closed-response experiment describes an apparatus with a well understood and controlled detection system. A closed-response system is able to isolate the experiment from environmental factors through collimation and shielding,

---

[15] The term efficacy is adopted from the field of health care, where it describes the capacity of a treatment to produce a certain effect [26]. In this context it describes the likelihood of an environmental interaction to produce fewer or additional counts in a detector.

while a closed-source system eliminates effects from within the source and/or target such as multiple scattering and self-attenuation through proper choice of materials, target sizes, etc.

Characterizing an experiment as having either a closed source or closed response infers, using the above definition, that the unspecified component is open and as a result, the experiment is in an open-laboratory environment. Conversely, the terms open source and open response do not infer information about the other constituent. Only apparatuses in which both the radiation source and the radiation detectors are directly controlled are considered closed laboratory environments. When pondering environmental effects, then, it is logically improper for the experimenter to ask the question "is the source or response *closed*?" Instead, the questions to be asked are "is the source or response *open*?" This terminology convention encourages the experimenter's thought processes to identify environmental effects, while still allowing an entire experimental apparatus to be described with a single term.

Fast-neutron counting experiments are inherently problematic because neutrons having energies in the regime $(0.1\,MeV \le E_n \le 10\,MeV)$ have a very long interaction length in air while having a scattering cross-section greater than 1 barn for many materials commonplace in the laboratory. A fast neutron may either elastically scatter from a nucleus or it may inelastically scatter, inducing a nuclear reaction. Equations. (1.1) and (1.2) show that an elastically scattered neutron will lose more energy when scattering from a light nucleus as opposed to a heavy, large Z, target. In

doing so, the neutron becomes even more likely to scatter again, as scattering cross-sections typically increase for decreasing energy in this energy range. This is particularly true for hydrogen (see Figure 1). It is the combination of these two properties that make materials rich in hydrogen content, such as water and plastic, the preferred materials for moderating neutrons, or reducing their kinetic energy. Unfortunately, many materials commonplace in the laboratory such as concrete, wood, asphalt, water, and plastic contain significant amounts of low-Z materials—most notably of course, hydrogen. Therefore, fast-neutron counting experiments can seldom ignore neutron-scattering effects and are almost always conducted in an open-response laboratory. This is particularly true for many active interrogation applications, where the scientist may have little control over the source and its environment[16]. Hence, it is proposed to modify Eq. 1.3 by introducing a new term describing a particular detector's efficiency in a particular environment, the *efficacy*:

$$\overline{\varepsilon_e} \equiv \overline{\varepsilon_I} \cdot (\kappa + 1)$$
$$\kappa(efficacy) + 1 \equiv \kappa_\Phi \cdot \kappa_\gamma \tag{2.1}$$

where $\overline{\varepsilon_I}$ is the average intrinsic efficiency, $\overline{\varepsilon_e}$ is defined to be the experimental efficiency, and the two coefficients κ_Φ and κ_γ represent the sum of environmental effects combined into two factors; κ_Φ, the *flux efficacy*, represents the change in magnitude of the incident particle flux and κ_γ, the *counting efficacy*, represents the change in efficiency due to perturbations of the neutron energy spectrum and

---

[16] The experimenter may actually have a strong motivation to avoid interfering with the source--in fact desiring to stay as far from it as possible. One example situation where this applies is inspection of a container that is suspected of containing a weapon that could potentially be activated remotely!

---

geometric distribution of the incident flux. Comparison of (2.1) with Eqs. (1.6), (1.7), and (1.9) reveals that the experimental efficiency is equal to the flux-weighted average total efficiency divided by an *effective* fractional solid angle subtended by the detector Ω_{eff}, or:

$$\overline{\varepsilon_e} = \overline{\varepsilon_T} \cdot \left[\frac{\Omega_{eff}}{4\pi} \right]^{-1} \tag{2.2}$$

The efficacy, then, is the *fractional increase in the number of counts in the detector, per source particle travelling directly from the source to the detector's active surface, due to environmental interactions*. In conceptual terms, the efficacy can be said to provide the connection between the closed laboratory and open laboratory. Efficacy additionally can be used to relate different open-laboratory scenarios to one another.

2.1 Understanding the two components of Efficacy

The two components κ_Φ and κ_γ in Eq. (2.1) are inextricably related to one another, as virtually all nuclear processes are strongly energy-dependent and involve the transfer of both energy and momentum. However, it is useful to consider them as conceptually distinct quantities. As a further note, keep in mind that nearly all detectors used in nuclear science are somewhat sensitive to particles entering the detector at positions not considered part of the active area. This is particularly true for moderating neutrons detectors that count fast neutrons by relying on external moderation to thermalize the neutrons. Therefore, it is important to remember that the detector area involved in the efficacy comprises the *entirety of the detector's*

outer surfaces. The surface area used for normalization, however, remains the

detector's front face.

2.1.1 The flux efficacy (κ_Φ)

To reiterate, κ_Φ is the overall change in magnitude of the particle flux entering the detector due to environmental interactions. As shown in Figure 17 below, changes in particle flux arise from many objects and processes. The challenge faced by the experimentalist is analyzing the environment and accurately determining which objects will have the greatest effect on the particle flux. A solid apriori assessment will serve as a guide for decisions such as detector placement, location and makeup of supporting apparatus, source configuration, etc. The primary considerations are the object's solid angles relative to the source and detector and total cross-section for neutron interactions. Obviously, hydrogenous materials such as wood, oil, water, concrete, etc. near the source or detector are particularly troublesome and should generally be avoided when possible. Depending on the specific application, it is not always necessary to measure κ_Φ. However, the experimenter should consider it a general requirement to at least achieve a reasonable estimate of its magnitude and take whatever steps are possible to restrict it as close to unity as possible.
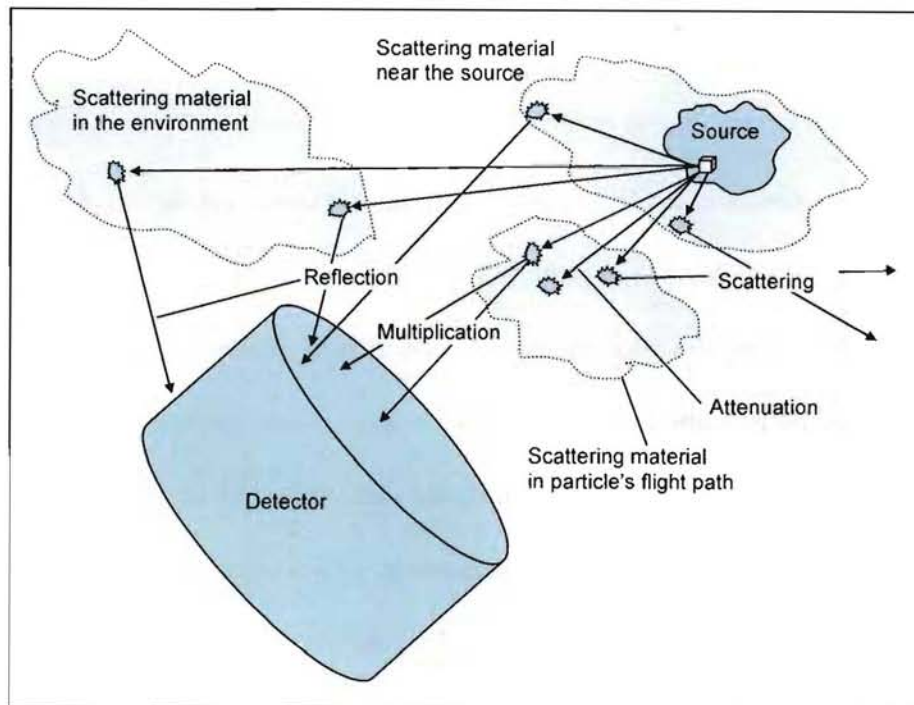
Figure 17: Examples of the various scattering processes that effect the absolute particle flux incident upon the detector.

2.1.2 The counting efficacy (κ_γ)

For the purposes of analyzing the effect that the change in particle flux has on experimental intrinsic efficiency, it is convenient to simplify our thought processes by considering the effect that nuclear interactions have on the average energy of a large number of incident particles. Some of the more dominant nuclear interactions and their effects on both efficacy parameters are summarized below[17].

---

[17] In the inequalities describing κ_Φ and κ_γ, the use of multiple symbols suggests the relative degree of the effect. For example, $\kappa_\Phi \ll 1$ might suggest that κ_Φ may be in the range $0.8 < \kappa_\Phi < 1$, whereas $\kappa_\Phi \lll 1$ may suggest $0.1 < \kappa_\Phi < 1$. In all cases these are merely generalizations, however, and by no means does this notation suggest universally applicable values.

- **Attenuation:** Most materials preferentially absorb thermal neutrons.

Therefore, as attenuation becomes a significant effect, the neutron energy spectrum

generally increases in average energy, or is hardened. This increase in the average

energy would cause an additional decrease in efficiency; thus $\kappa_\Phi < 1$ and $\kappa_\gamma < 1$.
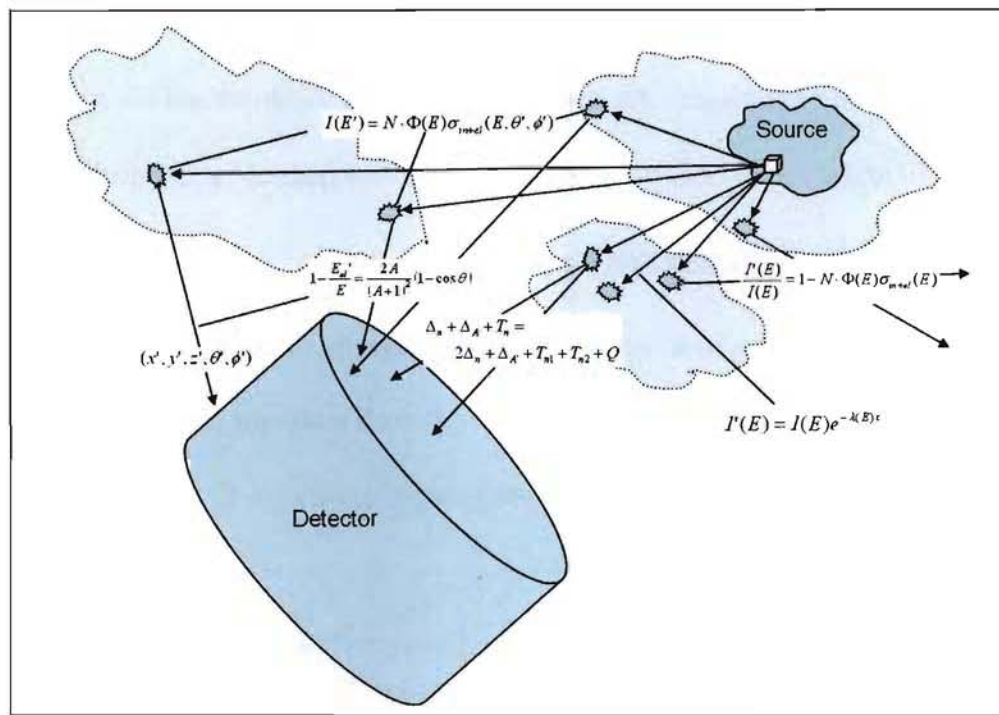
Figure 18: Effects of various scattering processes on energy spectrum and particle incidence.

- **In-flight scattering:** Neutron scattering cross-sections globally decrease with

energy for most elements, although not as universally as for attenuation. This is the

case for long flight paths through atmosphere such as in standoff interrogation

experiments. In this case, a significant number of neutrons can be removed by

scattering but the effect on the energy spectrum is much less significant:

$\kappa_\Phi \ll 1$ and $\kappa_\gamma \approx 1$.

- **Near-source scattering:** This is a much more complicated situation, and can be the most difficult to accurately assess. Hydrogenous materials have a large scattering cross-section and also extract significant amounts energy from the source particles. For one example, if the source is, say, hidden in an oil drum, the flux is significantly increased because the drum has a solid angle of 4π for source particles and the detector has roughly the same solid angle for the drum and the source: $\kappa_\Phi \ggg 1$ and $\kappa_\gamma \gg 1$. High-Z materials can have significant cross-sections but generally have a lesser effect on the particles energy: $\kappa_\Phi > 1$ and $\kappa_\gamma \approx 1$. Many middle-Z materials and a few high-Z materials have both large absorption cross-sections and large scattering cross-sections. If such materials are present, the flux and efficiency generally increases only slightly: $\kappa_\Phi > 1$ and $\kappa_\gamma > 1$.
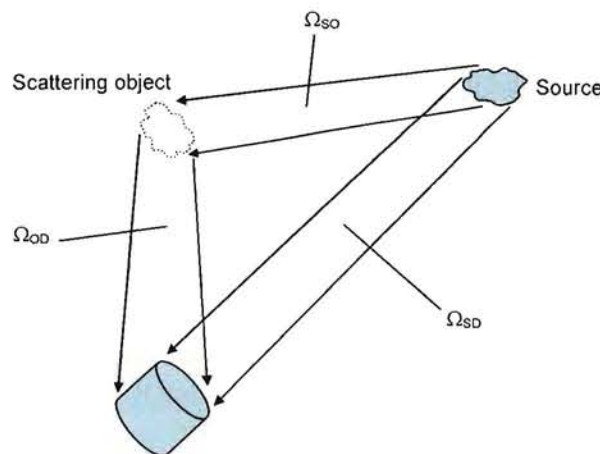
Figure 19: Determination of the flux efficacy factor for neutron-scattering objects in the environment.

- **Scattering from objects in the environment** is generally considered to be a

source-induced background effect. For environmental objects, κ_Φ can be calculated directly. Assuming isotropic source emission and semi-isotropic reflection[18] from the object:

$$I_T = I \frac{\Omega_{SD}}{4\pi} + I \frac{\Omega_{SO}}{4\pi} \alpha \frac{\Omega_{OD}}{2\pi}$$

$$\kappa_\Phi = I_T \bigg/ I \frac{\Omega_{SD}}{4\pi} \qquad\qquad (2.3)$$

$$\rightarrow \kappa_\Phi = 1 + \frac{\alpha \Omega_{SO} \Omega_{OD}}{2\pi \Omega_{SD}}$$

where I is the source current, I_T is the incident current, Ω_{SD} is the source-detector solid angle, Ω_{SO} is the source-object solid angle, Ω_{OD} is the object-detector solid angle, and α is the albedo of the object. Of particular concern are extensive planar surfaces such as concrete floors and walls or the surface of the ocean for maritime applications. Figure 20 shows that the albedo for concrete is 0.5-0.8 in the neutron energy regime applicable to this work. The result of such high albedo is that most of the neutrons emitted from the source have multiple opportunities to interact with the detector.

---

[18] The total solid angle of emission for particles reflecting from a surface is 1/2, or 2π steradians.
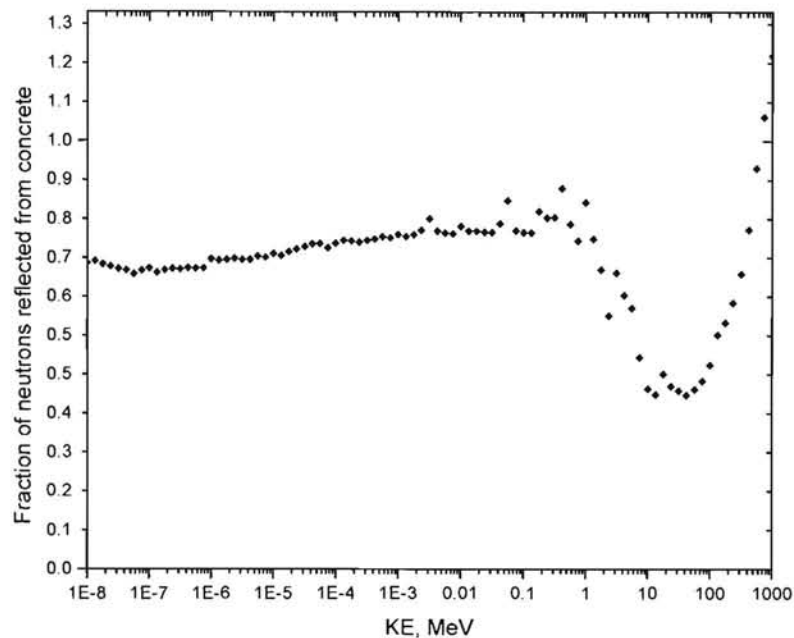
Figure 20: Neutron albedo from a thick concrete slab. The bumpiness is caused by scattering resonances in the constituents of the concrete. Notice the multiplication effect $(d\alpha/dE > 0)$ for $E_n > 40$ MeV as the cross-section for reactions producing multiple neutrons becomes significant. At even higher energies, interactions involving cascades of (n, xpxn) and (p, xpxn) reactions and (n, spallation) become possible and α eventually exceeds unity.

2.1.3 Examples of efficacy calculations and discussion

Consider, for example, a He-3 detector having a surface area 200-cm^2 located 1-m from an isotropic neutron source with the entire apparatus located 1m above a semi-infinite concrete floor and the source-detector axis parallel with the surface of the floor. Take $\alpha = 0.8$, $\Omega_{SD} = 200/100^2 = 0.02$, and $\Omega_{SO} = 2\pi$ in (2.3). Using MCNPX, Ω_{OD} was calculated to be 6.83 x 10^{-3}. This results in a flux-efficacy factor of $\kappa_\Phi = 1.273 \pm 0.02$. Now move the detector to a distance of 5 meters from the source. Ω_{OD} decreases by about a factor of 10, to 7.04 x 10^{-4} because the detector is further away from the part of the floor most strongly illuminated by the source.

However, Ω_{SD} simultaneously decreases by a factor of 25, so the net result is a

considerable increase in flux efficacy: $\kappa_\Phi = 1.704 \pm 0.03$.
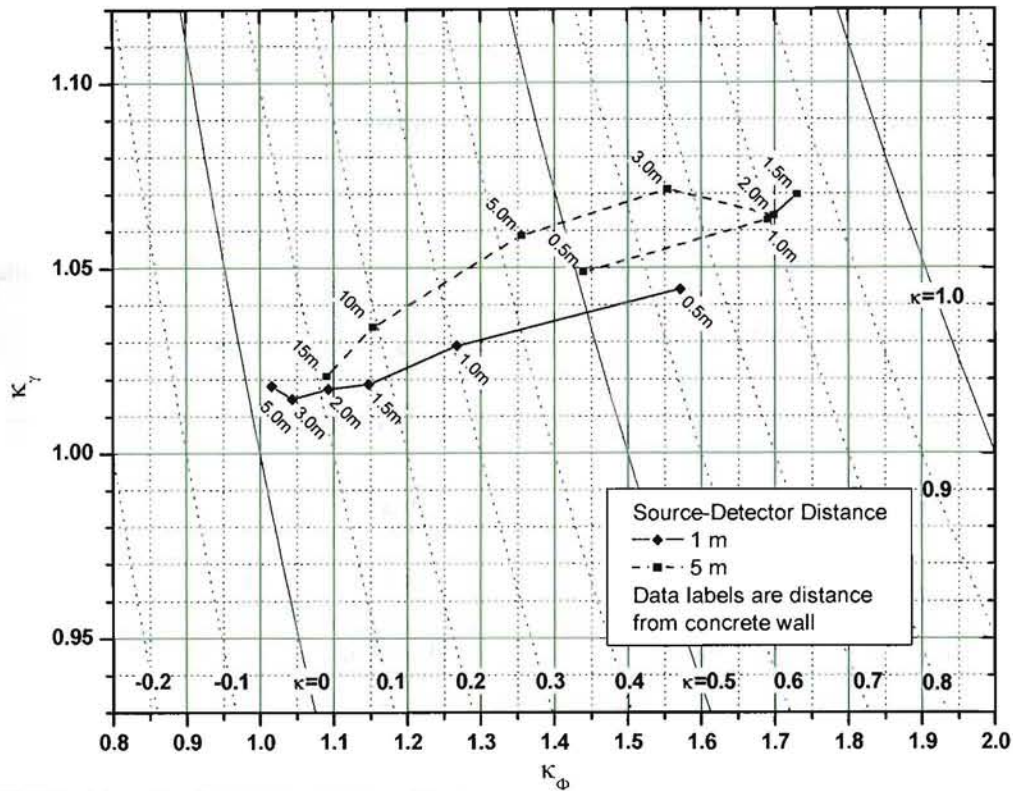
Figure 21: Efficacy of a nearby concrete wall for an epithermal neutron spectrum simulated by MCNPX. The statistical error bars were omitted for clarity; they are less than 1%[19,20].

A suggested rule of thumb in the laboratory is to keep the efficacy (κ) below

10%. One would naturally expect the efficacy to decrease as the experimental

apparatus is moved further from the wall. Figure 21 shows several MCNPX

---

[19] The actual detector model used was a 5-cm sphere of He-3 at 300-mbar surrounded by an 8-cm sphere of moderating HDPE. The neutron energy spectrum was uniform in probability from 100 keV-1 MeV. This paradigm is fairly representative of delayed neutron spectra being investigated at LANL by He-3 research detectors in terms of total efficiency and efficiency as a function of neutron energy.

[20] There are no universally-accepted neutron energy limits for the epithermal regime; for the purposes of this document the energy range will be defined as: $0.1eV \le E_{epi} \le 0.1MeV$.

---

calculations for the two experiments described in the preceding paragraph. Both 1-m and 5-m source-detector distances are presented for a wide range of wall distances. For a source-detector distance of 1-m, a 3-m distance from the wall is sufficient to meet the $\kappa < 10\%$ paradigm. For a 5-m distance, the experiment must be moved >15m from the wall. In summary, for a single nearby semi-infinite wall, the necessary distance to minimize the efficacy effect is roughly 3 times the source-detector distance when the source and detector are less than a few meters apart, and it is somewhat greater than that for larger separations. The efficacy is almost entirely due to the increase in flux; the energy effect $\left(\kappa_\gamma \right)$ increases as the source-detector distance increases, but remains below ~110% in this scenario.

Interestingly, the 5-m source-detector distance data actually shows a *decrease* in efficacy for a wall distance less than 1.5m. This effect arises due to multiple scattering in the wall. As the source-detector apparatus gets closer to the wall, the average depth of the scattering point inside the wall becomes greater and the neutrons experience an increased probability of scattering away from the detector. The effect was also observed for the source-detector spacing of 1-m. The applicable wall distance was < 0.25-m in this case, and the data was omitted in the interest of readability.

Now consider the same two experiments placed inside a concrete room 10-m on a side. The neutrons are now confined on all sides and they can scatter from the walls multiple times. Using the facts that $\Omega_{SO} = 4\pi$ for particles emitted from the source and $\Omega_{S'O'} = 2\pi$ for wall-to-wall interactions and assuming equidistant walls

---

and negligible fraction of neutrons absorbed in the detector on each "bounce", Eq.

(2.3) can be modified thusly:

$$I_{Box} = I\frac{\Omega_{SD}}{4\pi} + \sum_n I\alpha^n \frac{\Omega_{OD}}{2\pi}$$

$$\rightarrow K_{\Phi Box} = K_{\Phi Wall} + \sum_{n>1} \frac{\alpha^n}{\Omega_{SD}}\Omega_{OD} = 1 + \frac{\alpha}{1-\alpha}\frac{\Omega_{OD}}{\Omega_{SD}}$$

(2.4)

Equation (2.4) grows without bound as $\alpha \rightarrow 1$. This is a direct result of

neglecting the absorption of neutrons in the detector. Several alternative expressions

for the efficacy of a box can readily be developed that do not make this assumption.

Depending on other assumptions that are made, these expressions rapidly grow in

complexity and become cumbersome to calculate on-the-fly. Thus, they are

considered inconsistent with the spirit of the efficacy concept and are not presented

here.

Comparison of the second terms of Eq. (2.3) and Eq. (2.4) shows that the

impact of the box on the incident flux is much more significant than for a single

wall—the efficacy is 4 times greater for $\alpha = 0.75$! The energy effect is also

increased, as the neutrons lose more and more energy as they continue to rattle

around the room. Figure 22 summarizes the effects for various locations within a 7-

m-tall box:
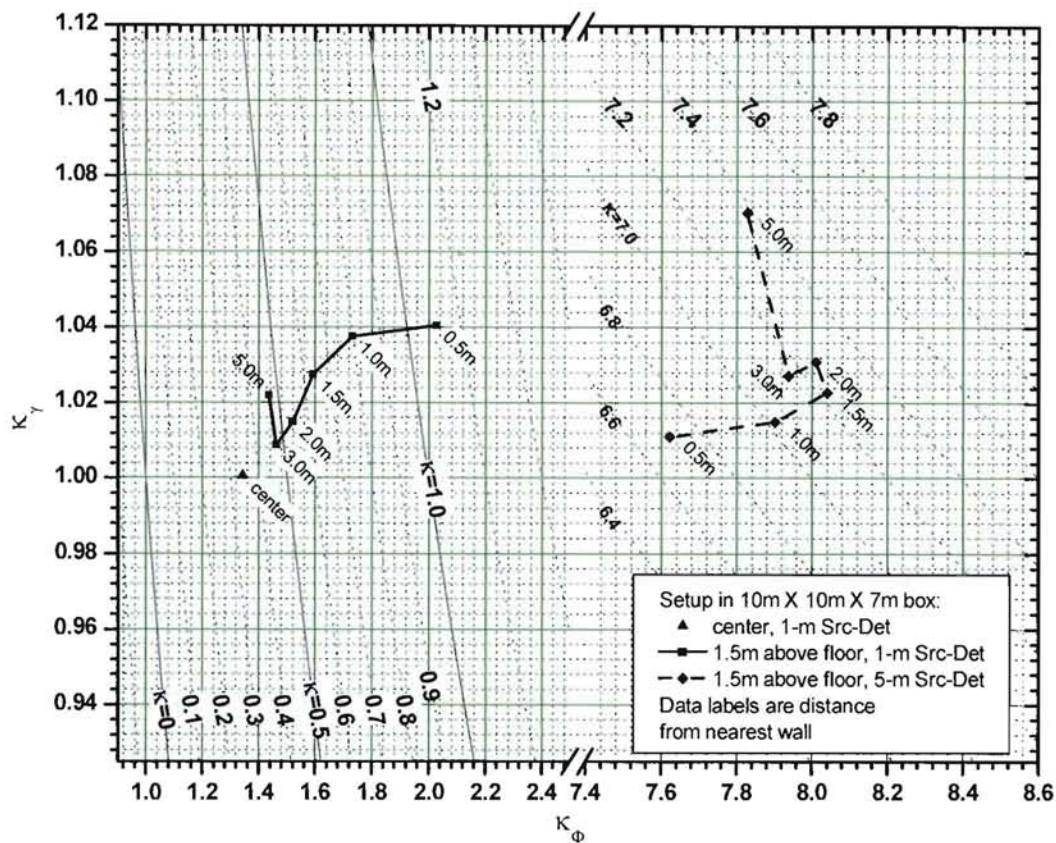
Figure 22: Efficacy of a 10-m square by 7-m tall concrete box for an epithermal neutron spectrum simulated by MCNPX. The statistical error bars were all less than 1% and were omitted for clarity.

The data from Figure 21 and Figure 22 are given in Table 2 for easier comparison. The efficacy at the center of the box is 10 times greater than the single-wall case at a distance of 5 meters from the wall. For a detector 1-m from the source positioned 1.5m above the floor, the efficacy is increased by at least a factor of 2.5; this minimum increase logically occurs when the apparatus is in the center of the room. The magnification effect of the box increases to more than 6.5 times when the apparatus is very close to an adjacent wall. The effect is even more dramatic when the source-detector distance is increased to 5 meters—the efficacy is roughly a factor

of 10 greater than the single wall no matter where you are in the room. The count rate in this situation is over *eight times greater* than if there were no walls present.

5-m from wall 1-m Src-Det	Center of box 1-m Src-Det	Distance to nearest wall in box, m	In Box 1.5-m above floor 1-m Src-Det	1.5-m from wall 1-m Src-Det	Distance to nearest wall in box, m	In Box 1.5-m above floor 5-m Src-Det	1.5m from wall 5-m Src-Det
		0.5	1.111		0.5	6.708	
		1.0	0.797		1.0	7.022	
0.034	0.343	1.5	0.637	0.169	1.5	7.223	0.718
		2.0	0.544		2.0	7.260	
		3.0	0.476		3.0	7.155	
		5.0	0.467		5.0	7.381	

Table 2: Values of efficacy (κ) for concrete wall and concrete box.

2.2 The neutron gas concept

Eschewing mathematical rigor, the situation can be conceptualized in an alternate fashion by envisioning a neutron gas being emitted by the source. Albedo neutrons are analogous to pressure waves being re-emitted from nearby objects, walls, etc. that they come into contact with. These waves, being comprised of uncharged particles, do not interact with each other and can be modeled as a statistical ensemble similar to an ideal gas [27]. A given experimental configuration thus creates a particular neutron gas flux-pressure gradient $\Psi(\vec{r}, E)$ that the detector is subjected to in addition to the neutrons that travel directly from the source into the detector's acceptance. The flux-pressure gradient varies with position in both magnitude and energy spectrum. If the detector were rotated about the source, the direct flux would not change but the detector would be placed in a different flux-

pressure scenario. On the other hand, if the distance from the source to the detector were changed, the direct flux would change but the flux-pressure would remain unaffected. In both cases, however, the neutron gas itself remains constant.

2.3 Closing remarks on efficacy

It can be impractical to calculate wall-to-detector solid angles with any appreciable accuracy on the fly in a laboratory setting. On the practical side, it is easy to envision a small pocket reference book containing a compendium of efficacy values that can quickly be looked up for various experimental situations. Most importantly, a thorough understanding of the principles presented above can contribute invaluable insight into how much detail must be included in computer models to accurately reproduce the experiment.

As a final note, the above discussion has considered the source to be completely open and uncollimated. It is frequently fairly easy to eliminate much of the efficacy effect using a neutron-absorbing collimator. Materials typically used for this purpose include polyethylene doped with boron, or b-poly, and outer sheets of Cadmium wrapped around inner layers of moderator (usually HDPE or b-poly). It is never possible to completely ignore environmental effects in high-energy neutron-counting experiments no matter how well the source is collimated, however, as significant numbers of neutrons can interact with environmental objects after scattering from the front surface of the detector or after passing through the detector entirely. However, through careful attention to details during the planning and construction phases of the experiment, environmental factors can usually either be

reduced to negligible levels during the experiment or at least accounted for with

simple additions to the geometry model used in the simulation.

Chapter 3 : Benchmarking Studies

The array design work was almost entirely performed with the monte-carlo

radiation transport code MCNPX. The veracity of MCNPX's ability to simulate

neutron scattering processes and to accurately predict detector response is studied

below by a preliminary series of experiments. These experiments were conducted to

benchmark MCNPX.

3.1 The MCNPX code

MCNPX is an extension to the MCNP code produced and maintained at Los

Alamos National Laboratory. Development of MCNP and its parent codes dates back

to the first nuclear reactor design work in the 1950's. MCNPX extends the capability

of MCNP to simulate nearly all particles, including heavy ions, up to TeV energies[21]

by integrating several other codes such as LAHET, CEM, etc. The recent addition

inclusion of light ions from nuclear reactions into MCNPX gives the code the

capability of tracking the proton and triton daughter particles from the ^{3}He(n,p)^{3}H

reaction. This allows MCNPX to simulate interactions with the interior of the

apparatus, namely wall effects. This improves the code's accuracy in predicting

count rates, as it allows the user to specify a lower energy threshold that mimics the

---

[21] MCNPX does not define a maximum energy limit; however, care must be taken to ensure the applicability of the high-energy models used in the code. This should be considered on a particle-by-particle basis. A reasonable energy limit where this may start to become a consideration would be E > 10GeV.

lower-level discriminator (LLD) used to remove electronic noise and contributions

from other particles from empirical helium-3 spectra.
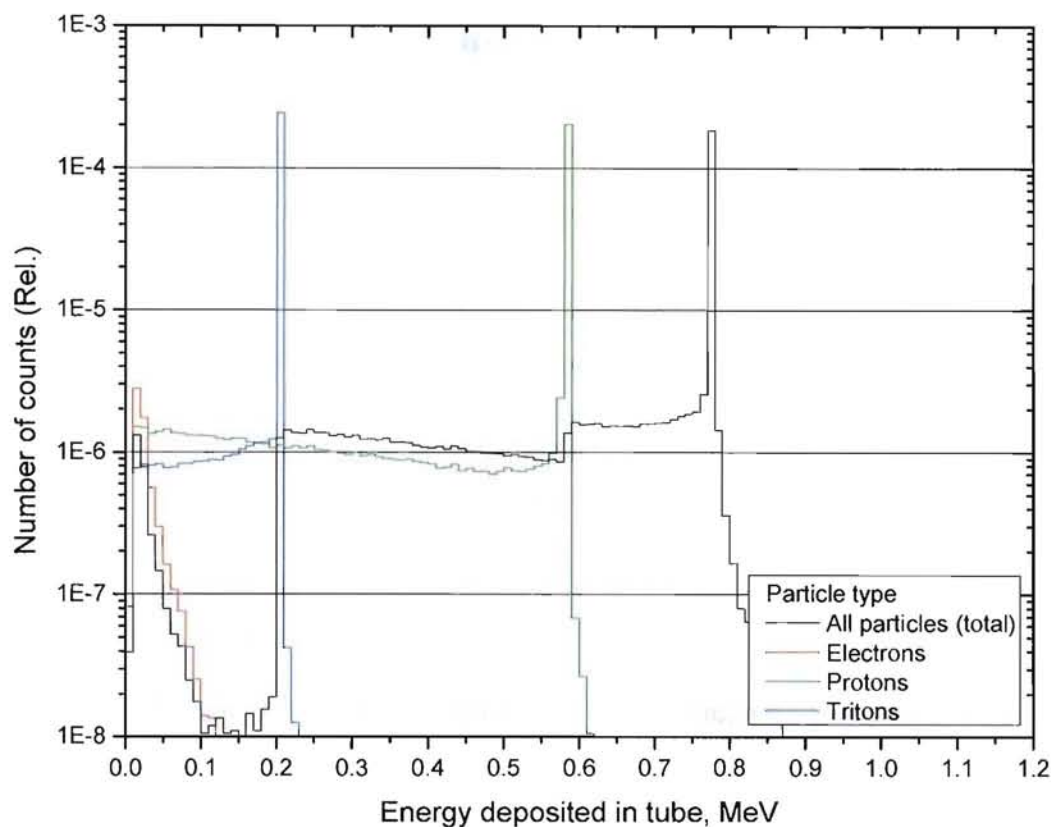
Figure 23: MCNPX pulse-height light tally of energy deposited in He-3 tube from 3He(n,p)3H reactions, broken down by particle type[22]. The steps in the sum spectrum correspond to wall effects (see § 1.2.1.2). Notice that the peak in the proton spectrum is slightly shorter than that for the tritons; this demonstrates that more protons stop in the wall because of their greater range. An energy threshold of 191 keV was used to identify pulses produced by neutron capture events.

[22] The F8 tally with PHL option is referred to as a pulse-height light tally because it was originally intended for scintillator applications using energy deposition-to-light output KERMA factors. It works equally well for directly tabulating energy from charged particles by setting the KERMA factors to unity. Energy deposited by photons is not directly scored; the F8 PHL tally relies on creation of secondary electrons to track photon contributions.

3.2 Experimental setup

Three experiments were conducted to benchmark various aspects of the ANDY detector design. The first was a pressure experiment, which measured efficiency versus partial pressure of He-3 inside the detector. An albedo experiment was performed next, which measured the efficiency of a He-3 counter versus the thickness of an HDPE layer behind the detector. Finally, a diffusion/reflection experiment was performed to measure the efficiency of a quasi-lattice detector as a function of the thickness of several intermediate HDPE layers. All three experiments used 2" diameter by 12" long drift tubes constructed and filled at LANL. The tubes were filled with a mixture of He-3 and proportional gas to 1 bar total pressure.

The experimental setups were designed to accentuate the desired effect and maximize repeatability. The setups generally consisted of HDPE sheets separated by cylindrical HDPE spacers to produce an air gap. The size of the HDPE sheets was 12" x 16" and the spacers were 1" diameter by 2-1/16" long. Holes 1/4" in diameter were drilled through the sheets and the center of the spacers and 1/4" HDPE rods were inserted through the entire setup to insure that all the layers were properly aligned. The detectors were placed in the air gap lengthwise with the detector axis aligned parallel to the long side of the HDPE sheets. The center of the detector was aligned with the geometric center of the sheets. The manufacturer of the HDPE sheets specifies a density ranging from 0.92-0.95 g/cm^3; the density used in this set of calculations was 0.93.

Throughout the experiments, the statistical error in the MCNPX runs was less

than 1%. The data were assigned a 5% systematic error to account for unquantifiable

approximations in the geometry definition.

Four different Cf-252 sources were used in the experiments. Sources no. 208,

209, and 210 were cross-calibrated using source 108 as the standard. The results are

shown in Table 3. The assumed uncertainty in the activity of source 108 is 10%.

This uncertainty was propagated to all sources. The source capsules were cylindrical,

0.8-cm diameter by 1-cm long. The actual active volume of the sources is not known;

a 1-mm dead layer in all dimensions was used in the model. The relationship

between the mass of the source and the neutron emission rate is described in

Appendix B.

Source Number	Reference Mass, µg	Reference Date	Experiment Date	n emission rate, s^{-1}
108	1.0 (±10%) (calibrated)	6/1/1987	8/9/2008	13560 ± 1356
208	0.110 (calc.)	12/31/1988	8/9/2008	1492 ± 149
209	0.214 (calc.)	12/31/1988	8/9/2008	2887 ± 289
210	0.211 (calc.)	12/31/1988	8/9/2008	2853 ± 285

Table 3: Cf-252 source data

3.3 Experimental results

3.3.1 Reduced chi-squared analysis

Throughout this document, a reduced chi-squared analysis was performed on

the experimental results whenever possible. The reduced chi-squared statistic, χ_v^2,

describes the goodness-of-fit of a set of empirical data points $\{y_i\}$ to a fitting function

$y(x_1, x_2, \ldots, x_n)$, and is given by:

$$\chi_v^2 \equiv \frac{\chi^2}{v} = \frac{\sum \frac{1}{\sigma_i^2}[y_i - y([x_1, x_2, \ldots, x_n]_i)]^2}{v} \qquad (3.1) \quad [43]$$

where σ_i^2 is the variance of each point and $v \equiv N - n - 1$ is the number of degrees of

freedom; with N being the number of data points and n being the number of

independent parameters in the fitting function. The fitting function is believed to be a

good approximation of the true dependence of the data if the reduced chi-squared is

approximately unity, $\chi_v^2 \approx 1$ [44].

Note that imposing an algebraic form on the fitting function $y(x_1, x_2, \ldots, x_n)$ is

not a requirement of reduced chi-squared analysis. There only must be some existing

means for sampling the function at a set of discrete points $\vec{x}_j \in \{[x_1, x_2, \ldots, x_n]_j\}$.

Ideally there would be a one-to-one correspondence between the sets of empirical

parameters $\{\vec{x}_i\}$ and sampled parameters $\{\vec{x}_j\}$, allowing immediate evaluation of Eq.

(3.1). If this is not the case, any $\vec{x}_i$ missing from $\{\vec{x}_j\}$ can be interpolated, assuming

that $y(\vec{x})$ is well-behaved and slowly varying in the region $\vec{x}_{j-m} < \vec{x}_i < \vec{x}_{j+n}$, where m and n specify a range of j appropriate to the chosen interpolation method.

The sampling scheme described above is a fundamental premise behind using computer models to model empirical parametric studies. In all the experimental results presented in this document the monte-carlo code MCNPX provides the conduit for nonanalytic sampling of the fitting function.

3.3.2 He-3 partial pressure experiment

Three detectors were tested containing He-3 at partial pressures of 50 mbar, 150 mbar, and 300 mbar. In the MCNPX models, tubes having >1 bar total pressure contained exactly 300 mbar of proportional gas. Helium-3 makes an effective proportional gas at pressures greater than 1 bar, but 300 mbar of standard proportional gas is retained in the high-pressure tubes to normalize the tube gain. The self-shielding effect of the He-3 gas becomes readily apparent in the model results above 300 mbar partial pressure as the slope of the curve becomes less than proportionality.
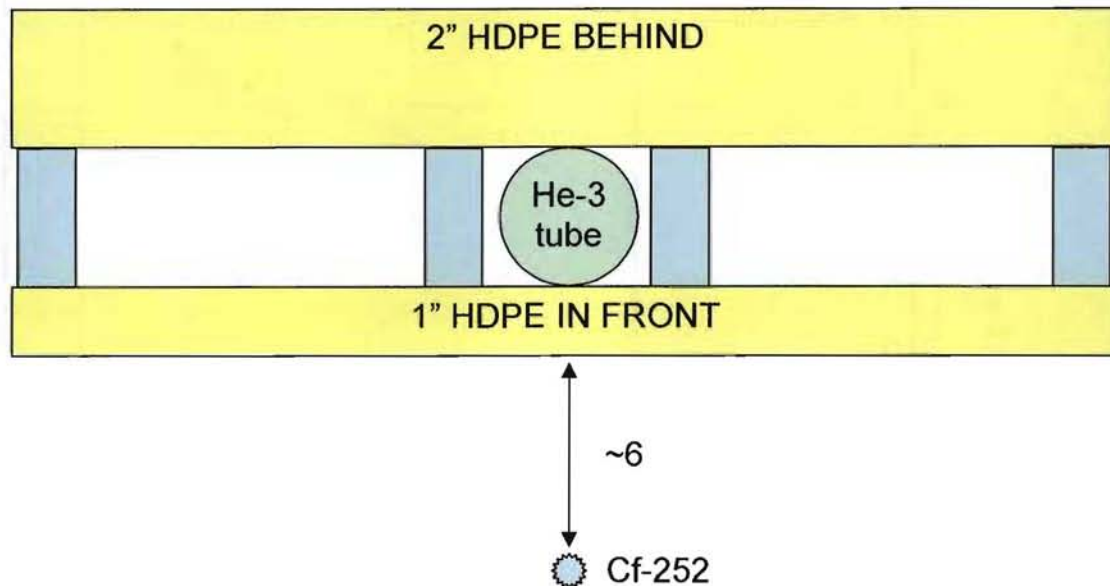
Figure 24: Setup for efficiency vs. He-3 partial pressure experiment

The data shown in Figure 25 data are within one standard deviation of the MCNPX prediction. A rigorous chi-squared analysis was not feasible, as there are only three data points. It would have been desirable to measure tubes containing higher He-3 pressure (>=1 bar) in order to quantify the self-shielding effect of the helium-3. This was forgone at the time due to limited quantities of helium-3 available at LANL and multiple other experiments competing for the gas. Further experiments may be performed at a future date to expand the dataset and verify the code's predictions in the high-pressure regime.
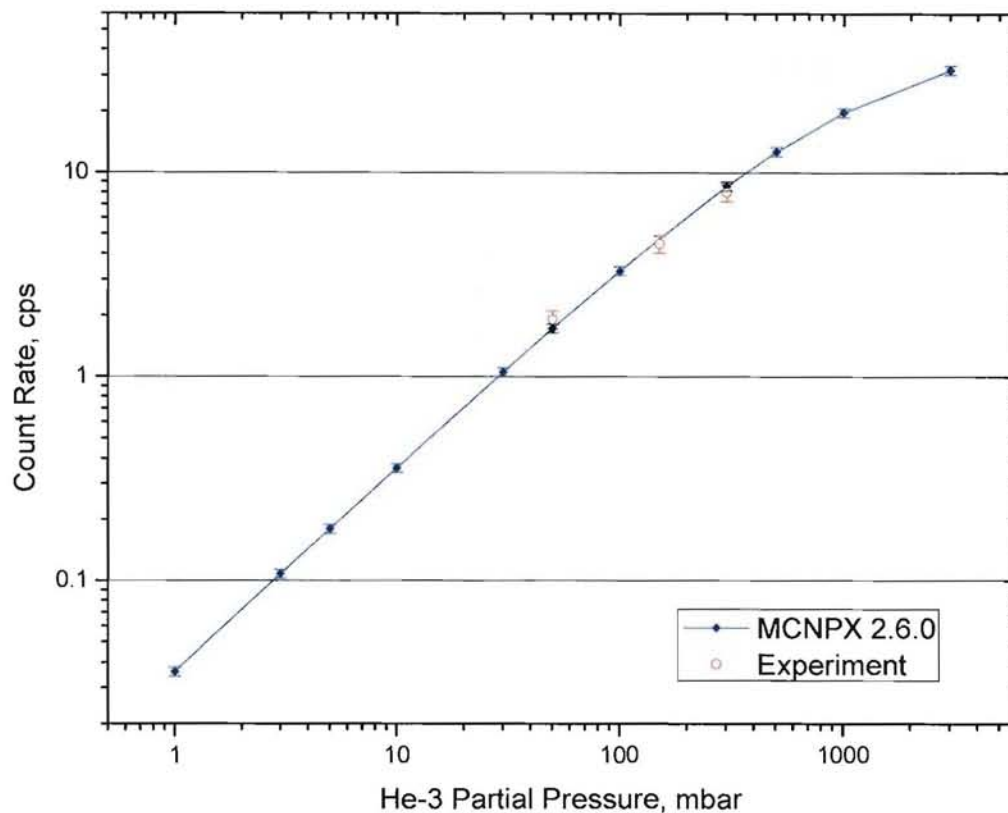
Figure 25: Results of the He-3 partial-pressure experiment

3.3.3 Albedo experiment

The purpose of the albedo experiment was to verify that MCNPX can correctly predict the increase in count rate from neutrons that backscatter from an adjacent HDPE slab. The front layer of HDPE was chosen to be 0.30 g/cm^2, or 1/8" in thickness. A front moderator must be used to provide structural stability and some initial moderation of the energetic Cf-252 fission neutrons. However, the front moderator was kept as thin as possible in order to avoid interference with the albedo signal. The results of the experiment appear in Figure 27.
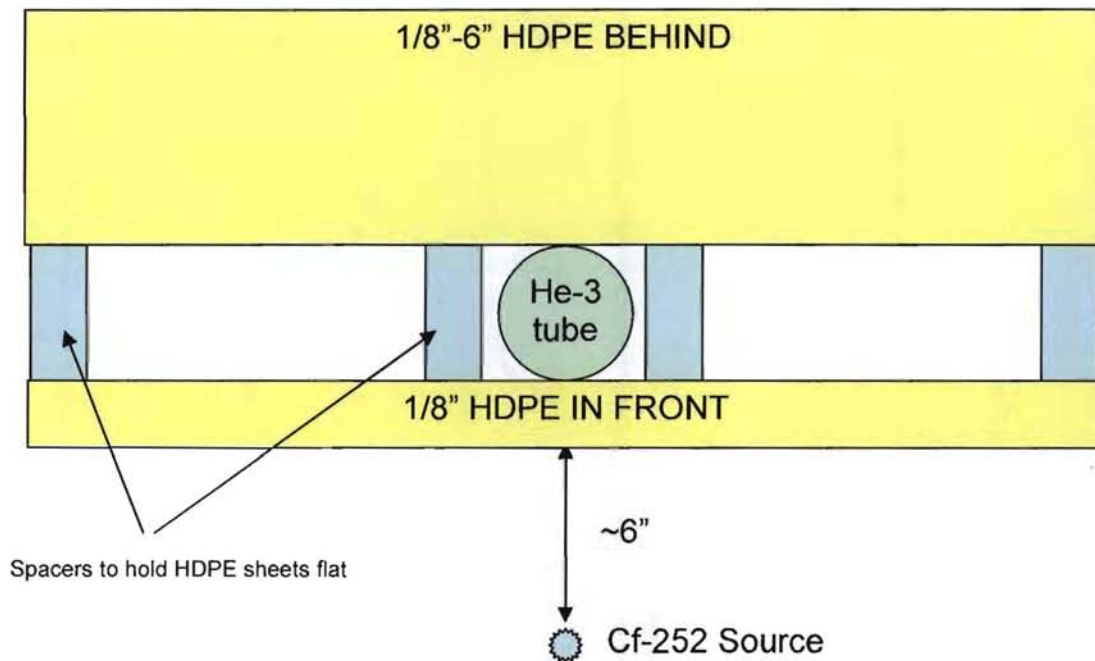
Figure 26: Setup for the albedo experiment

A low count rate at the two thinnest reflectors prevented a statistically significant measurement. The signal-to-noise was very poor, -15 dB for the thinnest reflector (1/8", or 0.30 g/cm^2), and -9 dB for the 1/16" reflector (0.60 g/cm^2). Consequently, these data points were excluded from the chi-squared analysis. The interior data points between 3/8" (0.90 g/cm^2) and 6" (14.48 g/cm^2) match within 1 standard deviation with two exceptions: there appears to be a slight deficiency (approx. 20%) in the MCNPX data at 2-3" thickness (4.83-7.23 g/cm^2). Although the points are consistent within two standard deviations, there may be inconsistencies in the density of the HDPE, as the slabs that were thicker than 1" were composed of multiple sheets that were cut from multiple sheets of stock.
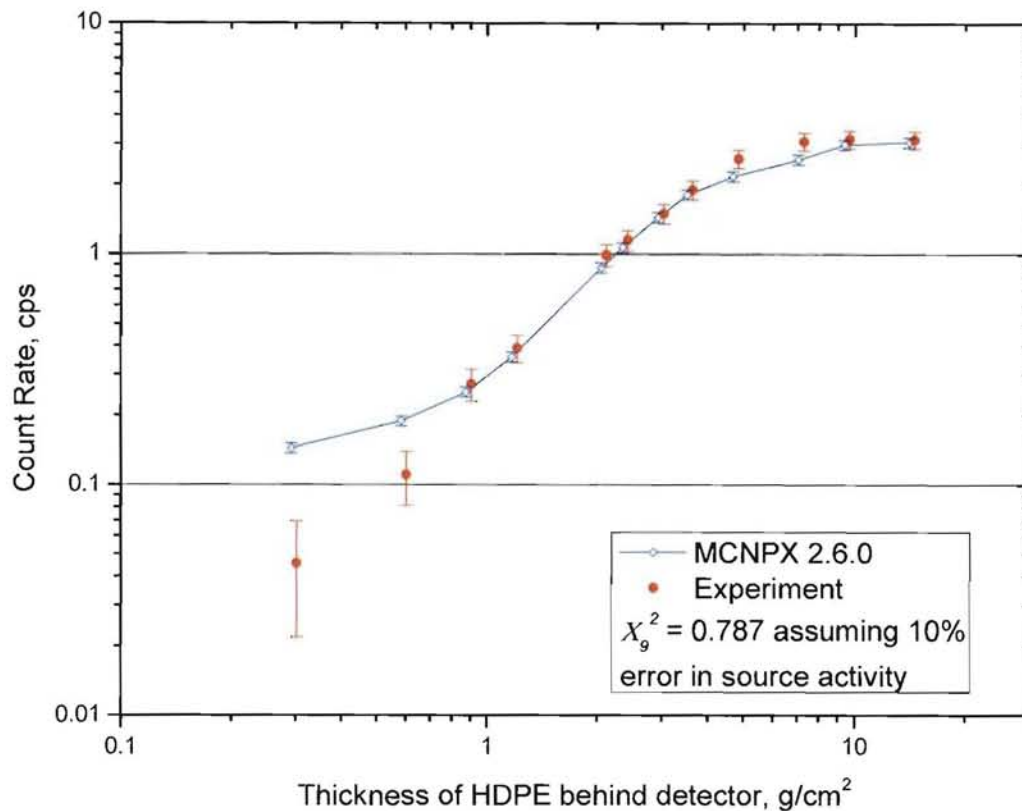
Figure 27: Results of Albedo experiment

The thickness of the HDPE slab is the one parameter used in calculating the reduced chi-squared statistic with 9 degrees of freedom of 0.787, which corresponds to a p-value of 0.63. It should be noted, however, that the experimental data are systematically greater than the MCNPX simulation. The measured count rate is on average 1.09 ± 0.02 times that predicted by MCNPX. This is within the uncertainty of the source activity and it can be treated as a systematic error. A similar result was found in section 6.1. The average excess in experimental counts between these two experiments is 1.076. After applying this empirical renormalization factor (see Figure 28), the source activity was assigned a much smaller systematic uncertainty of 3.9%. This represents the 1.9% error of the mean of the deviation combined with a

2% error to account for the uncertainty in the source position. The reduced chi-squared value after applying this correction is 1.38, corresponding to a p-value of 0.19. There is a 19% probability of obtaining empirical data as inconsistent with MCNPX as this result. This demonstrates that the MCNP(X) family of codes can be used to recalibrate sources with better precision than that specified by the manufacturer using simple experiments.
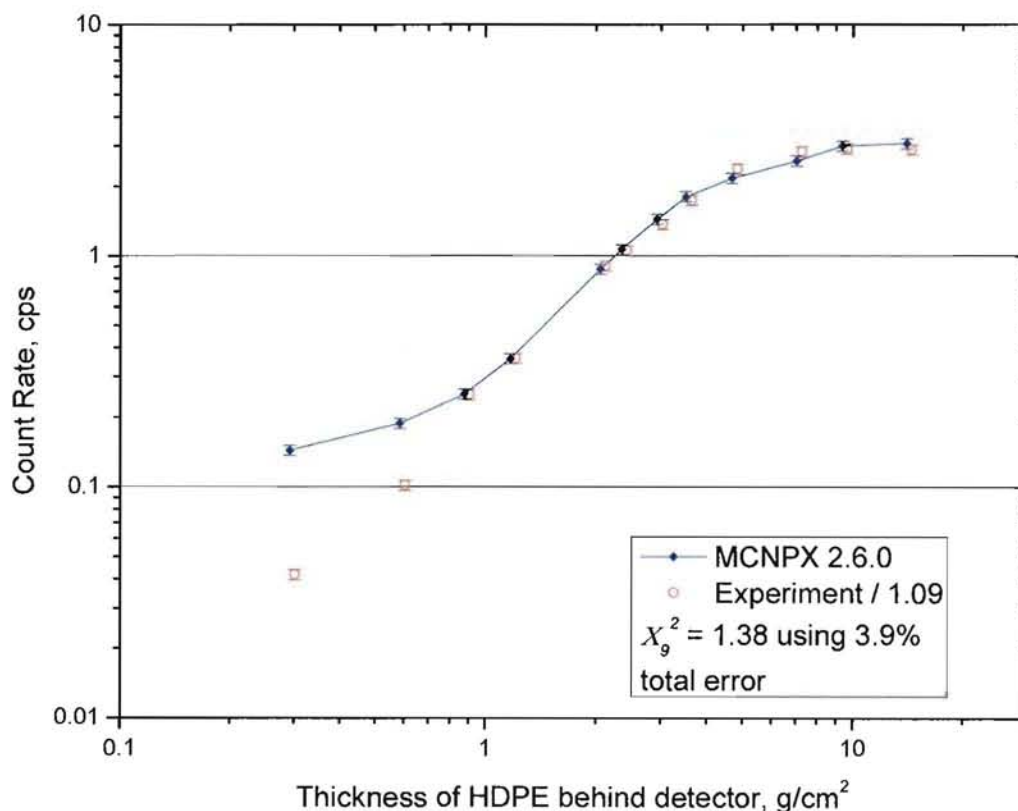
Figure 28: Renormalization of albedo experiment results. In this plot, the source activity was recalibrated using an empirical correction factor of 1.076.

3.3.4 Diffusion/reflection experiment

The diffusion experiment reproduced the effect of the neutron "trap" created

by the HDPE lattice. The simple design allows the separator layers to be quickly

switched out and facilitates the study of varying separator thickness without the

expense of manufacturing several lattices. This setup produced much lower count

rates than the other two experiments. To compensate for the low count rate, the

source was placed directly on the face of the front HDPE moderator. As a result, this

setup was much more sensitive to small errors in source placement than the other

experiments. The precision of the source position for simulation purposes was

assumed to be 5%.
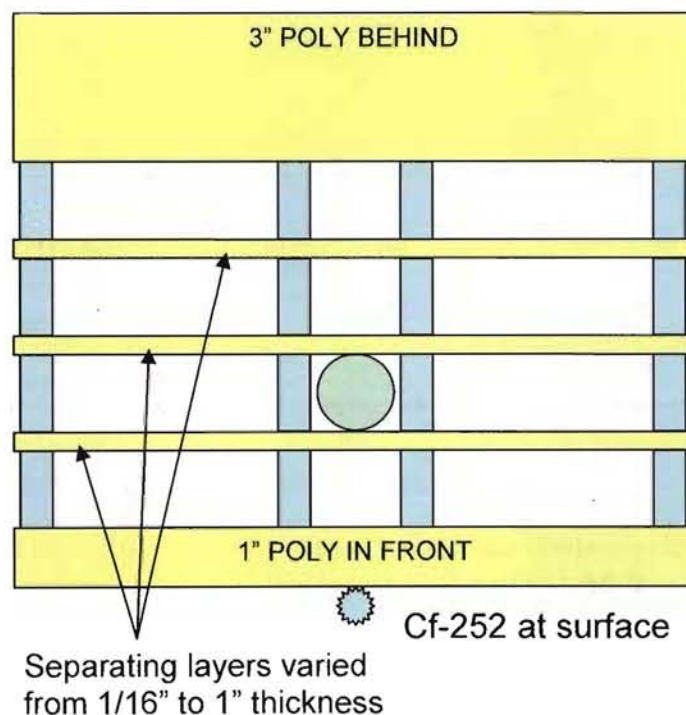
Figure 29: Setup for the diffusion/reflection (separator thickness) experiment
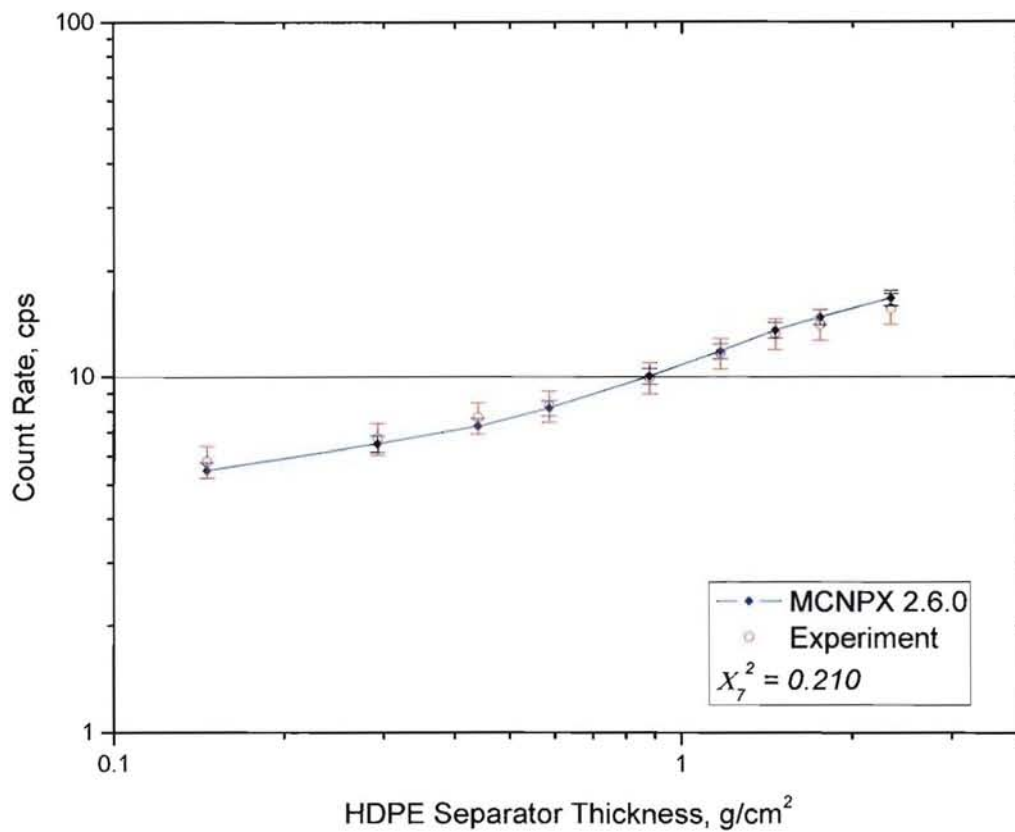
Figure 30: Results from separator thickness experiment

The empirical data and MCNPX results match very well. The small reduced chi-squared value of 0.21 suggests that the error bars are too large. In this case this is believed to be a mere coincidence. The empirical data and simulation just happened to almost exactly coincide because of the high sensitivity to the position of the source. It is expected that a more precisely-aligned setup would result in a systematic over-prediction of the source activity, similar to the albedo experiment of section 3.3.3 and the prototype tube-position experiment of Chapter 6. This situation could have been avoided had a stronger neutron source been available by moving the source farther away from the detector.

The slope of the MCNPX curve appears to systematically increase in a

slightly greater fashion than the experimentally measured values. The reduced chi-squared analysis shows that this difference in the second derivative is not statistically significant; however, the consistency of the trend suggests that a systematic error may be present. The most likely error is that the assumed value of 0.93 for the HDPE density is incorrect. Measuring the density of the HDPE was not immediately possible and was deemed unnecessary considering the scope of this experiment.

Ultimately, the results of this experiment are satisfactory considering the limitations of the apparatus. The discrepancies, while negligible, reinforce the paradigm that great care should be taken in experiments that involve high sensitivity. Additionally, material parameters should be verified with an independent measurement when feasible.

3.3.5 Conclusion of benchmarking studies

These results have shown that the Monte-Carlo code MCNPX provides predictions of helium-3 detector response within a few percent for many experimental setups involving polyethylene as the primary constituent. By extension, the code can be assumed to perform very well for pure Carbon as well. The code was shown to be quite sensitive to small modifications in the setup, suggesting that it will be quite sensitive to small environmental changes as well. Therefore, much care must be taken in modeling such experiments; not only to accurately define the pieces that make up the experimental apparatus, but also to adequately identify and characterize neutron-scattering objects in the environment.

Chapter 4 : Detector array optimization

The optimization work presented here is intended to lay a general groundwork

for application-specific designs of ANDY-type detectors. To achieve this, the

performance of a uniform[23] rectangular HDPE lattice was evaluated.
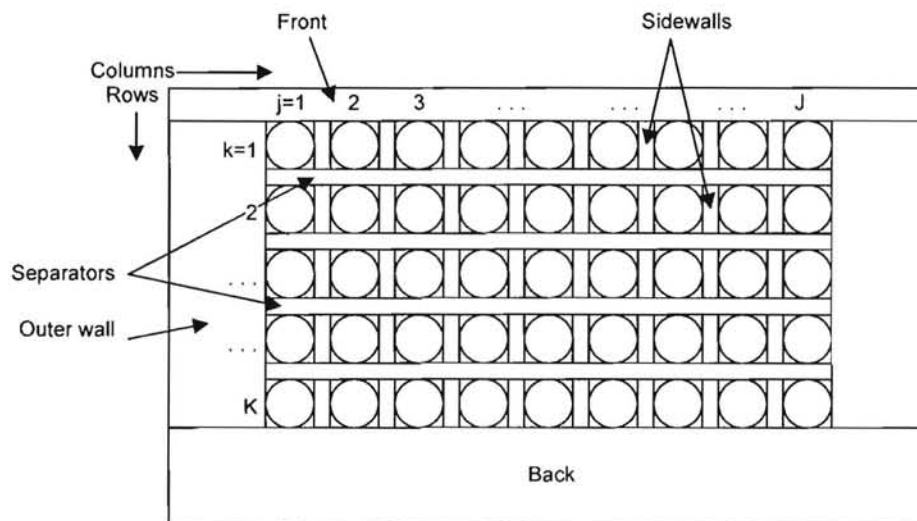
Figure 31: Diagram of an ANDY-type detector, specifying all parameters to be optimized.

4.1 Fundamental principles and parameters

The components and dimensions of the detector array constitute a large

parameter space. This parameter space was reduced by setting the thickness of the

four outer walls and rear slabs to the albedo-limited thickness[24] of 9.5 g/cm^2 (see

Figure 10). The only remaining parameters to optimize are the thicknesses of the

front moderating slab, the sidewalls, and the separators. Limiting the scope of the

---

[23] The term uniform refers to the fact that all the sidewalls are the same thickness throughout the lattice, as are all the separators, etc.

[24] Throughout this chapter the density used for HDPE was 0.95.

study in this fashion allows the remaining parameter space to be completely sampled. Throughout this chapter, the source used was a quasi-plane wave[25] of neutrons uniformly distributed across the entire front face of the detector, including the outer sides. The energy of the neutrons was sampled from a Cf-252 spectrum (see Appendix B).

4.1.1 Total efficiency figure-of-merit

A figure-of-merit (FOM) is defined in Eq. (4.1) to properly compare detectors of different sizes. $FOM_{[m]}$ is the intrinsic efficiency, ε_I, cost-normalized to per liter He-3 at STP in the detector and geometry-normalized by multiplying by the surface area of the detector. The weighting factor m is included to represent the experimenter's preference between increased efficiency and maximally-optimized usage of the He-3 gas.

$$FOM_{[m]} = \left(\overline{\varepsilon_I}\right)^m \cdot A/V \qquad (4.1)$$

A is the surface area of the detector and V is the STP volume of helium-3 present in the detector. For $m=1$ this expression is proportional to the total efficiency times $4\pi R^2 \Omega_{SD}$ and is thus referred to as the *total efficiency figure-of-merit* (see Eqs. (1.7) and (1.8) on page 17). It should be noted that comparison of $FOM_{[m]}$'s having different m is meaningless. To prevent this mistake, m is always denoted as a bracketed subscript. The literal units of $FOM_{[1]}$ are $cm^{-1} \cdot sr^{-1}$; however, since it is impossible to quantify the dimensionless factor m, $FOM_{[m]}$ is described as having

---

[25] The source was uniformly distributed in position and was given initial momentum in a narrow cone having a 1-degree opening angle and central axis perpendicular to the face of the detector.

arbitrary units. This figure-of-merit is invariant with the number of detectors used in

the experiment (assuming zero cross-talk between detectors); therefore it permits

direct comparison of the effectiveness of different detector designs.

4.2 MCNPX simulations

Before proceeding with the optimization process of the full lattice, a simple baseline study was performed. This involved optimizing the response of a single high-pressure tube containing 3 bars of He-3 inside a rectangular parallelepiped of high-density polyethylene.
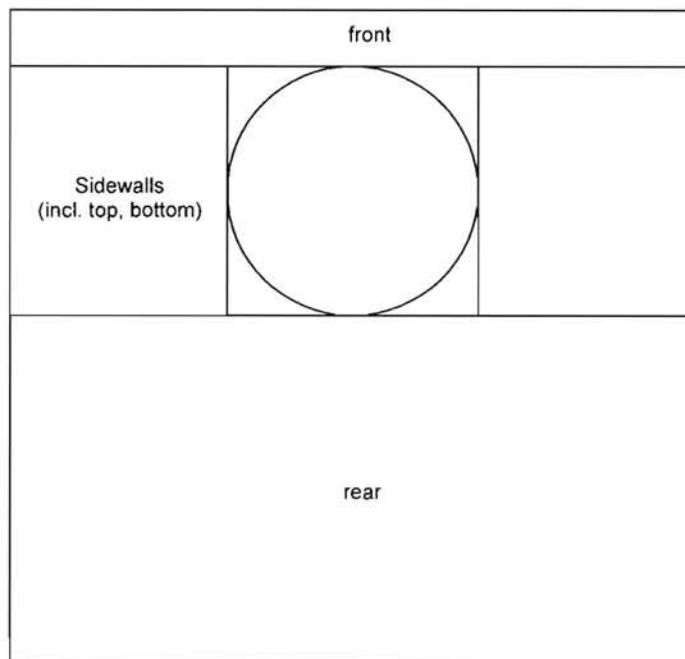
Figure 32: Diagram of the single-tube He-3 detector used for a baseline.

4.2.1 Baseline data: single He-3 tube

A 5-cm diameter tube was used in the baseline simulation which was 300-cm in length and contained 3 bars of He-3. The total volume of He-3 in the tube was approximately 17.3 L_{STP} (0.77 mol). The thickness of the back reflector was chosen to be 9.5 g/cm^2 and the front moderator 0.95 g/cm^2. Figure 33 displays the intrinsic efficiency as a function of the thickness of the four outer sides:
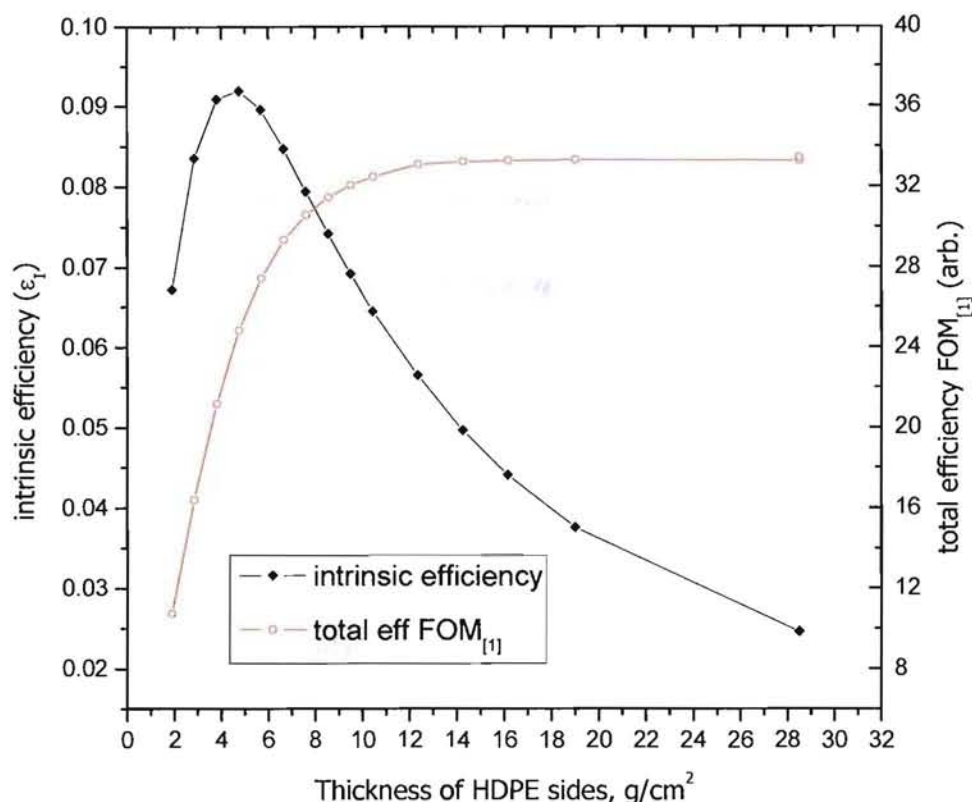
Figure 33: Intrinsic efficiency and total efficiency figure-of-merit (FOM[1]) for a detector consisting of a single He-3 tube. The relative statistical monte-carlo error was less than 1%.

The efficiency for the single 3-bar tube reaches a maximum of about 9.2% at 4.75 g/cm^2-thick outer walls. The figure-of-merit FOM$_{[1]}$ increases monotonically and eventually saturates at about 33.3 above 12.35 g/cm^2. This happens because while the efficiency drops off, the surface area simultaneously increases. The increase in surface area, and hence solid angle, initially dominates, resulting in an increase in FOM$_{[1]}$. As the sidewall thickness is further increased, the two competing factors ultimately reach an impasse and FOM$_{[1]}$ saturates. This presents an interesting scenario to applications such as neutron radiation monitoring: the concrete that is used extensively in laboratories is a very effective neutron moderator; therefore the

most efficient use of a moderated thermal neutron detector is to embed the radiation

monitor directly into the walls and/or floor of the facility.

4.2.2 Optimizing the design of the rectangular ANDY detector

The baseline detector size was chosen to be 320-cm tall by approximately

320-cm wide. The tubes were 5-cm in diameter, 300-cm long, and were placed 20

rows deep in the direction of the incident neutron plane wave. This is an adequate

size to minimize fringe effects from the edges of the detector and thus is

representative of a semi-infinite implementation. These dimensions represent a size

suitable to many homeland security applications while maintaining relevance to the

laboratory regime.

The width and depth of the detector varied as the sidewall thickness and the

separator thickness were changed, respectively. There were always 20 rows in the

detector; however, the number of columns was determined by choosing the odd

number of detectors that made the interior width nearest to 300 cm. Using this

convention there is always a column of tubes centered on the vertical bisector of the

lattice. The goal was to maximize consistency of the detector's response as other

detector parameters were changed. The initial parameters were chosen to be 0.95

g/cm^2 separator thickness and no sidewalls. The detector contained 59 columns of

tubes in this configuration.

4.2.2.1 Front thickness optimization

The front face of the detector plays two important roles: (1) it provides initial

moderation of the incoming fast neutrons, which increases the detector's efficiency, and (2) it reflects incident neutrons via albedo, which decreases the efficiency. The results in Figure 34 show that the loss from albedo dominates, and the detector begins losing efficiency at a front thickness of only 1.425 g/cm^2. The maximum value reached by $FOM_{[1]}$ is approximately 23.0; about 31% less than the single tube. This shortfall is not a cause for concern at this point, as the 20-row model was never assumed to be an optimal design; it merely highlights the fact that the ANDY concept cannot be extended to an indefinite number of rows. The optimal front face thickness was chosen to be 1.5 cm. This thickness results in about 2% less than peak efficiency for this particular configuration; however, the additional thermalization should prove beneficial in the final step--optimization of the number of rows.
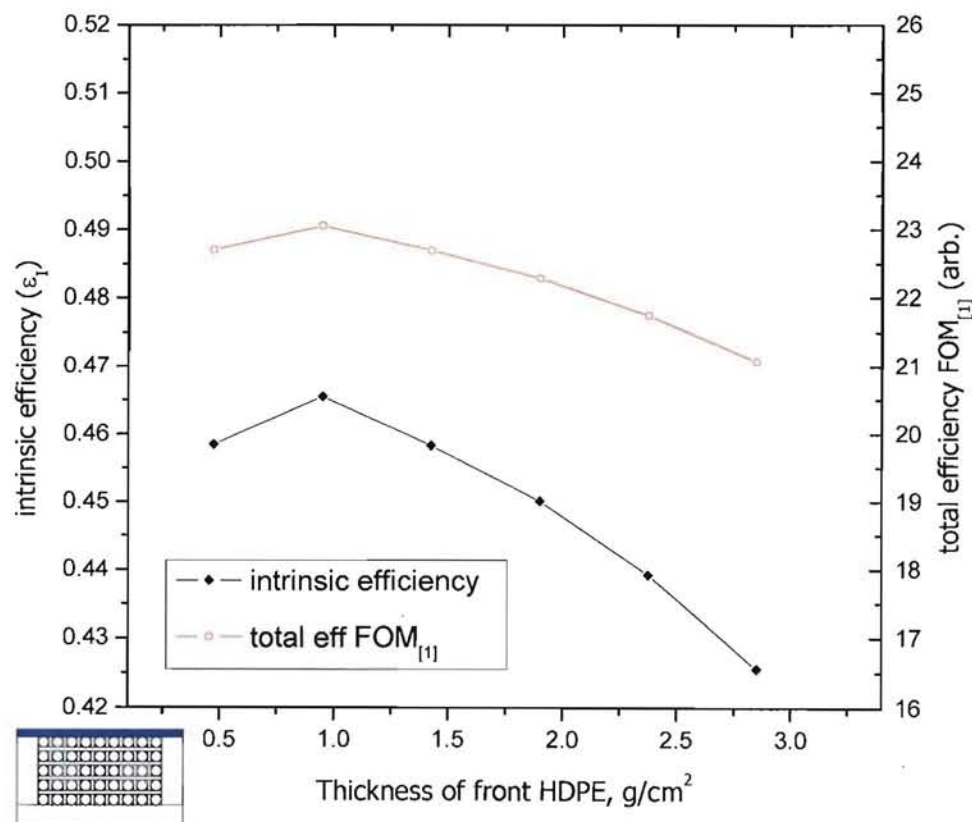
Figure 34: Efficiency parameters vs. front face-thickness for the semi-infinite

ANDY array. The surface area is constant throughout this comparison, and the two curves are identical in shape. The statistical error bars are less than 1%.

4.2.2.2 Sidewall thickness optimization

One would expect an increase in sidewall thickness to create a monotonic

decrease in efficiency, and Figure 35 shows that this is indeed the case. The

sidewalls do provide some additional thermalization, but this is completely

overwhelmed by increased neutron loss to capture on the hydrogen in the HDPE: H(n,

γ)d. However, $FOM_{[1]}$ does not exhibit the same trend because the number of He-3

tubes in each row decreases as the tubes are supplanted by the increasing thickness of

HDPE in the sidewalls. The decrease in He-3 volume results in a net increase in

$FOM_{[1]}$ that produces a broad peak near 0.7125 g/cm^2 sidewall thickness. The number

of columns and the associated detector dimensions are summarized in Table 4.
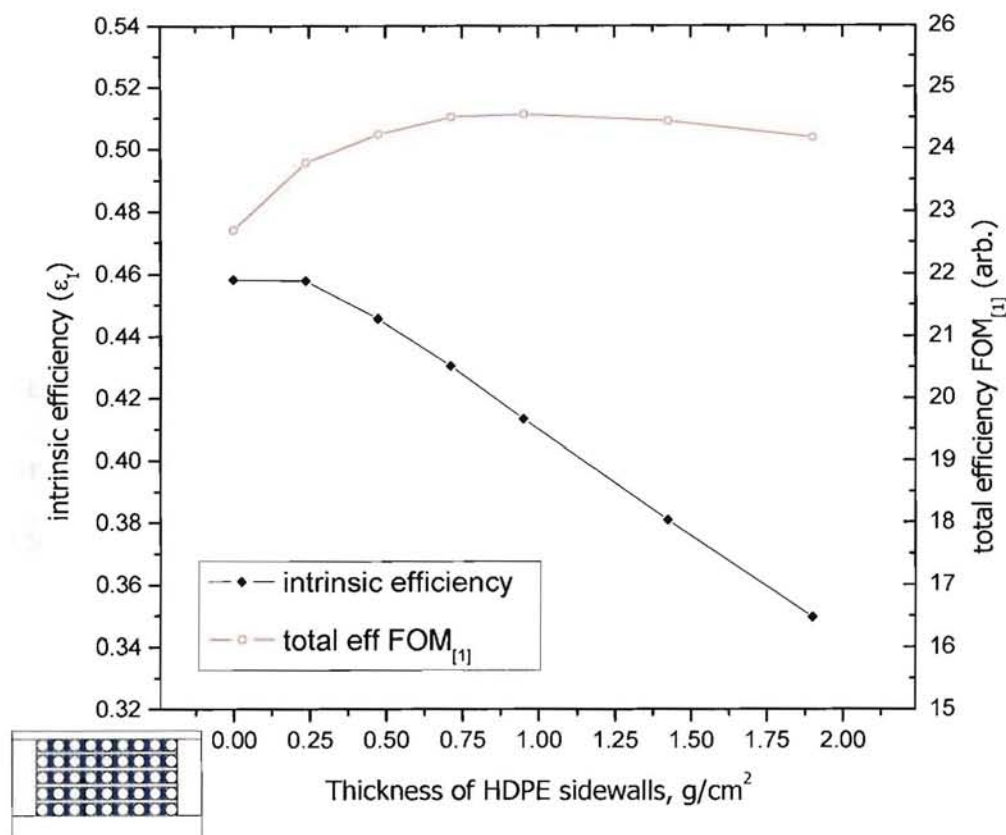
Figure 35: Efficiency parameters vs. sidewall thickness for the semi-infinite ANDY array. The statistical error bars are less than 1%.

Sidewall thickness, cm (g/cm²)	Columns	He-3 Volume (V), L	Total width, cm	Surface Area (A), m²
0.00 (0.0000)	59	102.17	316.18	10.12
0.25 (0.2375)	57	98.71	320.39	10.25
0.50 (0.4750)	55	95.24	323.60	10.36
0.75 (0.7125)	51	88.32	314.27	10.06
1.00 (0.9500)	49	84.85	314.98	10.08
1.50 (1.4250)	47	81.39	326.44	10.45
2.00 (1.9000)	43	74.46	321.86	10.30

Table 4: Detector parameters as a function of sidewall thickness for the semi-infinite ANDY array.

4.2.2.3 Separator thickness optimization

Figure 36 illustrates the results of the separator thickness study. A peak at

$0.475 \ \text{g/cm}^2$ separator thickness occurs because of the semi-infinite nature of the lattice. The outer HDPE box and the gas in the tubes do a fairly adequate job of trapping and thermalizing the neutrons by themselves. Increasing the amount of HDPE in the lattice creates an initial increase in efficiency because of improved thermalization; however, the loss of neutron flux due to increased albedo and neutron capture on hydrogen eventually dominates, and ε_i drops. The optimum thickness chosen to use in the array depth study was $0.7125 \ \text{g/cm}^2$--slightly greater than the thickness that produces maximum efficiency. Just as in the study of the front face thickness, the minor loss of efficiency is expected to be offset by improved thermalization for lattices containing fewer rows.
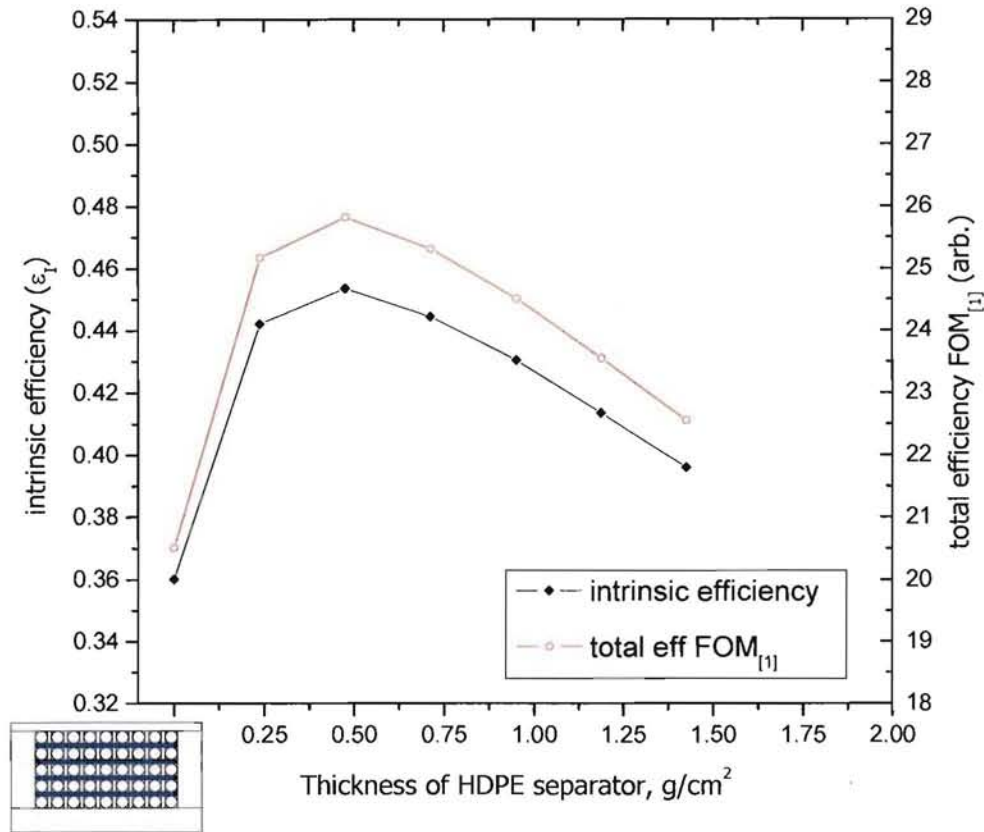
Figure 36: Efficiency parameters vs. separator thickness for the semi-infinite ANDY array. The statistical error bars are less than 1%.

4.2.2.4 Row-by-row study of the separator results

Before proceeding to the array depth study, the results of the preceding

section were analyzed on a row-by-row basis by defining the row-sum efficiency η_k

as the sum of the contributions of all the detectors in a single row:

$$\eta_k = \sum_j \varepsilon_{I\,jk} \tag{4.2}$$

Where $\varepsilon_{I\,jk}$ is the intrinsic efficiency of the individual tube at position (j,k) in the

lattice (refer to Figure 31 on page 63). In Figure 37, each data point η_k thus

represents the sum of an entire row of detectors. The row given by k=1 is at the front

---

of the detector, and row 20 at the back. For zero separator thickness, the count rate is fairly flat with a slight bias toward the front rows of the detector. The frontward bias becomes more predominant as the separator thickness increases. Generally speaking, rows 2-3 experience the greatest count rate and the count rate decreases dramatically toward the rear of the detector. This is a clear demonstration of the lattice concept at work: for a well-moderated ANDY detector, a significant fraction of the incident neutrons are trapped and thermalized in the first few rows. The neutron flux steadily decreases through absorption and leakage through the walls of the detector as the neutrons diffuse into the deeper rows, and the count rate drops accordingly. This suggests that only a few rows of tubes may be necessary to achieve the desired efficiency.
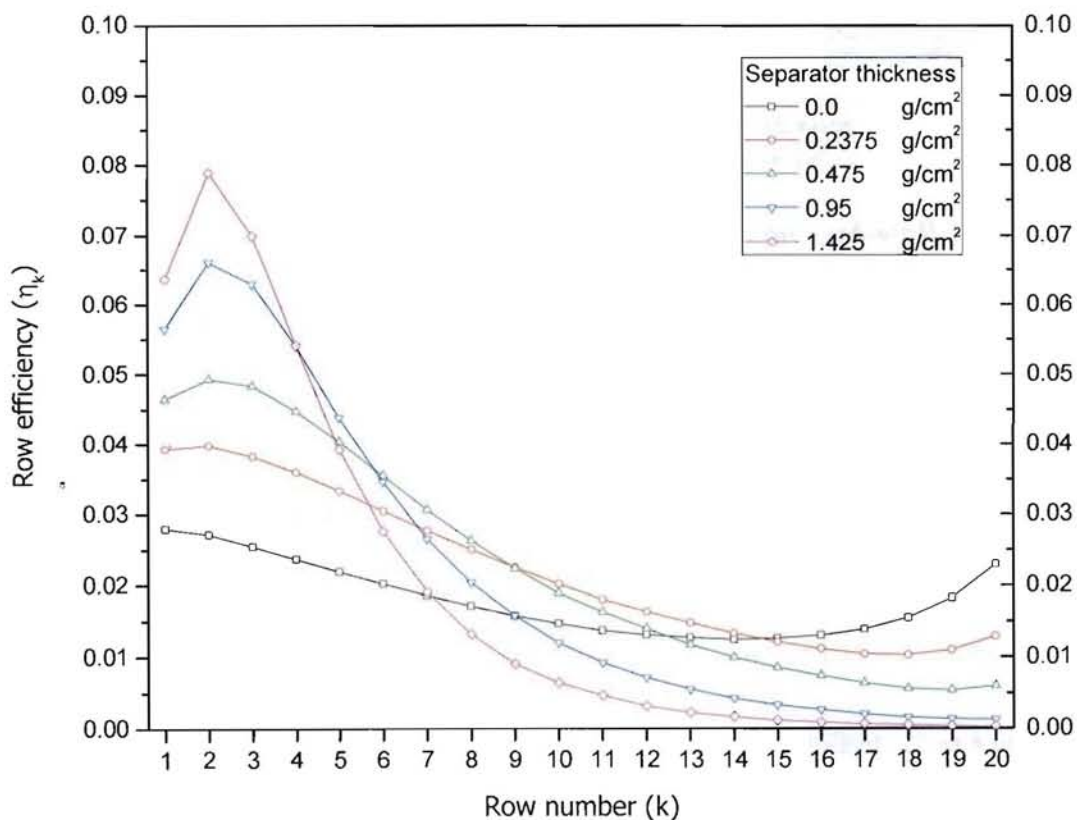
Figure 37: Row-sum efficiencies of the semi-infinite ANDY detector for several

separator thicknesses. Each line corresponds to a particular separator thickness. Each point on the line represents the sum of all the detectors in that particular row. The statistical error bars are less than 1%.

4.2.2.5 Array depth optimization

Figure 38 was produced by modeling several detectors, each containing a specified number of rows of tubes. The results show that approximately 90% of maximum efficiency is reached with only 10 rows. Furthermore, the efficiency for a single row is within a few percent of the optimized single high-pressure tube. While the efficiencies are comparable, the 1-row ANDY design enjoys a huge advantage over the single tube in terms of $FOM_{[1]}$. This is because the low-pressure tubes used in ANDY arrays contain much less gas than old-style single high-pressure tubes. The geometrical interpretation of this is that ANDY-type detectors occupy a much greater solid angle relative to the amount of helium-3 in the detector. In this particular arrangement, the ANDY detector has 21.5 times the surface area of the single-tube detector but only uses 5.1 times as much helium-3, resulting in an increase in $FOM_{[1]}$ of 2.97--nearly 3 times the total efficiency per unit gas.
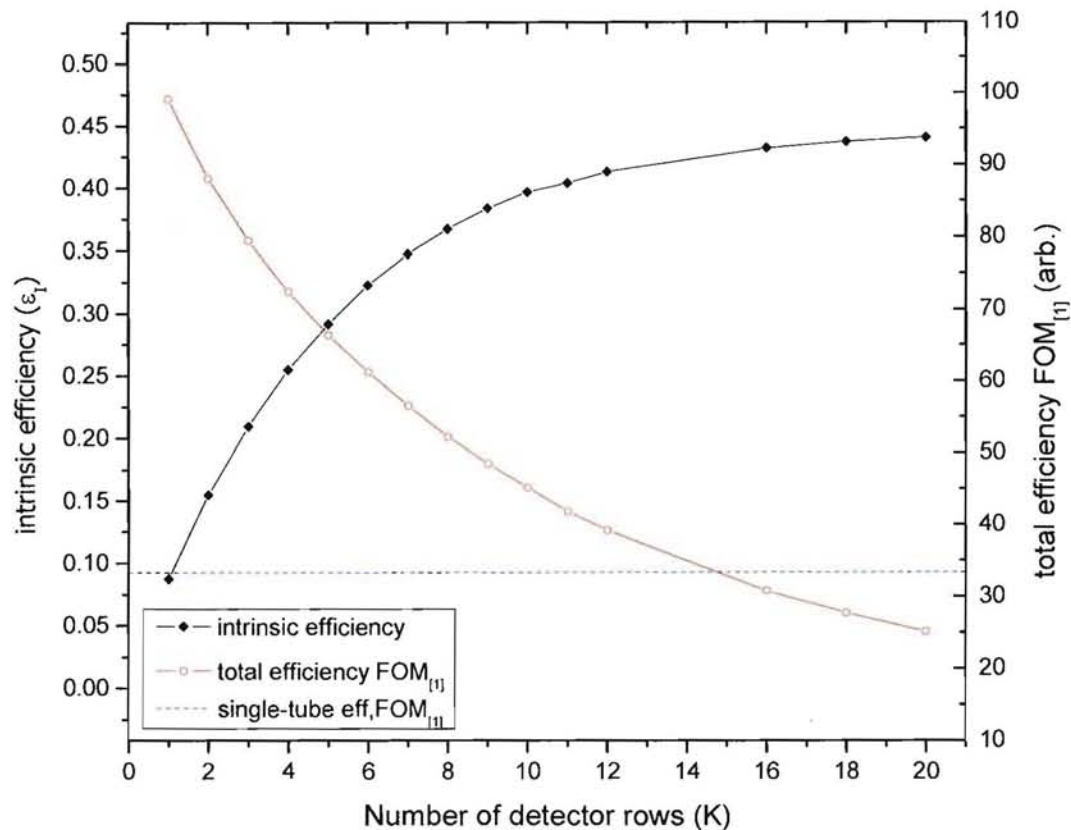
Figure 38: Efficiency parameters versus number of detectors rows for a uniform rectangular ANDY detector. The lattice parameters were identical in each case: 9.5 g/cm² in the top, bottom, rear, and outer sides; 1.425 g/cm² in front; and 0.7125 g/cm² in the separators and sidewalls. The results from the single high-pressure tube of section 4.2.1 appear as a dashed line for comparison; the two y-axes were aligned so the efficiency and figure-of-merit for the single-tube coincide. The statistical error bars are less than 1%.

The figure-of-merit results are somewhat surprising in that the maximum

FOM$_{[1]}$ occurs at a single row. This appears to be in disagreement with the results of

section 4.2.2.4, which suggested that the peak should have occurred at two to three

rows. Figure 39 reveals the discrepancy: the row efficiency increases monotonically

towards the rear of the array for detectors having only a few rows. However, FOM$_{[1]}$

is based on the *average* efficiency of all the rows, which monotonically decreases.

The monotonic increase in efficiency in the rearward direction results from a

combination of the large albedo (>80%) of the thick rear reflector with insufficient

neutron thermalization that stems from the constant-thickness front moderator and

separators that were used throughout this microstudy. To demonstrate this effect, the

four-row ANDY detector was re-optimized to obtain maximum efficiency. The

results are presented in Figures 40-42.
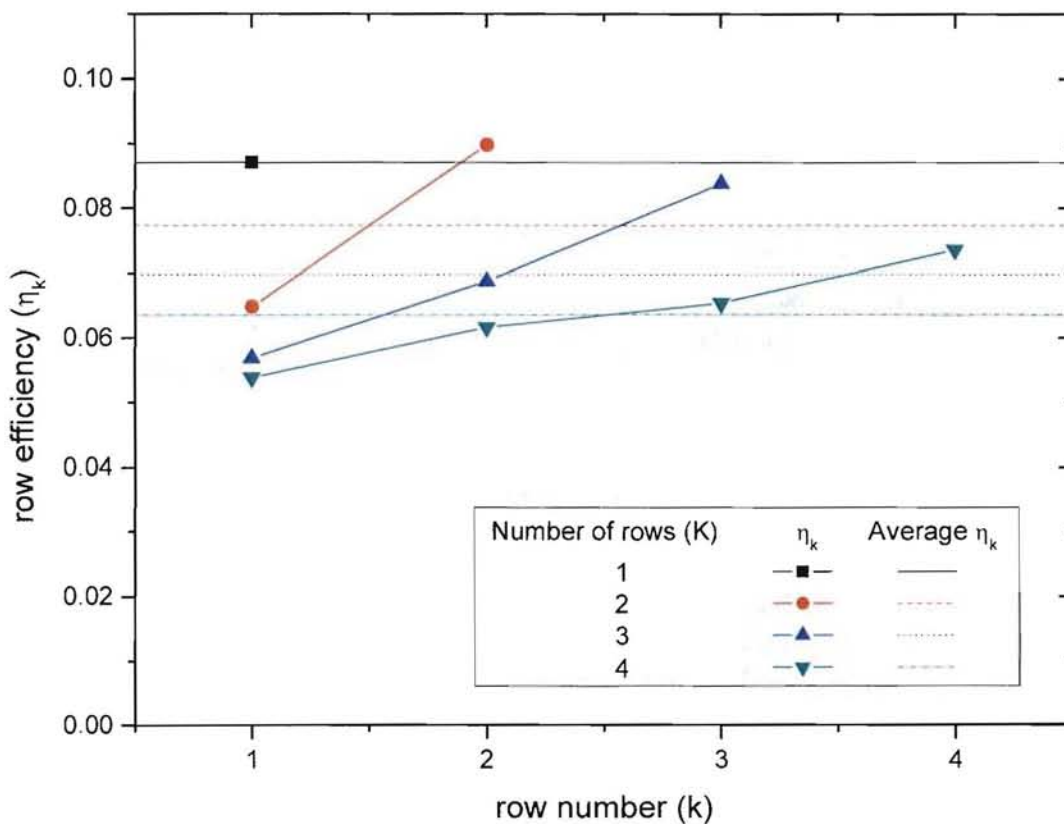
Figure 39: Row-sum efficiency analysis of ANDY arrays containing only a few rows. The average row efficiency for each detector is given by the dashed lines. As always, Row 1 is the front row. The statistical error bars are less than 1%.
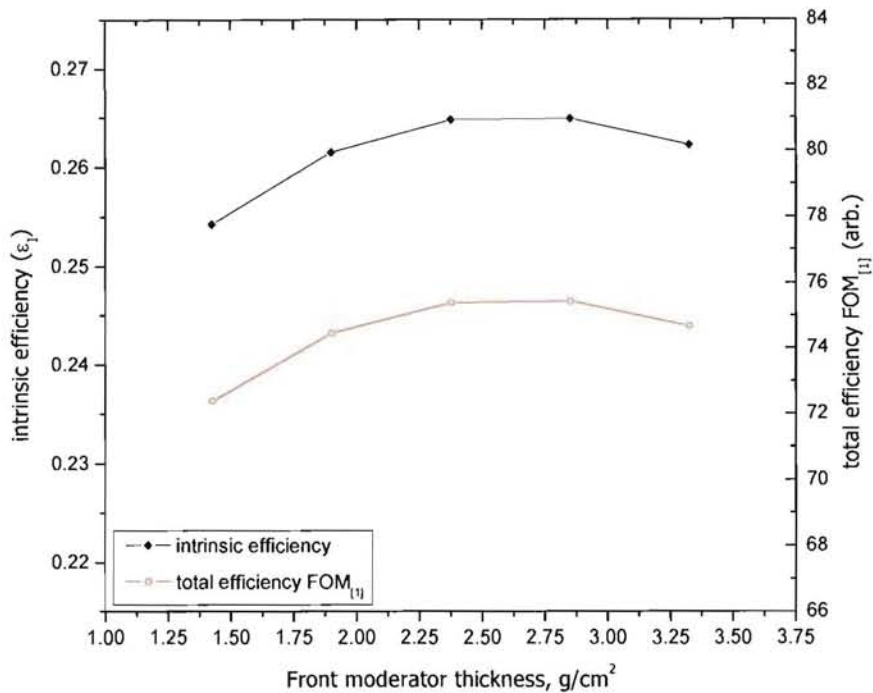
Figure 40: Optimizing the front moderator for the four-row ANDY lattice. The statistical error bars are less than 1%.
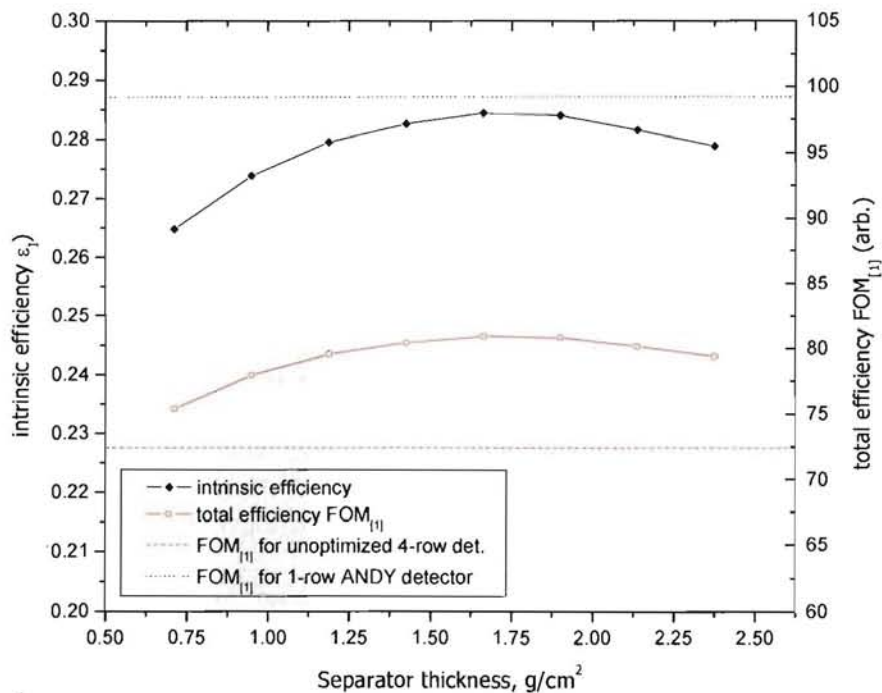
Figure 41: Optimizing the separators for the four-row ANDY lattice. The statistical error bars are less than 1%.
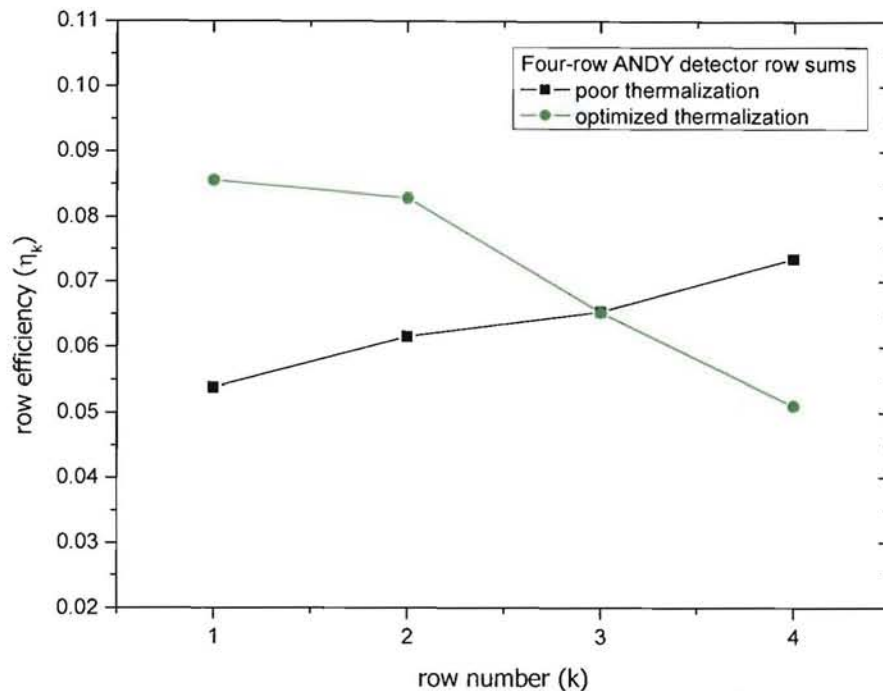
Figure 42: Row-by-row comparison of four-row ANDY detectors: poorly thermalized and optimally-thermalized. The statistical error bars are less than 1%.

Optimization of the four-row detector resulted in a 12% gain in efficiency. This is certainly a significant gain; however, the value of FOM[1] of 80 is still well short of the single-row ANDY detector, which appears as a dotted blue line in Figure 41. This microstudy showed that both the front moderator and the separators were too thin in the configuration used in Figure 38; this is not surprising considering that those parameters were optimized for a much deeper array. Figure 42 shows a dramatic difference in the location of neutron capture events after optimization. The slope of the row-by-row efficiency curve changed sign. It should also be noted that in the optimized four-row array, the efficiency of rows 1 and 2 are within a few percent of each other. While these results are not intended to be all-inclusive, they do provide

insights that will be quite valuable to designers of real-world ANDY arrays.

However, the analysis of these results is not yet complete; recall from section 1.3 that

many experimental scenarios call for increased emphasis on efficiency. The impact

of this concept applied to the ANDY array is described in the following section.

4.3 Application to real-world configurations: the row-cost FOM

The implication of the results presented in Figure 38 when applied to real-

world scenarios is clear. The maximum utilization of the He-3 gas is optimal with a

single row of detectors, and any required increase in count rate should be realized by

adding detectors to the ends of the array. However, this solution may not be desirable

for many applications due to space constraints or aesthetic and/or logistic

considerations (consider a large-scale example, a detector 18 cm deep and 100 meters

long!). Thus it will frequently be preferable to increase efficiency by adding

additional rows to the detector. From a design standpoint, this scenario is equivalent

to stating that the intrinsic efficiency is more important than the solid angle. This can

be realized mathematically by adding a *second* weighting parameter, *n*, to the figure-

of-merit expression:

$$FOM_{\{mn\}}^{(m)} = \left(\overline{\varepsilon_I}\right)^{m \cdot n} \cdot A/V \qquad\qquad (4.3)$$

This figure-of-merit is used to optimize the number of rows in the ANDY

detector. It is thus referred to as the *row-cost figure-of-merit*. To reiterate, *m*

represents the relative emphasis between efficiency and amount of He-3 gas used, and

n represents the relative emphasis between efficiency and solid angle. Obviously, Eq.

(4.3) is mathematically equivalent to (4.1); however, both m and n are retained to emphasize the fact that the two weighting factors are distinct conceptual quantities. The parentheses in the superscript of $FOM^{(m)}_{\{mn\}}$ suggest that direct specification of m is optional. With this consideration, the subscripted square brackets of Eq. (4.1) have been replaced by curly braces in (4.3) to distinguish the otherwise potentially identical forms.

The combination of m and n into a single parameter could result in under-emphasis of the intrinsic efficiency. For example, a weighting factor of 3 represents a fairly extreme bias, and a practical-minded designer may be tempted to reduce the factor. However, the results of this strong single bias are identical to the results given by the product of the two conservative factors $m=1.5$ and $n=2$, which represent a slight bias in favor of efficiency versus the amount of gas used and a moderate bias versus the surface area of the detector, respectively. Therefore, $m \cdot n = 3$ yields the desired result. To further emphasize the distinction between m and n, one should recall that while both are used to finalize a real-world design, only m was used in selection of the He-3 partial pressure.
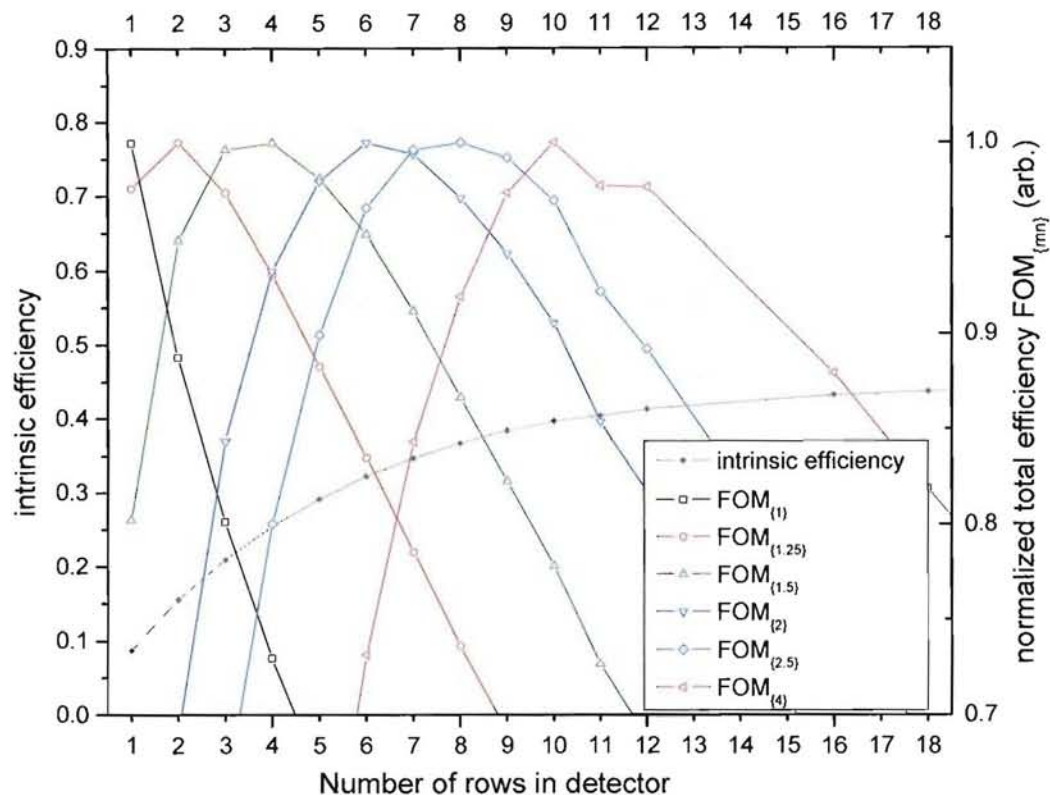
Figure 43: Row-cost efficiency figure-of-merit FOM$_{\{mn\}}$ for ANDY detectors in various efficiency scenarios. The statistical error bars are less than 1%.

For most real-world applications, m and n are both expected to be modest; the total weighting factor $m \cdot n$ will typically lie in the range 1.5-2.5. Figure 43 shows that the optimum number of rows in these circumstances for the array consisting of tubes containing 300-mbar helium-3 is 4-8. This corresponds to an intrinsic efficiency of 30-35%. The reader should keep in mind that while the 300-mbar level is considered a good starting point for demonstrative purposes, the true optimum may involve more or less partial pressure of He-3 gas. The study of this final application-dependent optimization parameter is left to the designer.

Comparing the row-cost efficiency figure-of-merit results of Figure 43 to the

single-tube detector shows that the single tube initially gains ground as the emphasis on efficiency is increased (see Figure 44). However, when cost is truly no object (represented by the regime $m \cdot n > 3$), the ANDY design is even more dominant than the purist viewpoint ($m \cdot n = 1$). This remarkable result suggests that virtually any real-world neutron detector design that relies on external thermalization could be improved by implementing the ANDY concept.
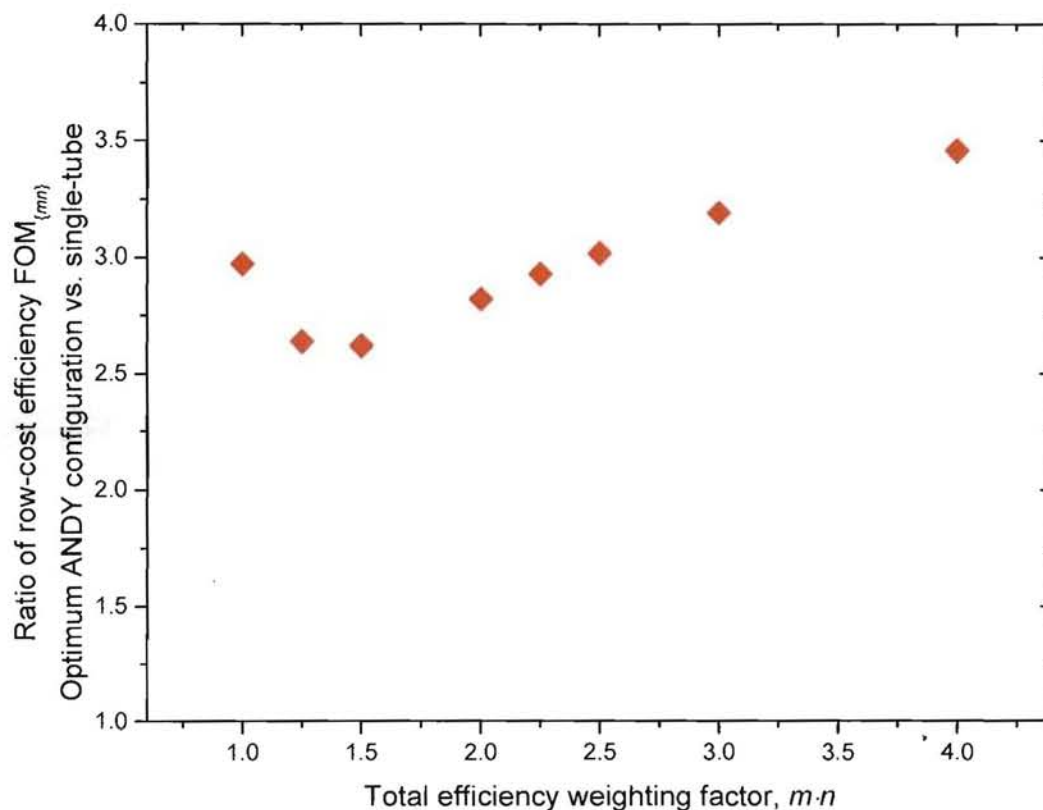
Figure 44: Improvement in row-cost efficiency figure-of-merit for ANDY detector over single-tube detector. Several efficiency-weighting scenarios are presented. The number of rows in the various ANDY detectors used in each weighting scenario is the optimum number prescribed by Figure 43. The statistical error bars are less than 1%.

Chapter 5 : Prototype development

A prototype detector was constructed at LANL for the purposes of

benchmarking the results of Chapter 4 and providing a portable, high-efficiency,

large-area neutron detector suitable to conducting future standoff interrogation

experiments at LANL and Brookhaven National Laboratory (BNL). The final design

represents a compromise between cost, portability, recommended dimensions of the

lattice, and efficiency required by the experiments.
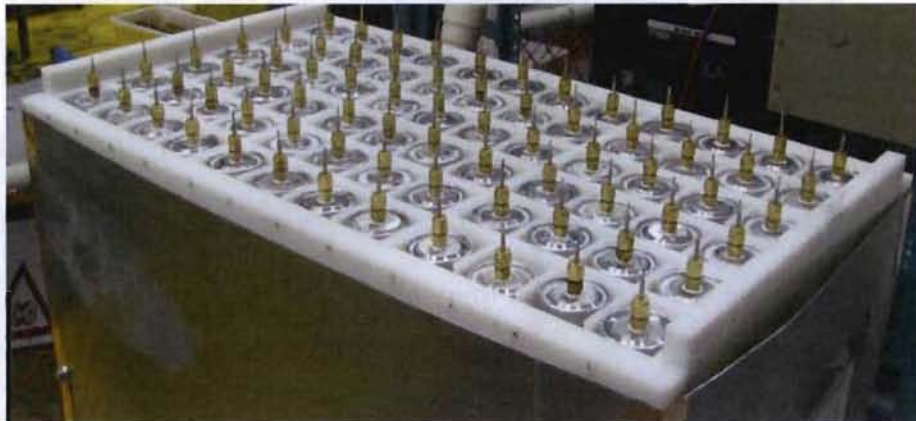
Figure 45: The ANDY prototype detector in the laboratory at LANL, containing 72 tubes arranged in a 6 row by 12 column lattice.
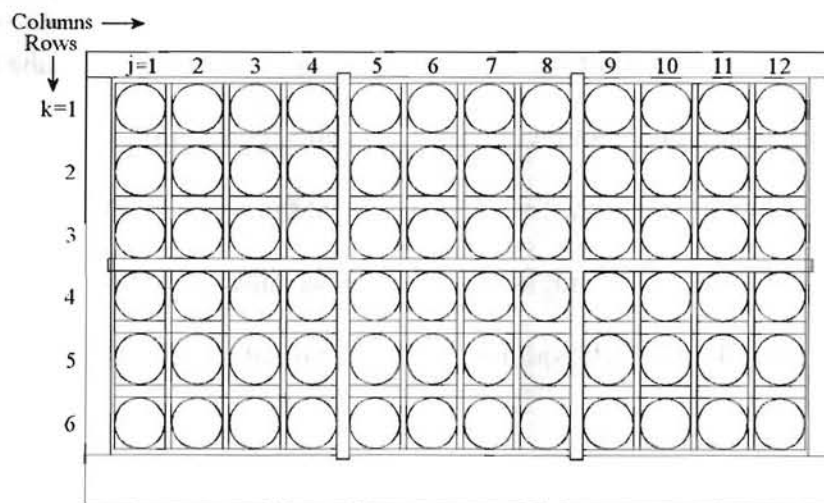
Figure 46: MCNPX model of the ANDY prototype. The top face in the MCNPX model is the front face.

5.1 Detector construction

The helium-3 detectors were built at LANL using a design emphasizing robust and inexpensive construction. The basis for the design was one that has been used successfully for constructing proportional counters up to 6.1-m in length for the ongoing development of a muon radiography and tomography system at LANL [45, 46, 47]. The detectors consist of an aluminum tube 5.08-cm in diameter that has been sealed at both ends with welded aluminum caps. The central wire is 35-micron diameter gold-plated tungsten stretched to 50g tension. The dual anode connections (top and bottom) are provided via copper tubes 0.15875-cm in diameter that are crimped onto the central anode wire. Thus the tubes can readily be adapted to position measurements using the time difference between the signals arriving at the two ends. The anodes are insulated from the housing by polyetheretherketone (PEEK) tubing.

Swagelok fittings inserted through threaded holes in the caps provide airtight seals at the Swagelok-PEEK and PEEK-anode interfaces. One end of the tube has a tee and a second Swagelok fitting. This fitting holds a second copper tube that provides the gas interface (not pictured). The ground connection is made by tightly looping copper wire around the Swagelok fitting at the small gap between the base of the fitting and the cap. The simplicity of this design allows the detectors to be easily assembled using off-the-shelf equipment at a fraction of the cost of retail industrial detectors.
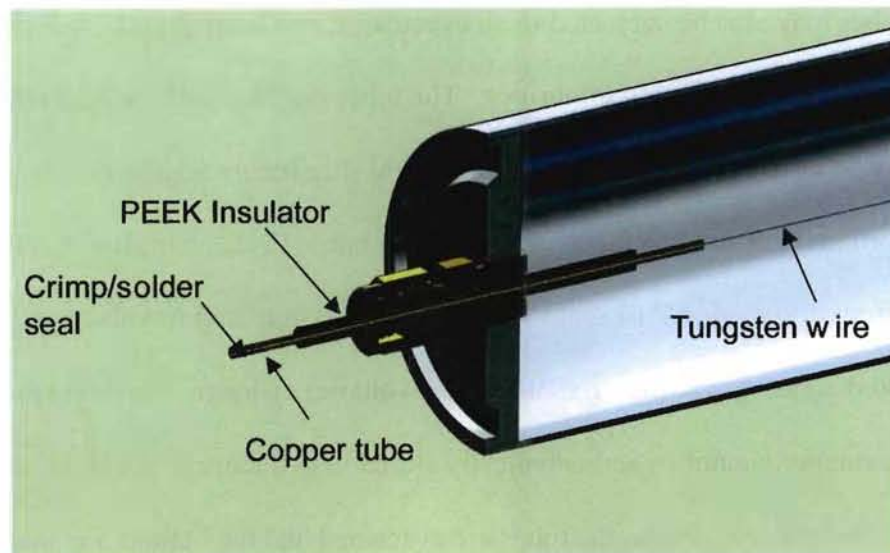
Figure 47: Schematic view of detector construction.

After the tube assembly is complete, the gas-fill and quality control processes are conducted simultaneously in an integrated fashion. First, the tension in the anode wire is verified with an oscillation test. In this test, a magnet is placed near the detector to create a magnetic field gradient. The wire is caused to vibrate by gently striking the tube with a knuckle or rubber mallet. The fundamental frequency of the wire's vibration is proportional to the square root of the tension in the wire. The wire's motion through the magnetic field induces an oscillatory electrical signal in the wire. The frequency of oscillation is measured with a digital oscilloscope that has built-in fast fourier transform (FFT) capability (Tektronix TDS3000B or similar). Several harmonics are excited during this test. The precision of the measurement can be increased to better than 1% by fitting several of these harmonics.

Next, the detectors are connected to a custom-built gas filling station that allows up to 60 tubes to be filled and leak-checked simultaneously. The first step in this process is leak checking with ordinary Helium. During the leak checking process

the tubes may also be subjected to an evacuation and heating cycle, which assists in

the removal of outgassing impurities. The tubes are then high-voltage tested to

5000V to insure proper isolation of the anode wire before adding the fill gases. The

proportional gas is a proprietary mixture of ethane (C_2H_6), tetraflouromethane (CF_4,

industrial designation R14), and Argon. The gas is ordered premixed and arrives in a

standard welding-size (approx. 50L water volume) cylinder. Helium-3 is ordered in

much smaller quantities and is typically stored in cylinders about 1L in water volume.

Following the leak check, the tubes are evacuated and the helium-3 is inserted. The

helium-3 is added first to avoid pollution of the remaining He-3 in the cylinder. Next,

the helium-3 cylinder is closed off from the rest of the system and the proportional

gas is added. Using this method it is impossible to prevent some loss of helium-3 into

the proportional gas cylinder. The loss is minor, however, because of the large

pressure difference between the filling station and the gas cylinder. After the desired

pressure is reached, the copper fill tube is closed with a crimping tool and any excess

copper tubing is trimmed off. The tip of the tube is then given a secondary seal with

a layer of solder. A final leak check is performed by immersing the tips of the copper

fill tube and anode tubes in water. If no bubbles form, the tube is ready to go into

service.

5.2 Array construction

The prototype consists of 72 helium-3 tubes arranged in a 12 x 6 rectangular

lattice. Based on the results of Chapter 4, the design of this lattice emphasizes

efficiency fairly strongly. Portability was also a significant factor in choosing the

dimensions; the detector is typically placed on a wheeled cart and the 12 x 6 lattice

provides enhanced stability as it is rolled about the laboratory. Each tube is 5.08-cm

in diameter, roughly 121.92-cm long, and contains 200 mbar He-3 and 800 mbar

proportional gas for a total internal pressure of 1 bar. The dimensions of the outer

box were selected to minimize weight while not unnecessarily sacrificing efficiency.

The top, bottom, front and side HDPE slabs are 2.54-cm thick and the rear is 5.08-cm.

The top and bottom slabs are drilled through to allow the anode connections and fill

tube to pass through. There is a 3.81-cm air space and additional 2.54-cm base below

the bottom slab. The open space is reserved for custom electronics that will be

installed at a future date[26]. The top area is open save for six aluminum project boxes

that provide connection points for high voltage and ground wires. The entire detector

is encased in a 0.762-mm thick aluminum faraday shield to reduce electronic noise.

---

[26] Planning for the electronics-addition project is currently underway; it is slated to begin in June 2010, pending funding.

UNCLASSIFIED – ADC Review by Alexander Saunders, P-25, on 3/23/2009

Fully-assembled prototype　　　　　　Outer egg crate with base　　　　Inner egg crate
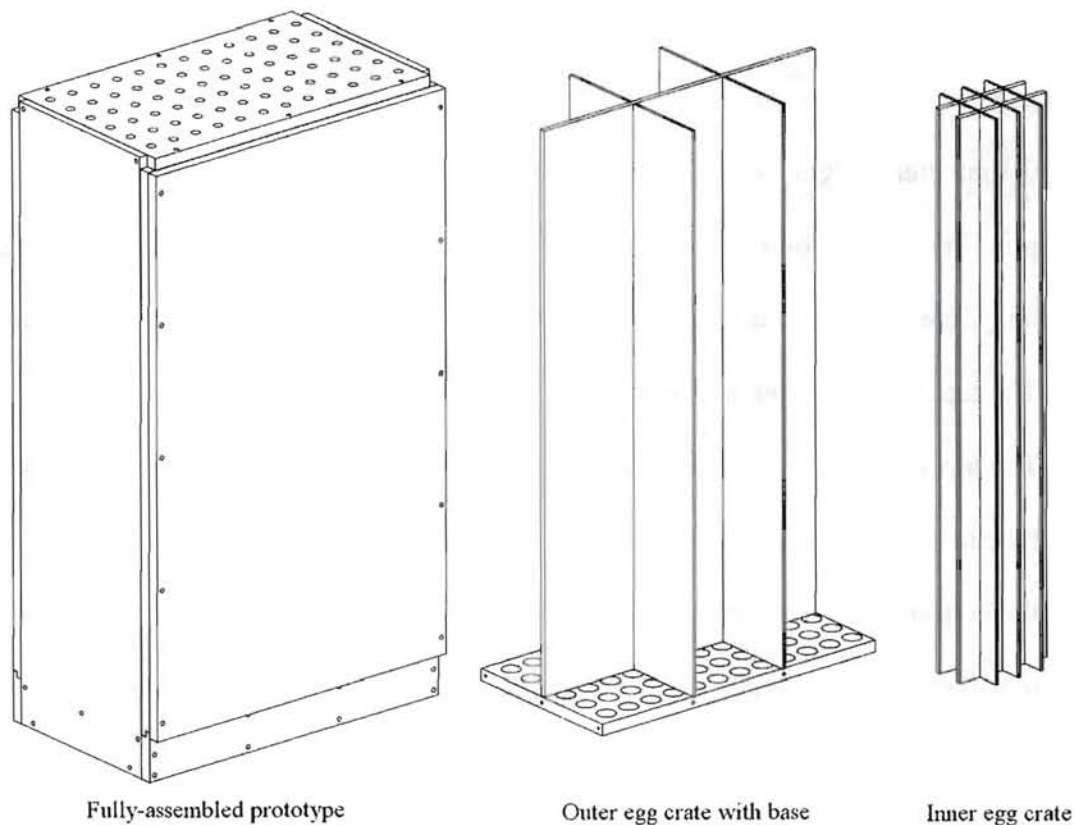
Figure 48: ANDY Prototype assembly

The lattice is comprised of nested structures of HDPE sheets that interleave in a similar fashion to old-style egg crates. Each sheet is cut through to its midpoint lengthwise to allow the sheets to slide together and form a structure without gaps. There are six inner "egg crates" that hold 12 tubes each, made from 0.635-cm and 1.27-cm thick sheets arranged in a 3x2 pattern. The larger outer egg crate is made from 1.27-cm thick sheets[27] arranged in a 2x1 pattern to hold the six inner lattices. This design facilitates very rapid assembly of the detector. Each egg crate can be assembled and stood upright by a single person. This allows the egg crates to be

---

[27] The design specification actually called for the two sheets aligned front-back to be 0.635-cm thick, so that all the sidewalls were the same thickness. A mistake made by the third-party fabricator led to this result.

assembled independently while the outer box is being bolted together. The large egg crate is placed on the detector base and the four outer walls are closed. The small inner egg crates are light enough to be lifted above the walls of the detector and gently dropped inside by a single person. A team of three workers can assemble the entire HDPE lattice structure in a matter of minutes. The fully-assembled weight of the detector, including helium-3 tubes, is about 300 kilograms. The true beauty of this lattice design is that it scales easily to facilitate building detectors of almost any size.

5.3 Electronics and readout

Data collection for the ANDY prototype is greatly simplified by combining groups of tubes in parallel. This is done by simply daisy-chaining the high-voltage and ground connections. The number of tubes that are combined and their positions in the array depend on the data that is desired. Typically, all 72 tubes are connected into one signal to facilitate gross count rate monitoring with a single data acquisition (DAQ) channel. Other experiments dictate different detector combinations; for example, 12 tubes comprising one entire row were connected to obtain the row-by-row benchmarking data of sections 6.1 and 6.2.
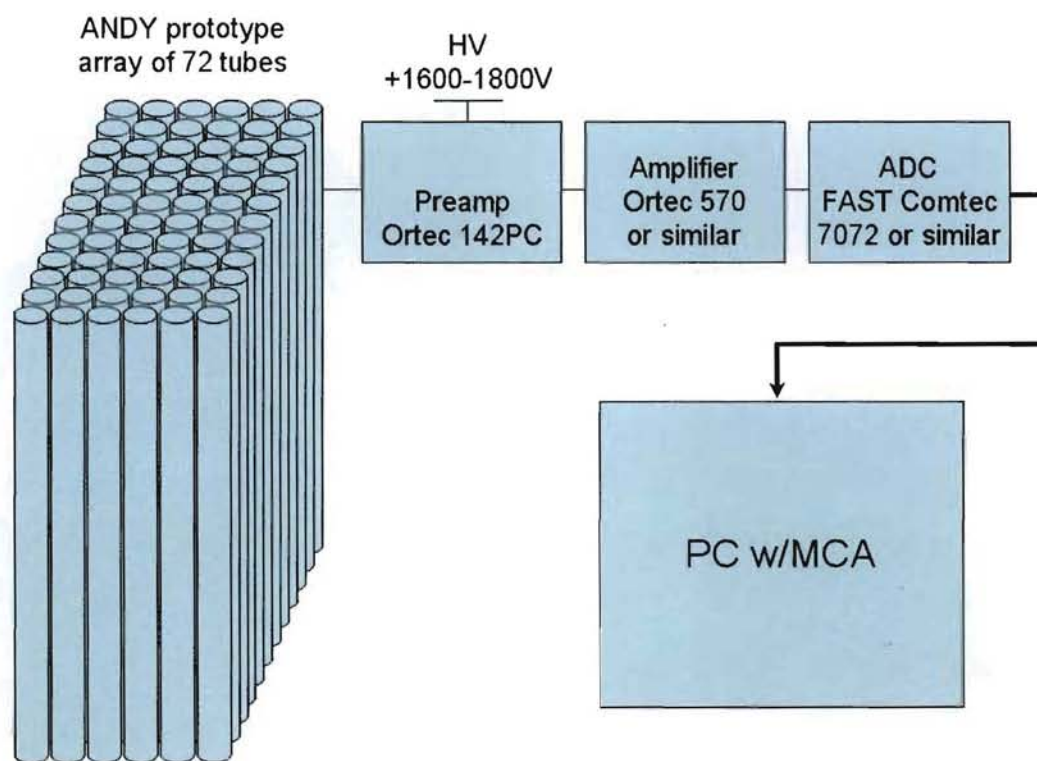
Figure 49: Electronics used in recording neutron counts from ANDY prototype detector. Groups of He-3 tubes are connected in parallel and recorded as a single channel using standard NIM electronics.

The benefits to this technique are clear: standard NIM instrumentation can be used; only one set of electronics needs to be set up; and standard histogramming software can be used to record the data, which results in simple and straightforward output files. There is no need to set up and calibrate complicated multichannel instruments or program elaborate data acquisition routines. There are drawbacks to this method, however:

- The proportional counters must be gain-matched, as there is no independent gain control for individual tubes. Each tube is independently efficiency-calibrated prior to installation in the array and any outliers are discarded. After a matched set of tubes has been selected and installed, the neutron counts form a single, slightly rounded peak in the energy spectrum (see Figure 50). This peak plays the same important role as with a single tube; it allows the experimenter to identify neutron events and discriminate them with a lower-level threshold. The system is insensitive to gain changes on the order of a few percent because of the roundness in the peak. A gain drift is considered problematic when an additional peak appears in the spectrum. At this point, a single lower-level threshold may not be sufficient to discriminate neutron events. In the event of such a failure, each tube would have to be re-tested on an individual basis. Testing is a quick process that does not require the tubes to be removed from the lattice. Any anomalous tube(s) can also be replaced without disturbing the other tubes in the array.

- A more robust DAQ system would count each detector individually. The system currently used is count-rate-limited compared to such a system, in that pileup

occurs if multiple tubes detect neutrons simultaneously. Many of these pileup events could be recovered by implementing additional lower-level threshold(s) above the primary neutron peak and multiplying counts in this region by the appropriate factor (2, 3, etc). However, this correction becomes increasingly inaccurate as the pileup increases and it is preferable to limit the count rate so only single-count events occur.
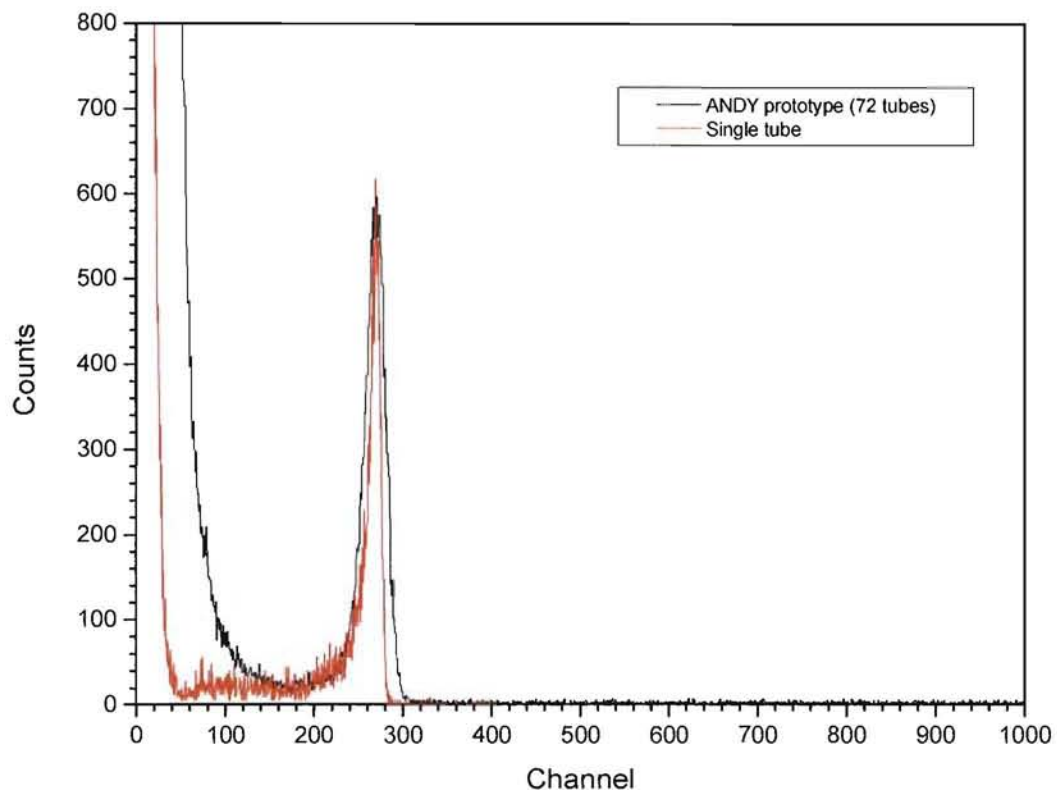
Figure 50: The pulse-height spectrum from the ANDY prototype with all 72 tubes in parallel compared to a single He-3 detector. The spectrum is considerably noisier than the single-tube spectrum but the neutron peak is still clearly resolved.

- Another count rate limitation occurs in the form of increased saturation recovery time. When a proportional detector receives an overwhelmingly large burst of radiation, the voltage in the tube is depleted and the tube is said to be in saturation.

The bias voltage is typically quickly replenished in a matter of microseconds to milliseconds by capacitive storage. During the initial recovery phase the detector is operating proportionally, but at reduced gain. Recovery time is exacerbated in this system because of the large number of detectors that need to be "recharged" and the varying degree of depletion. The tubes at the front of the detector experience greater depletion and longer recovery time than the tubes at the rear because the rear tubes are partially shielded by the additional HDPE layers in front of them. The causes the neutron peak to appear "smeared out" because the tubes are not all operating at the same gain. The data cannot be considered valid until all tubes have recovered and a single, cohesive neutron peak appears. During recent proton interrogation experiments conducted at LANL the recovery time for the ANDY prototype was several seconds at a 30-m distance, while that for a single 2"x12" He-3 detector at a distance of 1m recovered in a few milliseconds.

- Experiments involving multiple groups of detectors (such as sections 6.1 and 6.2) require repeated measurements. Repeatedly switching detector connections to perform multi-group measurements takes time and is potentially hazardous to the experimenter and the detectors themselves. The anode connections on the detectors are somewhat fragile and due to the finite capacitance of the tubes the experimenter must take care that they are completely drained of charge or (s)he may receive a small but unpleasant shock. The anode connections are also fairly sharp and superficial scratches can occur if they are carelessly brushed up against. While the potential for accident is low when proper precautions are taken, it would still be preferable to eliminate the risk altogether by implementing a multichannel counting system that

does not require the detector lid to be removed.

The drawbacks discussed above make it desirable to develop the capability to record each detector individually for long-term use of the detector. However, the daisy-chain method is perfectly satisfactory for occasional use around the laboratory, particularly when the count rates are modest. It is much more convenient for the experimenter to quickly set up a simple single-channel acquisition system than to deal with a complex 72-channel data acquisition system and struggle to re-learn the nuances that are always present in such systems. Therefore, despite the limitations of the existing method, development of such a system has been given a low priority up to this point[28].

---

[28] See footnote 26 on page 88.

Chapter 6 : Experimental results

Two benchmarking experiments were conducted to verify the ability of the MCNPX code to predict the performance of the ANDY prototype detector at LANL.

6.1 Individual tube position efficiency measurement

In the first experiment, the efficiency was measured at each of the 72 detector positions using a Cf-252 neutron source inside an HDPE source holder attached to the front of the detector. Several precautions were taken in order to maximize the consistency throughout the experiment: First, the source holder was keyed so it could only be attached in one position, ensuring precise repeatability in the source position between all measurements. Second, all of the available He-3 tubes were counted individually and twelve were selected that had the closest-matching efficiency. These twelve tubes were then inserted into row six—the back row of the lattice. The tube in column A was counted both with and without the source. Then the tubes in columns A and B were switched and column B was counted. Then B and C were switched, and so on. Hence, the exact same helium-3 tube was used at every position. The twelve tubes were then moved into row five and the process was repeated. This procedure was repeated for the remaining four rows, again continuing to use the same tube for each measurement. As a final precaution, another helium-3 tube was placed 10m from the apparatus to provide an independent measurement of the background rate. This was important because the signal-to-noise ratio for the tubes having the lowest count rates was less than 2:1. The background rate did not vary throughout the

experiment.
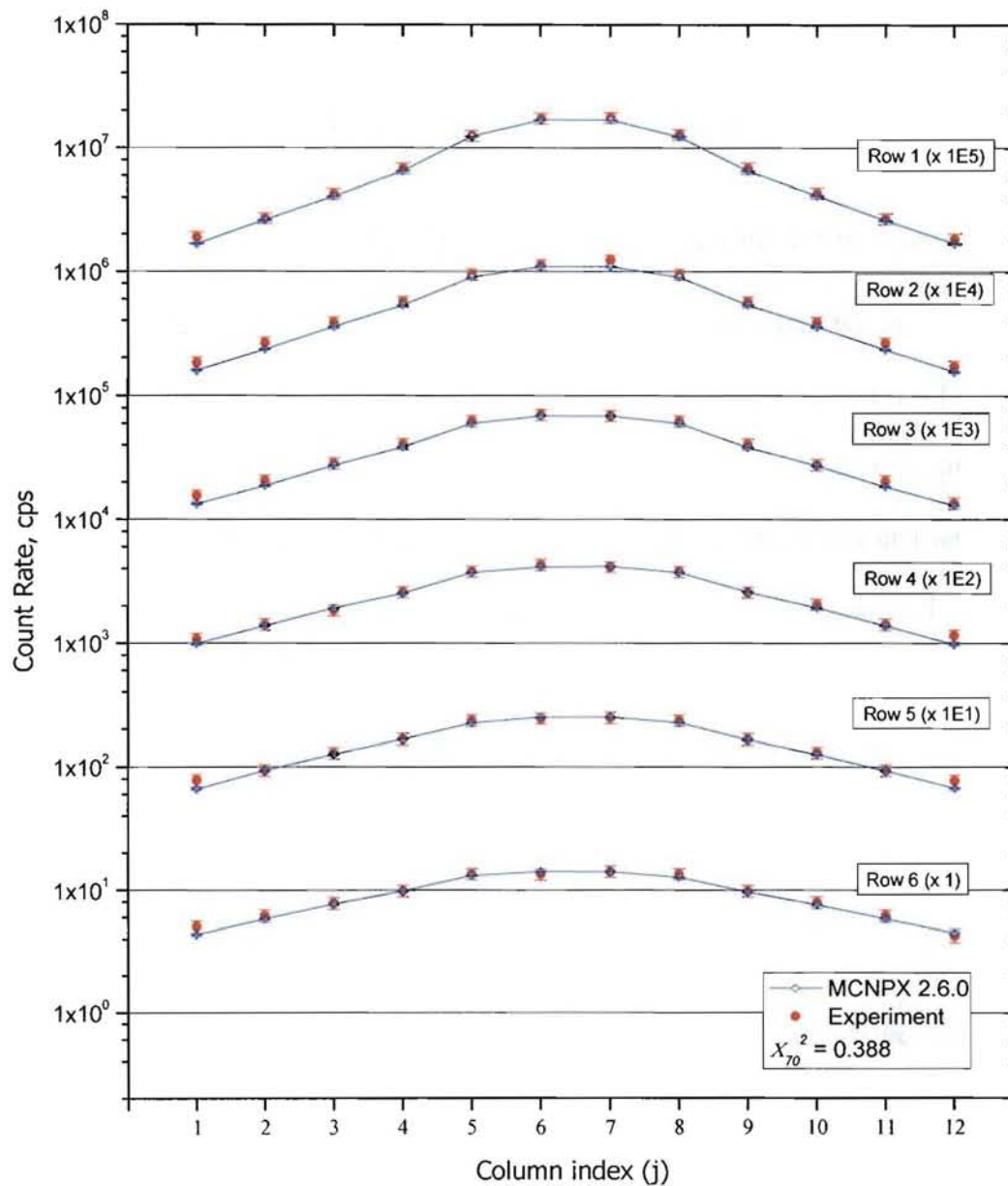
Figure 51: Results of individual-tube efficiency measurement. The results are presented in rows, with each successive row separated by a decade for clarity.

Figure 51 shows the excellent agreement between the experimental data and

the MCNPX model. The reduced chi-squared value of 0.388 suggests that the

assumed 10% error in the source activity may be excessive. Overall, the

experimental values are higher than the MCNPX predictions by 6.1%. This result is

consistent with section 3.3.3, where the empirical data was 9.0% greater than the

code. Renormalizing the data[29] using the average correction factor of 1.076 and the

3.9% relative error from section 3.3.3 results in a new reduced chi-squared value of

0.98. This strongly supports the assertion that the MCNPX code has sufficient

precision to perform independent calibration of neutron sources for these types of

experimental models.

The experimental curves also appear to be slightly flatter across each row,

which is consistent with the results of section 3.3.4. While these deviations are not

statistically significant, such consistency suggests that something is not entirely

correct in the model. Several factors could create a minor effect such as this.

Possibilities include incorrect HDPE density; incorrect treatment of thermal neutrons;

air temperature, density, and/or humidity; or approximations in the geometry, to name

just a few. The important thing, however, is that these results prove that the code is

able to predict efficiencies of helium-3 detectors within a few percent. This level of

precision is certainly suitable to facilitate high-fidelity planning of very sensitive

experiments.

---

[29] A plot of the renormalized data is indistinguishable from Figure 51 and is not shown.

6.2 Single-row efficiency measurement with full array

The purpose of the second experiment was twofold: (1) verify the MCNPX-predicted efficiency of the ANDY prototype, and (2) benchmark the code in a more difficult experimental environment. To achieve the latter, the prototype was placed in the high-resolution-spectrometer (HRS) dome at LANSCE Area C at LANL. The HRS dome is a 14-m radius circular concrete room capped with a 0.46-m thick hemispherical concrete dome[30]. The dome is covered by a compacted-earth berm that is 3-m thick at its thinnest point. The cylindrical walls have three penetrations that provide beam entry, beam exit, and truck access. The truck access tunnel is not depicted in Figure 52; it comes out of the page at about a 20 degree angle to the normal. All three penetrations are approximately 5m wide by 5m tall. The area is an active experimental area and is filled with massive objects such as magnets and stacks of shielding blocks. This construction creates a very complicated neutron scattering trap that is ideal for a sensitivity study of efficacy. The detector was placed on a wooden cart 13.3 cm high and located about 5 meters from the nearest concrete wall.

---

[30] Given dimensions for the HRS dome are approximate.
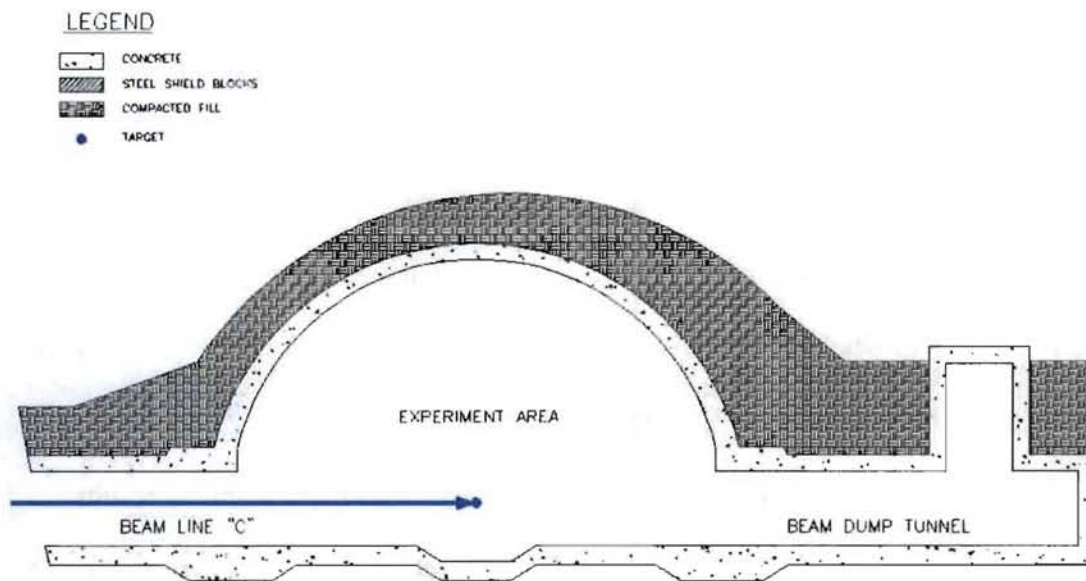
Figure 52: Cross-sectional view of the HRS Dome at LANSCE Area C.
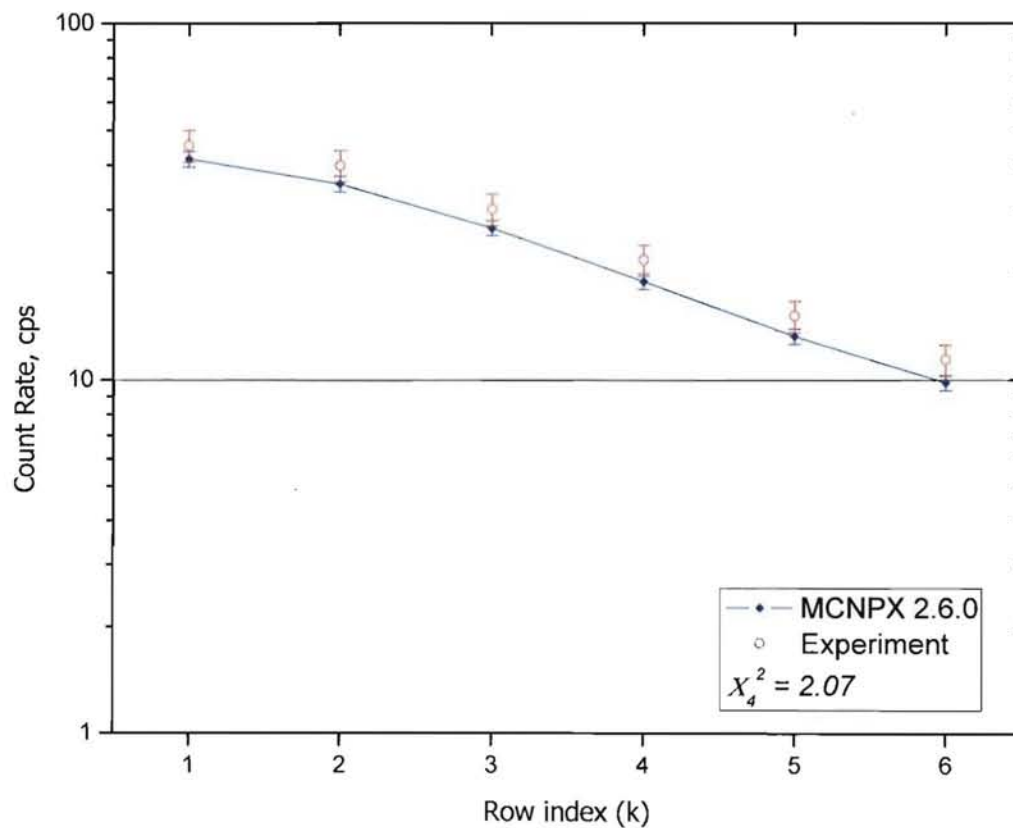
Figure 53: Results of row-sum efficiency measurement with full ANDY array including only the concrete floor in the MCNPX model. The MCNPX data was assigned 5% error bars to account for approximations in the detector and source

models.

Figure 53 was created by summing each row of tubes individually. Only the source, detector, and concrete floor were included in the MCNPX model. The reduced chi-square value of 2.07 shows marginal agreement. Overall, the MCNPX results are 11.6% less than the experimental data. The intrinsic efficiency calculated by MCNPX was 20.2%, 13.0% less than the measured value of 23.2%. These deficiencies are comparable to but slightly greater than those from the results presented in Chapter 3. Conversely, the differences also fall within the expected range of the efficacy suggested in Chapter 2. Consequently, an improved model is required to determine if these results are consistent with the results of Chapter 3. The question, then, is what level of detail needs to be added to the model to obtain sufficient fidelity? In this case the experiment and code are already very close to agreement, so fine details should not be necessary. It should suffice to improve the accuracy of the efficacy measurement by adding rough models of massive scattering objects such as the cylindrical concrete walls and hemispherical dome.
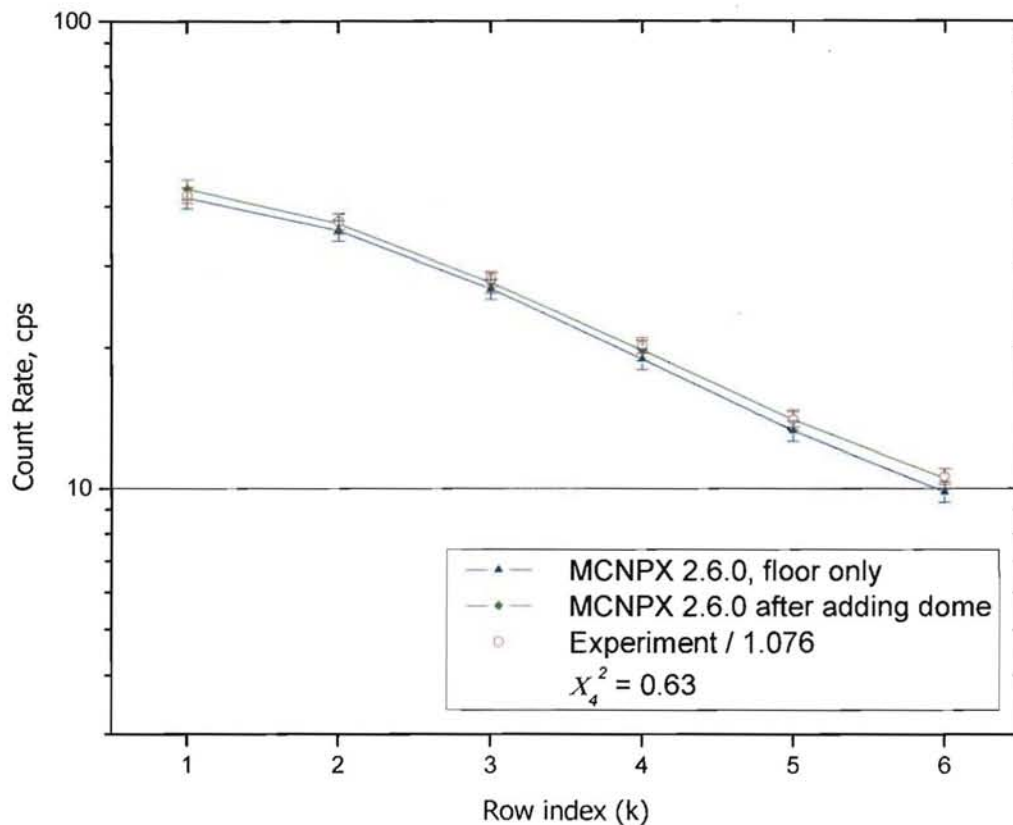
Figure 54: Results of row-sum efficiency measurement with source correction and improved MCNPX model.

In Figure 54 a solid concrete dome structure was added to the MCNPX model.

This model differs from the actual experimental area in that it lacks the wall

penetrations and scattering objects inside the dome. These are considered relatively

minor perturbations compared to the concrete structure itself. The empirical data was

also renormalized using the source activity correction factor 1/1.076 that was

calculated in sections 3.3.3 and 6.1. The new reduced chi-square value of 0.63

suggests much better agreement than the original model. This exercise demonstrates

that failure to properly account for the efficacy in an experimental apparatus can have

profound detrimental effects on the accuracy of computer simulations. The models of

scattering objects and structures need not be elaborate, but they must be present.

Chapter 7 : Conclusion

Computer simulations with the MCNPX code predict an increase in cost efficiency of 2.5-3.5 for neutron detectors based on an array of low-pressure helium-3 drift tubes (ANDY-type detector) over conventional high-pressure tubes. Benchmarking experiments performed with a prototype ANDY detector that was designed and constructed at LANL provide direct validation of these results. The results were consistent enough to suggest a correction factor in the Cf-252 source activity of 7.6%.

The concept of efficacy was introduced as a semi-deterministic method of calculating the effect of neutrons scattering from objects in the environment on detector count rate. A successful series of neutronics-based benchmarking experiments reinforces this concept. The results presented herein provide groundwork for the design of large-area neutron detectors that will be used in Homeland Security applications. More importantly, this work paves the road toward successful management of limited worldwide helium-3 resources for many years to come.

7.1 Additional Work

Several additional studies are underway to extend this work. A few of these are briefly presented below:

7.1.1 Addition of boron lining for further increase in efficiency

The efficiency of low-pressure gaseous neutron detectors can be increased by adding a boron lining. Work is currently underway at LANL to develop this technology in a robust and cost-effective manner. Figure 55 shows an early initial result. The efficiency of this particular helium-3 detector was increased by nearly 20%. Details of the methods being investigated are proprietary.
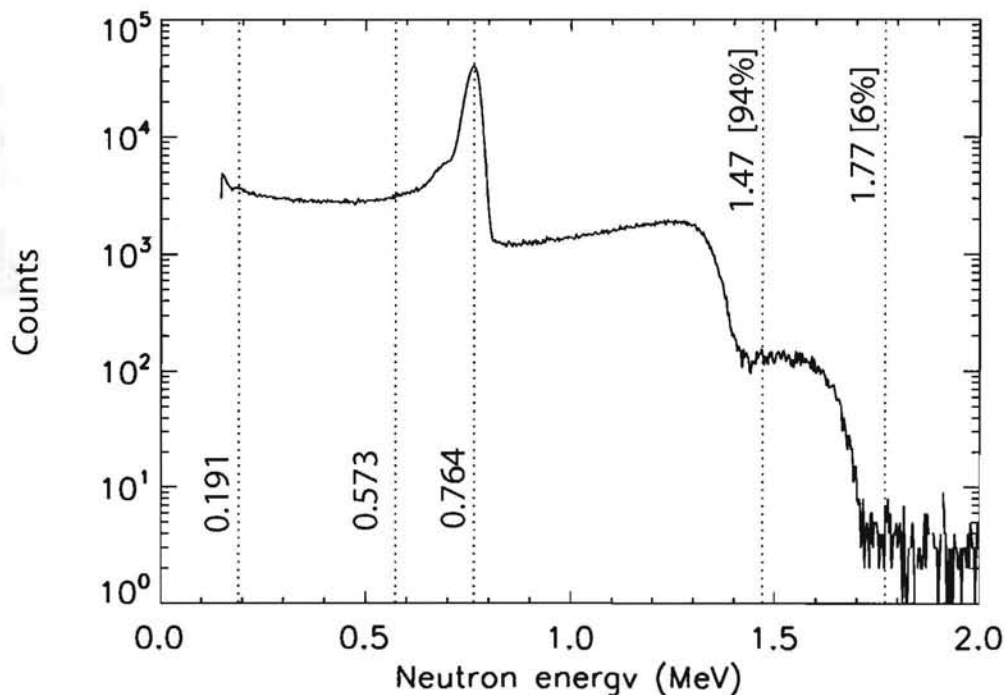
Figure 55: Pulse-height spectrum of a 3He-10B hybrid detector. Key features identifying the daughter particles from both isotopes are clearly distinguishable.

7.1.2 Energy selection via external shielding

The response curve of ANDY-type detectors as a function of neutron energy can be tailored to a desired neutron flux spectrum by adding external neutron moderators and/or absorbers. Figure 56 shows a few examples:
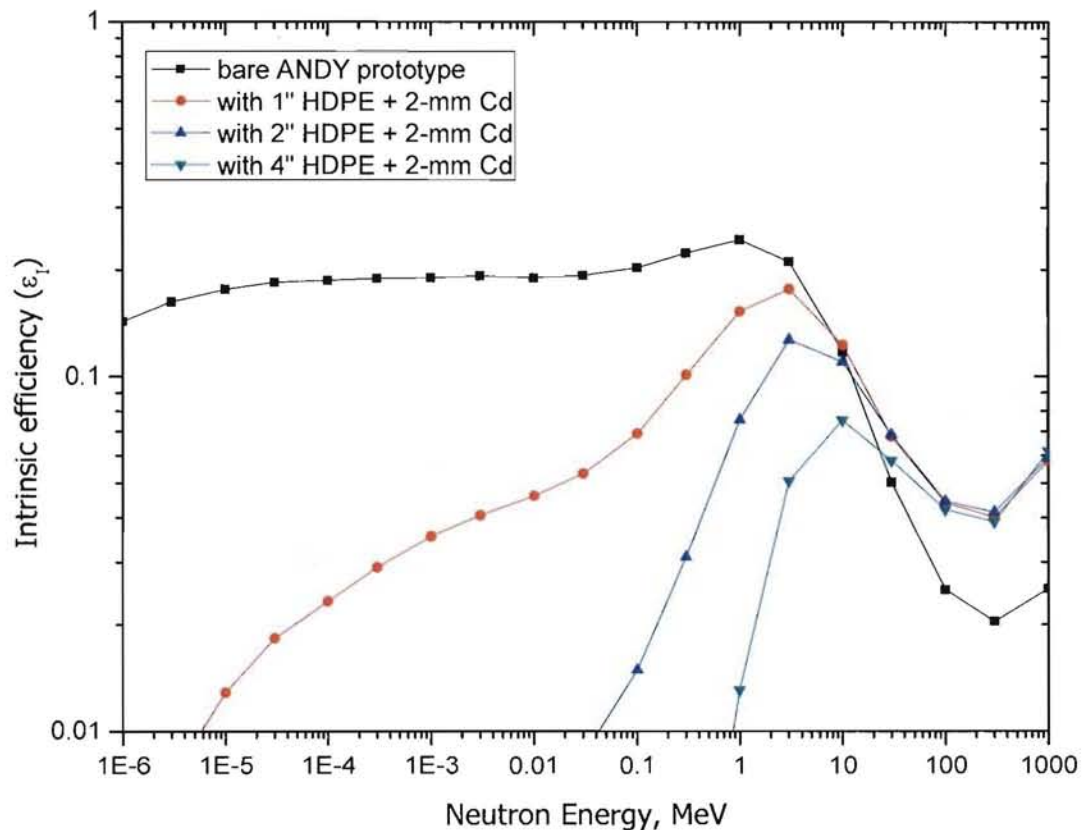
Figure 56: Efficiency curves for the ANDY prototype with several external shielding scenarios simulated with MCNPX. Statistical error bars are < 1%.

7.1.3 External Monitoring for Dosimetry and Experimental Support

The high sensitivity of the ANDY prototype detector also makes it very useful

for external monitoring applications. These can include dose measurements taken

outside primary shielding walls as demonstrated in Figures 57-59 or as a sanity check

to verify that beam was delivered, to name just a few.

Figure 57: The ANDY Prototype in operation outside the primary shielding door at Area C at LANSCE (HRS dome).
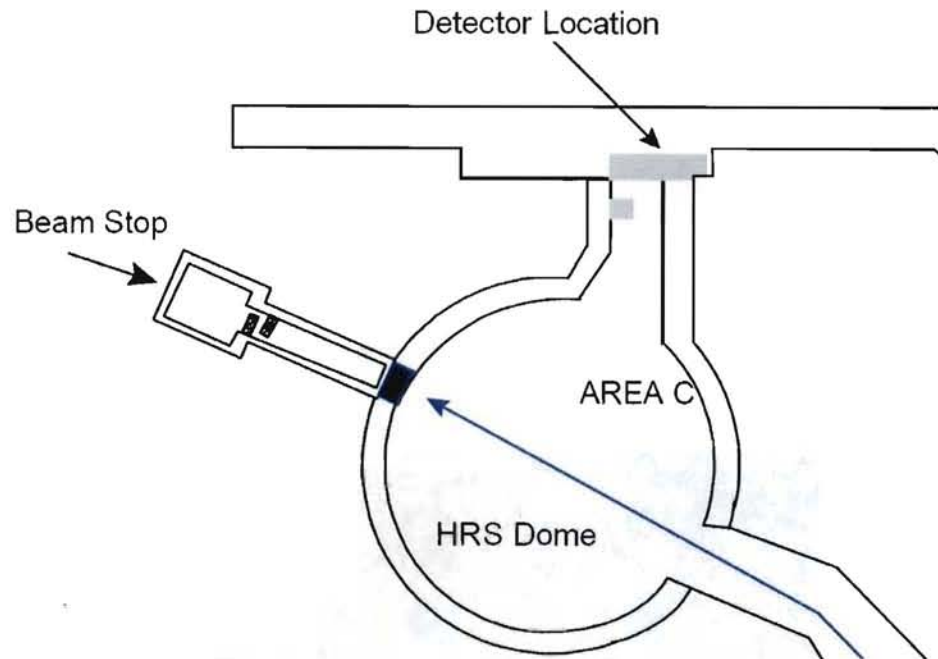
Figure 58: Plan view of the HRS dome. The blue line shows the path of the proton beam.
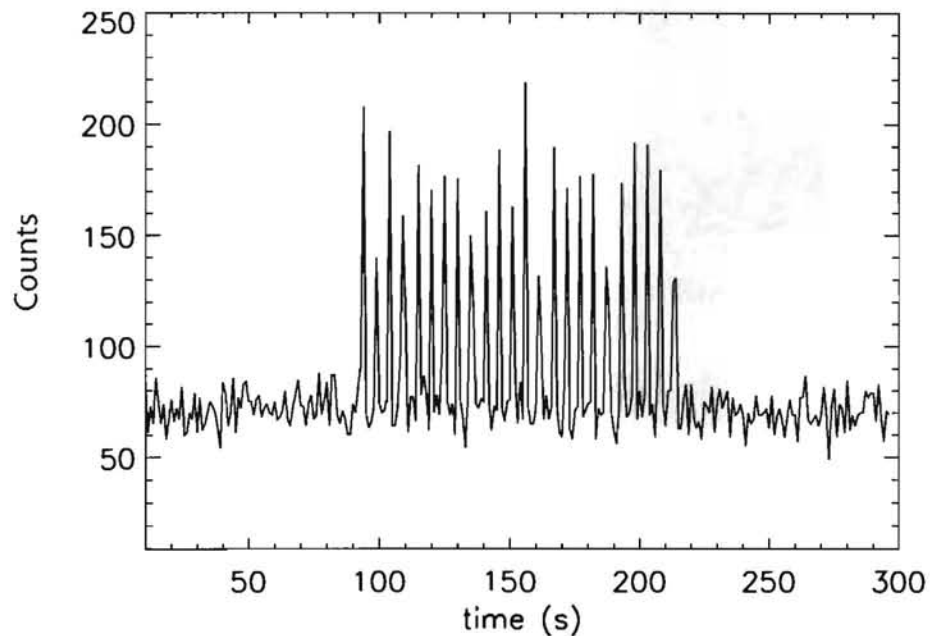
Figure 59: Time response of ANDY prototype during proton beam tuning.

References

1. J.M. Cork, Radioactivity and Nuclear Physics, D. Van Nostrand Co. Inc, New York, 1947.

2. J. Chadwick and M. Goldhaber, "A 'Nuclear Photo-effect': Disintegration of the Diplon by g-Rays", Nature 134, pg 237, 1934.

3. D. B. Pelowitz, editor, MCNPX User's Manual, Version 2.6.0, Los Alamos National Laboratory, LA-CP-07-1473, 2008.

4. W.J. Price, Nuclear Radiation Detection, 2nd Ed., McGraw-Hill Book Company, New York, 1964.

5. ASTM E 721-94, 1998. "Standard guide for determining neutron energy spectra . . .", 1998 Annual Book of ASTM Standards, Vol. 12.02, ASTM, West Conshohocken, PA, pp. 280-290.

6. Wheeler FJ, Nigg DW, Capala J, Watkins PR, Vroegindeweij C, Auterinen I, Seppälä T, Bleuel D, "Boron neutron capture therapy (BNCT): implications of neutron beam and boron compound characteristics", Medical Physics, Vol. 26 No. 7, pp 1237-44 (1999).

7. J. F. Briesmeister, Editor, X-5 Division, LANL, MCNP-A General Monte Carlo N-Particle Transport Code, Version 4C, RSICC, Oak Ridge National Laboratory, 2000.

8. A. Foderaro, The Elements of Neutron Interaction Theory, The MIT Press, Cambridge, Massachusetts and London, England, 1971.

9. C.E. Wiegand, et al, "Detection Efficiency of Plastic Scintillator for Neutron Energies 4 to 76 MeV", Rev. Sci. Instr., 33 No. 5, pg 526, 1962.

10. P.L. Reeder, "Detection of fast neutrons in a plastic scintillator using digital pulse processing to reject gammas", Nuclear Instruments and Methods-A 422 No 1-3, pp 84-88, 1999.

11. L.M. Bollinger and G.E. Thomas, "Neutron Detection with Glass Scintillators", Nucl. Instr. and Methods 17, pp 97-116, 1962.

12. G.E. Thomas, "A boron-loaded liquid scintillation neutron detector using a single photomultiplier", Nucl. Instr. and Methods 17, pp 137-139, 1962.

13. http://www.nndc.bnl.gov/exfor/endf00.htm; "Evaluated Nuclear Data File", National Nuclear Data Center, Brookhaven National Laboratory, New York.

14.   See http://ie.lbl.gov/ngdata/sig.txt for a convenient list; "Neutron Cross Sections . . .", S.F Mughabghab, M. Divadeenam and N.E. Holden, Academic Press, 1981.

15.   Z. Wang, et al, "Inexpensive and practical sealed drift-tube neutron detector", submitted to Nuclear Instruments and Methods-A, Feb 2009.

16.   R.B Firestone, Coral M. Baglin, and S.Y Frank Chu, Table of Isotopes, 8th Ed., John Wiley & Sons, New York, NY, 1999.

17.   A.J Stokes, T.J. Meal, J.E. Myers, Jr, "Improved performance of BF3 neutron counters in high gamma fluxes", IEEE Transactions on Nuclear Science, 13, pp 630-635, 1966.

18.   MCNPX simulation of proton interrogation experiments conducted at LANSCE. Calculations performed by LANL MCNPX applications team, D-5 group, 2008 (unpublished).

19.   S.Y.F. Chu, L.P. Ekstrom, R.B. Firestone, The Lund/LBNL WWW Table of Radioactive Isotopes, http://nucleardata.nuclear.lu.se/NuclearData/toi/

20.   F.-J. Hambsch, A. Tudora, G. Vladuca, S. Oberstedt, "Calculation of Prompt Neutron Multiplicities and Spectra for Several Nuclides", International Conference on Nuclear Data for Science and Technology, AIP CP 769, pp 362-365, May 24 2005.

21.   A.S. Vorobyev, V.N. Dushin, F.-J. Hambsch, V.A. Jakovlev, V.A. Kalinin, A.B. Laptev, B.F. Petrov, and O.A. Shcherbakov, "Distribution of Prompt Neutron Emission Probability for Fission Fragments in Spontaneous Fission of 252Cf and 244, 248Cm", International Conference on Nuclear Data for Science and Technology, AIP CP 769, pp 613-616, May 24 2005.

22.   R. C. Martin, J. B. Knauer, and P. A. Balo, "Production, Distribution, and Applications of Californium-252 Neutron Sources", presented at 4th Topical Meeting on Industrial Radiation and Radioisotope Measurement Applications (IRRMA '99), Raleigh, North Carolina, Oct. 3-7, 1999.

23.   "Properties of Neutron Sources", Proceedings of an Advisory Group Meeting on Properties of Neutron Sources Organized by the International Atomic Energy Agency, June 9-13 1986, Leningrad, USSR, p.10, International Atomic Energy Agency, Vienna, 1986.

24.   Proceedings of IAEA Panel Neutron Standard Reference Data, Vienna, Austria, Nov. 20-24 1972, CONF-721127, p. 362, International Atomic

Energy Agency, Vienna, 1973.

25.   Proceedings of IAEA Consultants' Meeting on Prompt Fission Neutron
       Spectra, Vienna, Austria, Aug. 25-27 1971, p. 169, International Atomic
       Energy Agency, Vienna, 1979.

26.   Definition at http://www.merriam-webster.com/dictionary/efficacy, retrieved
       May 12, 2009.

27.   Anatoly V. Zrodnikov, Victor Ya. Poupko, and George M. Gryaznov,
       "Experimental Detection of Neutron Gas Pressure on the Control Rods of a
       Nuclear Reactor under the Microgravity Conditions", AIP Conf. Proc. 301,
       625, 1994.

28.   J. Kammeraad et al., "Radiological and Nuclear Countermeasures",
       Department of Homeland Security, Briefing, 9 March 2004

29.   D. Srikrishna, A. N. Chari and T. Tisch, "Deterrence of Nuclear Terrorism
       with Mobile Radiation Detectors", *Nonproliferation Review*, 12.3, pp. 573-
       614, 2005.

30.   J. Medalia, "Nuclear Terrorism: A Brief Review of Threats and Responses",
       CRS Report for Congress RL32595, The Library of Congress, 2004.

31.   A. Glaser, "Detection of Special Nuclear Materials",
       http://www.princeton.edu/~aglaser/lecture2007_detection.pdf

32.   S.J. Greene, "Delayed Neutron Emission Induced by 800 MeV Protons",
       http://p25ext.lanl.gov/~hubert/activei/files/AIWorkshop07.ppt, 2007.

33.   J.L Jones, et al, "Proof-of-Concept Assessment of a Photofission-Based
       Interrogation System for the Detection of Shielded Nuclear Material", INEEL
       Report INEEL/EXT-2000-01523, 2000.

34.   M.T. Kinlaw, A.W. Hunt, "Fissionable isotope identification using the time
       dependence of delayed neutron emission", Nuclear Instruments and Methods
       in Physics Research-A 562, pp1081-1084, 2006.

35.   J. Medalia, "Terrorist Nuclear Attacks on Seaports: Threat and Response",
       CRS Report for Congress RS21293, The Library of Congress, 2005.

36.   U.S. Department of Homeland Security, Bureau of Customs and Border
       Protection, "Remarks by Commissioner Robert C. Bonner, Council on
       Foreign Relations, New York, New York,", January 11, 2005.

37.   G. Peter Nanos, Jr., "CWMD Research & Development Overview", briefing

delivered at 2008 Unrestricted Warfare Conference, March 10, 2008.

38.   H. Daniel, "Application of muonic X-rays for elemental analysis", Biological trace Element Research, Vol. 13 No. 1 pp 301-318, 2007.

39.   L.J. Wittenberg, "Non-Lunar He-3 Resources", presented at the second Wisconsin Symposium on helium-3 and Fusion Power, Madison Wi, July 1993.

40.   L.J. Wittenberg, et al, "A Review of helium-3 resources and acquisition for use as a fusion fuel", Fusion Technology, Special Issue on D-He3 Fusion, Vol. 21 No. 4, pp 2230-2253, 1991.

41.   J. Bonde & A. Tortorello, "Helium-3: The energy source of tomorrow?", http://web.mit.edu/22.012/www/presentations/Helium-3%20version%202.ppt

42.   LND Inc. product listing, http://www.lndinc.com/products/category/22/

43.   J.R. Taylor, An Introduction to Error Analysis, University Science Books, California, 1997.

44.   P.R. Bevington, D.K. Robinson, Data Reduction and Error Analysis for the Physical Sciences, 3rd Ed., McGraw-Hill, New York, 2002.

45.   K. Borozdin et al., "Radiographic Imaging with Cosmic Ray Muons", Nature, 422, p.277, 2003.

46.   J. A. Green, C. Alexander, T. Asaki, J. Bacon, G. Blanpied, K. Borozdin, et al., "Optimizing the Tracking Efficiency for Cosmic Ray Muon Tomography", 2006 IEEE Nuclear Science Symposium Conference Record, San Diego, CA 286-288, 2006.

47.   C. L. Morris, C. C. Alexander, J. D. Bacon, K. N. Borozdin, et al., "Tomographic Imaging with Cosmic Ray Muons", Science & Global Security, Vol. 16 No. 1&2, pp 37-53, 2008.

Appendix A: Sample MCNPX input file

An MCNP/MCNPX input file is referred to as a "deck" and each line in the file is called a "card." These terms reflect the historic nature of the codes, hearkening back to the days when actual stacks of punch cards were used to load a program into the computer. The following input deck represents a model of the ANDY prototype detector located inside a greatly simplified model of the HRS dome at LANSCE. The results from this deck were used to produce the green curve, "row-sum efficiency measurement with improved MCNPX model," in Figure 54 on 103.

A.1: Listing of MCNPX input file rbr02.i

```
rbr02.i: Measuring row-by-row neutron efficiency
C
C ******************************** Comments *********************************
C
C Modeling 10/17/2008 experiment
C ANDY prototype in dome
C
C
C ******************************** Cell Cards *******************************
C
C .................................................... Area C dome
C
100     5    -2.3          -101 100                     $        circular wall
101     5    -2.3          -102 101                     $        circular wall
110     5    -2.3          -111 110 +100.2              $               dome
111     5    -2.3          -112 111 +100.2              $               dome
C
C ......................................... Primary Detector Structures
601    13    -2.7          -601 602 604                 $        Al Faraday Cage
603  2201  -9.264E-04      -603 611 612 613 614 615 616 750  $     Interior Air
604  2201  -9.264E-04      -604 741 721 731             $             Top Air
605  2201  -9.264E-04      -605                         $            Lower Air
C
611  2201  -9.264E-04      -611 751                     $        Big EC Cell 000
612  2201  -9.264E-04      -612 #752                    $        Big EC Cell 100
613  2201  -9.264E-04      -613 #753                    $        Big EC Cell 200
614  2201  -9.264E-04      -614 #754                    $        Big EC Cell 001
615  2201  -9.264E-04      -615 #755                    $        Big EC Cell 101
616  2201  -9.264E-04      -616 #756                    $        Big EC Cell 201
C
C .............................. Outer Box Front Polyethylene
701  3221  -0.95           -701 702 703                 $ Front poly modratr
702  2201  -9.264E-04      -702 750                     $              Groove
703  2201  -9.264E-04      -703 750                     $              Groove
C
C .............................. Outer Box Back Polyethylene
711  3221  -0.95           -711 712 713 714             $  Back poly modratr
712  2201  -9.264E-04      -712 750                     $              Groove
713  2201  -9.264E-04      -713 750                     $              Groove
714  2201  -9.264E-04      -714                         $                Step
C
C .............................. Outer Box Side Polyethylene
721  3221  -0.95           -721 722 741 742             $ RSide poly modratr
722  2201  -9.264E-04      -722                         $              Groove
731  3221  -0.95           -731 732 741 742             $ LSide poly modratr
732  2201  -9.264E-04      -732                         $              Groove
C
C .............................. Outer Box Top, Base, and Lower Base
```

```
741  3221  -0.95         -741 831 832 833 834 835 836    $           Top
742  3221  -0.95         -742 781 782 783 784 785 786    $           Base
743  3221  -0.95         -743                            $           Lower Base
C
C ..................................................... Large Egg Crate
C This definition has a glitch where the crate slides into the slots
C in the front and rear panels.  Its negligible.
750  3221  -0.95         -750 611 612 613 614 615 616
                         (701:-702:-703) (711:-712:-713)
751  2201  -9.264E-04    -751              fill=761
752  2201  -9.264E-04    -752              fill=762
753  2201  -9.264E-04    -753              fill=763
754  2201  -9.264E-04    -754              fill=764
755  2201  -9.264E-04    -755              fill=765
756  2201  -9.264E-04    -756              fill=766
C
761  2201  -9.264E-04    -761     trcl=761 lat=1 u=761
            fill=0:3 0:0 0:2      1  3r          1  3r        1  3r
C
762  like 761 but                 trcl=762 lat=1 u=762
            fill=0:3 0:0 0:2      1  3r          1  3r        1  3r
C
763  like 761 but                 trcl=763 lat=1 u=763
            fill=0:3 0:0 0:2      1  3r          1  3r        1  3r
C
764  like 761 but                 trcl=764 lat=1 u=764
            fill=0:3 0:0 0:2      1  3r          1  3r        1  3r
C
765  like 761 but                 trcl=765 lat=1 u=765
            fill=0:3 0:0 0:2      1  3r          1  3r        1  3r
C
766  like 761 but                 trcl=766 lat=1 u=766
            fill=0:3 0:0 0:2      1  3r          1  3r        1  3r
C
C ..................................................... Source and stand
C
771  1028  -0.22         -771
772    13  -2.7          -772
773  3221  -0.90         -773
C
C ..................................................... Holes in base
779  3221  -0.95         780                            u=3 $       HDPE
780  2201  -9.264E-04    -780                           u=3 $       Hole
781  3221  -0.95         -781              fill=781
782  3221  -0.95         -782              fill=782
783  3221  -0.95         -783              fill=783
784  3221  -0.95         -784              fill=784
785  3221  -0.95         -785              fill=785
786  3221  -0.95         -786              fill=786
C
791  3221  -0.95         -791     trcl=791 lat=1 u=781 fill=3
792  like 791 but                 trcl=792 lat=1 u=782
793  like 791 but                 trcl=793 lat=1 u=783
794  like 791 but                 trcl=794 lat=1 u=784
795  like 791 but                 trcl=795 lat=1 u=785
796  like 791 but                 trcl=796 lat=1 u=786
C
C ..................................................... Neutron Detectors
C
800  2201  -9.264E-04     801 805 806                   u=1 $       Outside Air
801    13  -2.7          -801 802                        u=1 $       Detector Outer
802  2344  -1.974E-03    -802 803                        u=1 $       Detector Gas
803  2344  -1.974E-03    -803 804                        u=1 $       Detector Gas
804  2201  -9.264E-04    -804                            u=1 $       Anode Wire
805  3221  -0.95         -805                            u=1 $       Side wall
806  3221  -0.95         -806                            u=1 $       Back wall
C
810  2201  -9.264E-04     805 806                        u=2 $       Empty Cell Air
815  3221  -0.95         -805                            u=2 $ EmptyCel Side wall
816  3221  -0.95         -806                            u=2 $ EmptyCel Back wall
```

```
C
C ...................................................... Top holes
C
827   3221   -0.95          828 829                     u=4 $          Top HDPE
828   2201   -9.264E-04    -828 829                     u=4 $          Top hole
829   2201   -9.264E-04    -829                         u=4 $          Top cone
831   3221   -0.95         -831          fill=841
832   3221   -0.95         -832          fill=842
833   3221   -0.95         -833          fill=843
834   3221   -0.95         -834          fill=844
835   3221   -0.95         -835          fill=845
836   3221   -0.95         -836          fill=846
841   3221   -0.95         -841   trcl=841 lat=1 u=841 fill=4 $    Top Hole univ
842   like 841 but                trcl=842 lat=1 u=842        $    Top Hole univ
843   like 841 but                trcl=843 lat=1 u=843        $    Top Hole univ
844   like 841 but                trcl=844 lat=1 u=844        $    Top Hole univ
845   like 841 but                trcl=845 lat=1 u=845        $    Top Hole univ
846   like 841 but                trcl=846 lat=1 u=846        $    Top Hole univ
C
C ...................................................... Air & Universe
C
982    5    -2.3           -982                          $          Concrete floor
983    5    -2.3           -983 982                      $          Concrete floor
984    5    -2.3           -984 983                      $          Concrete floor
985    5    -2.3           -985 984                      $          Concrete floor
986    5    -2.3           -986 985                      $          Concrete floor
987    5    -2.3           -987 986                      $          Concrete floor
988    5    -2.3           -988 987                      $          Concrete floor
989    5    -2.3           -989 988                      $          Concrete floor
990    5    -2.3           -990 989                      $          Concrete floor
998   2201  -9.264E-04   -999 601 990 772 771 773 #100 #110 #101 #111
999    0                   999


C ***************************** Surface Cards ******************************
C
C .......................................................................
C Area C dome
C
100        rcc   0    0    900    0    450    0    1400        $    circular wall
101        rcc   0    0    900    0    450    0    1405        $    circular wall
102        rcc   0    0    900    0    450    0    1700        $    circular wall
110         s    0   250   900                   1422.146     $     dome inner
111         s    0   250   900                   1427         $     dome outer
112         s    0   250   900                   1700         $     dome outer
C
C .......................................................................
C Primary Detector Structures
C                                                             $    Faraday Outer
0601  01  rpp  -0.079375   75.618975  -0.079375  138.179175  -0.079375
          46.104175
0602  01  rpp  0   75.5396   0   133.985   0   46.0248        $      Outer Box
0603  01  rpp  2.54  72.9996  9.525  131.445  2.54  40.9448   $      Interior
0604  01  rpp  0  75.5396  131.445  138.0998  0  46.0248      $      Upper Air
0605  01  rpp  2.54  72.9996  2.54  6.985  2.54  40.9448      $      Lower Air
0611  01  rpp  2.54  25.2857  9.525  131.445  2.54  21.1074   $    EC1 Cell 000
0612  01  rpp  26.5557  48.9839  9.525  131.445  2.54  21.1074$    EC1 Cell 100
0613  01  rpp  50.2539  72.9996  9.525  131.445  2.54  21.1074$    EC1 Cell 200
0614  01  rpp  2.54  25.2857  9.525  131.445  22.3774  40.9448$    EC1 Cell 001
C                                                             $    EC1 Cell 101
0615  01  rpp  26.5557  48.9839  9.525  131.445  22.3774  40.9448
C                                                             $    EC1 Cell 201
0616  01  rpp  50.2539  72.9996  9.525  131.445  22.3774  40.9448
C
C .......................................................................
C Outer Box Front Polyethylene
0701  01  rpp  0   75.5396   0   131.445   0   2.54           $       OB Front
0702  01  rpp  25.273  26.5684  9.525  131.445  2.1336  2.54  $      OBF Grv 1
0703  01  rpp  48.9712  50.2666  9.525  131.445  2.1336  2.54 $      OBF Grv 2
C
C .......................................................................
```

```
C Outer Box Back Polyethylene
0711  01  rpp  0  75.5396  0  131.445  40.9448  46.0248        $        OB Back
C                                                               $        OBBk Grv 1
0712  01  rpp  25.273  26.5684  9.525  131.445  40.9448  41.3512
C                                                               $        OBBk Grv 2
0713  01  rpp  48.9712  50.2666  9.525  131.445  40.9448  41.3512
0714  01  rpp  0  75.5396  0  9.525  43.4848  46.0248           $        OBBk Step
C
C ...............................................................
C Outer Box Side Polyethylene
0721  01  rpp  0  2.54  0  133.985  2.54  40.9448               $        OB R Side
0722  01  rpp  2.2098  2.54  9.525  131.445  21.082  22.4028    $        OBRS Grv
0731  01  rpp  72.9996  75.5396  0  133.985  2.54  40.9448      $        OB L Side
C                                                               $        OBLS Grv
0732  01  rpp  72.9996  73.3298  9.525  131.445  21.082  22.4028
C
C ...............................................................
C Outer Box Top, Base, and Lower Base
0741  01  rpp  1.905  73.6346  131.445  133.985  0  43.4848     $        OB Top
0742  01  rpp  1.905  73.6346  6.985  9.525  2.54  40.9448      $        OB Base
0743  01  rpp  2.54  72.9996  0  2.54  2.54  40.9448            $     OB Lowerbase
C
C ...............................................................
C Large Egg Crate
0750  01  rpp  2.8448  72.6948  9.525  131.445  2.2098  41.275$  Lg Egg Crate
C                                                               $     EC2 Univ 000
0751  01  rpp  2.8576  25.2856  9.5251  131.4449  3.1751  21.1073
C                                                               $     EC2 Univ 100
0752  01  rpp  26.5558  48.9838  9.5251  131.4449  3.1751  21.1073
C                                                               $     EC2 Univ 200
0753  01  rpp  50.254  72.682  9.5251  131.4449  3.1751  21.1073
C                                                               $     EC2 Univ 001
0754  01  rpp  2.8576  25.2856  9.5251  131.4449  22.3775  40.3097
C                                                               $     EC2 Univ 101
0755  01  rpp  26.5558  48.9838  9.5251  131.4449  22.3775  40.3097
C                                                               $     EC2 Univ 201
0756  01  rpp  50.254  72.682  9.5251  131.4449  22.3775  40.3097
0761  01  rpp  -2.5654  3.2004  0  121.92  -2.5654  3.8354      $  EC2-000 UnitCl
C
C ...............................................................
C Source
C                                                               $        foam block
0771      rpp  22.7698  52.7698  75.565  80.645  -108  -92
C                                                               $        Cf-252 source
0772      rcc  37.7698  80.645  -99        0  2.54  0  0.4
C                                                               $        ladder top
0773      rpp  22.7698  52.7698  74.565  75.565  -108  -92
C
C ...............................................................
C Holes in base
0780  01  rcc  6.29412  6.985  6.61162  0  2.54  0  2.032       $        Hole 000
0781  01  rpp  2.8575  25.9207  6.985  9.525  3.175  21.717     $     HoleUniv 000
0782  01  rpp  26.5557  49.6189  6.985  9.525  3.175  21.717    $     HoleUniv 100
0783  01  rpp  50.2539  73.3171  6.985  9.525  3.175  21.717    $     HoleUniv 200
0784  01  rpp  2.8575  25.9207  6.985  9.525  21.7678  39.6748$  HoleUniv 001
C                                                               $     HoleUniv 101
0785  01  rpp  26.5557  49.6189  6.985  9.525  21.7678  39.6748
C                                                               $     HoleUniv 201
0786  01  rpp  50.2539  73.3171  6.985  9.525  21.7678  39.6748
0791  01  rpp  2.8575  8.6233  6.985  9.525  3.175  9.5758      $        Hole Univ
C
C ...............................................................
C Neutron Detectors
0801  01  rcc  0  -1  0  0  122.92  0  2.54                     $        Det outer
0802  01  rcc  0  0.0254  0     0  121.8692  0  2.5146          $        Det inner
0803  01  rcc  0  0.025654  0  0  121.868692  0  2.514346       $        Boron layer
0804  01  rcc  0  0.025654  0  0  121.868692  0  0.00635        $        Anode wire
0805  01  rpp  2.5654  4.2004  -1  122.92  -3.5654  4.8354      $        Side poly
0806  01  rpp  -3.5654  2.5654  -1  122.92  2.5654  4.8354      $        Back poly
C
```

```
C ...........................................................................
C Holes in Top
0828  01  rcc  0   131.4449   0   0   2.5402   0   0.9525        $          Top hole
0829  01  k/y  0   133.35   0   1   -1                           $       Top cntrsnk
C                                                                 $ Top Hole UnitCl
0841  01  rpp  -2.5654   3.2004   131.4449   133.9851   -2.5654   3.8354
C                                                                 $TopHole Univ 000
0831  01  rpp  2.8576   25.2856   131.445   133.985   3.1751   21.1073
C                                                                 $TopHole Univ 100
0832  01  rpp  26.5558   48.9838   131.445   133.985   3.175   21.1074
C                                                                 $TopHole Univ 200
0833  01  rpp  50.254   72.682   131.445   133.985   3.1751   21.1073
C                                                                 $TopHole Univ 001
0834  01  rpp  2.8576   25.2856   131.445   133.985   22.3775   40.3097
C                                                                 $TopHole Univ 101
0835  01  rpp  26.5558   48.9838   131.445   133.985   22.3775   40.3097
C                                                                 $TopHole Univ 201
0836  01  rpp  50.254   72.682   131.445   133.985   22.3775   40.3097
C
C ...........................................................................
C Air & Universe
0982      rpp  -2999   2999   -1   0   -2999   2999               $          Floor
0983      rpp  -2999   2999   -2   0   -2999   2999               $          Floor
0984      rpp  -2999   2999   -3   0   -2999   2999               $          Floor
0985      rpp  -2999   2999   -4   0   -2999   2999               $          Floor
0986      rpp  -2999   2999   -5   0   -2999   2999               $          Floor
0987      rpp  -2999   2999   -6   0   -2999   2999               $          Floor
0988      rpp  -2999   2999   -7   0   -2999   2999               $          Floor
0989      rpp  -2999   2999   -8   0   -2999   2999               $          Floor
0990      rpp  -2999   2999   -199   0   -2999   2999             $          Floor
0999      rpp  -3000   3000   -200 2800   -3000   3000           $      world bndry
C
C ****************************** Transformations ****************************
C
C                                                                5-1/4" above floor
tr01    0      13.335      0                                     $   Detector origin
C
tr761   5.422900000    9.5250    5.740400000            $   EC2-000 univ origin
tr762   29.12110000    9.5250    5.740400000            $   EC2-100 univ origin
tr763   52.81930000    9.5250    5.740400000            $   EC2-200 univ origin
tr764   5.422900000    9.5250    24.94280000            $   EC2-001 univ origin
tr765   29.12110000    9.5250    24.94280000            $   EC2-101 univ origin
tr766   52.81930000    9.5250    24.94280000            $   EC2-201 univ origin
C
tr791   0              0         0                      $   Base Hole-000 origin
tr792   23.6982        0         0                      $   Base Hole-100 origin
tr793   47.3964        0         0                      $   Base Hole-200 origin
tr794   0              0         17.45996               $   Base Hole-001 origin
tr795   23.6982        0         17.45996               $   Base Hole-101 origin
tr796   47.3964        0         17.45996               $   Base Hole-201 origin
C
tr841   5.422900000    0         5.740400000            $   EC2-000 univ origin
tr842   29.12110000    0         5.740400000            $   EC2-100 univ origin
tr843   52.81930000    0         5.740400000            $   EC2-200 univ origin
tr844   5.422900000    0         24.94280000            $   EC2-001 univ origin
tr845   29.12110000    0         24.94280000            $   EC2-101 univ origin
tr846   52.81930000    0         24.94280000            $   EC2-201 univ origin
C
C ****************************** Material Cards ****************************
C
read file lanl_gas.trf
read file air_2201_lineC.trf
read file poly_3221.trf
read file concrete_lanl_m5.trf
read file 304.trf
C
C -=-=-=-=-=-=-=-=-=-=-=-=-=-=-=-=-=-=-=-=-=-=-=-=-=-=-=- Aluminum, p = 2.7
m13     13027 1
C                                                     Polyurethane Foam p = 0.12
m1028   6012  25      1001  42      7014  2      8016  6
```

```
C                                                    Polystyrene  p = 1.060
m3226     1001      -7.7418     6000     -92.2582
C
C
C *************************** Variance Reduction ***************************
C
imp:n 0.5 0.2 0.5 0.2 1  80r .5m .5m .5m .5m .5m .5m .5m  1 0
C
C ******************************* Source Cards ***************************
C
C Cf-252 area sources, 12 tube positions, vertical thirds
C
sdef    par=1
        erg=d1
        cel 772
        pos 37.7698  80.645  -99
        rad=d4
        ext=d5
        axs=0 1 0
C
si4 0 0.2
sp4 -21 1
C
si5 0.2 0.8
sp5   0   1
C
read file cf252_unbiased.trf
C
C ******************************** Tallies ********************************
C
  FC1 Current crossing the outer faces
   F1:n 602.1 602.2 602.5 602.6
   C1 0 1
   T1 0  36i  37e8
  FQ1 T F C
C
FC104    Flux-integrated He3 signal, rows and total
  F104:n
       (803<(761[0:3 0:0 0:0] 762[0:3 0:0 0:0]  763[0:3 0:0 0:0])<(751 752 753))
       (803<(761[0:3 0:0 1:1] 762[0:3 0:0 1:1]  763[0:3 0:0 1:1])<(751 752 753))
       (803<(761[0:3 0:0 2:2] 762[0:3 0:0 2:2]  763[0:3 0:0 2:2])<(751 752 753))
       (803<(764[0:3 0:0 0:0] 765[0:3 0:0 0:0]  766[0:3 0:0 0:0])<(754 755 756))
       (803<(764[0:3 0:0 1:1] 765[0:3 0:0 1:1]  766[0:3 0:0 1:1])<(754 755 756))
       (803<(764[0:3 0:0 2:2] 765[0:3 0:0 2:2]  766[0:3 0:0 2:2])<(754 755 756))
       T
FM104  4.8806E-06 2339 103
SD104          1  6r                       $   Unity normalization for efficiency
FQ104   T F E
C
FC114    Flux-integrated He3 signal
  F114:n (803 < 761[0:3 0:0 0:0] < 751)
         (803 < 762[0:3 0:0 0:0] < 752)
         (803 < 763[0:3 0:0 0:0] < 753)
         (803 < 761[0:3 0:0 1:1] < 751)
         (803 < 762[0:3 0:0 1:1] < 752)
         (803 < 763[0:3 0:0 1:1] < 753)
         (803 < 761[0:3 0:0 2:2] < 751)
         (803 < 762[0:3 0:0 2:2] < 752)
         (803 < 763[0:3 0:0 2:2] < 753)
         (803 < 764[0:3 0:0 0:0] < 754)
         (803 < 765[0:3 0:0 0:0] < 755)
         (803 < 766[0:3 0:0 0:0] < 756)
         (803 < 764[0:3 0:0 1:1] < 754)
         (803 < 765[0:3 0:0 1:1] < 755)
         (803 < 766[0:3 0:0 1:1] < 756)
         (803 < 764[0:3 0:0 2:2] < 754)
         (803 < 765[0:3 0:0 2:2] < 755)
         (803 < 766[0:3 0:0 2:2] < 756)
FM114  4.8806E-06 2339 103
SD114          1 71r                       $   Unity normalization for efficiency
```

```
FQ114   T F E
C
C ****************************** Other Data Cards ******************************
C
mode n e h t s p a #
phys:n 6j 2                                        $ full-analog mode
LCA 9j 1                                           $        pure LAQGSM
C
c dbcn j j 1 200 1
print -98 -100 -85 -86                            $ eliminates normally unneeded tables
C
prdmp j 2e5  1 2   2e5                             $ write MCTAL, save 2 dumps
C
C ****************************** Problem Cutoffs ******************************
C
C Energy, time cutoffs by particle
cut:n 2j 0 0                                       $ full-analog mode
cut:h j 1e-3
cut:t j 1e-3
cut:s j 1e-3
cut:e j 1e-3
cut:a j 0 $ 1e-3
cut:# j 0 $ 1e-3
C
nps 2e7                               $            source particle cutoff
```

A.2 Supplemental readfiles used in rbr02.i

In order to maintain consistency between different MCNPX decks,

commonly-used cards such as material definitions and source energy spectra are

stored in external files. These files are read into the code via the "read file" card.

This author prefers the file extension ".trf" to uniquely identify this type of file on the

Windows platform. TRF is an acronym for Text Read File.

lanl_gas.trf

```
C ... Begin lanl_gas.trf ...........................................
C
C Gas mixes based on LANL standard proportional gases
C DSC Naked gas (D) is composed of **.*% He4, **.*% C2H6, **.*% CF4, **.*% Ar
C *DSC Naked gas mix is protected by CRADA agreement
C Makela gas (M) is composed of 7.7% C2H6, 43.6% CF4, 48.7% Ar
C The BaseGas column refers to the base gas used and its pressure in mbar
C
C  mat   BaseGas   He-3 pp      g/cc      He3/b*cm
C m2340   M1000   5.000E-02   2.443E-03   1.2202E-06
C m2341   M1000   1.000E-01   2.449E-03   2.4403E-06
C m2342   M1000   3.000E-01   2.474E-03   7.3209E-06
C m2343   M1000   2.500E-02   2.440E-03   6.1008E-07
C m2344   D0800   2.000E-01   *.***E-03   *.****E-06
C
m2339 2003 1                     $ pure He-3 for rxn rate calculation
m2340 2003 5.0E+01 1001 4.620E+02 6012 5.9E+02 9019 1.744E+03 18000 4.870E+02
      gas=1
m2341 2003 1.0E+02 1001 4.620E+02 6012 5.9E+02 9019 1.744E+03 18000 4.870E+02
      gas=1
m2342 2003 3.0E+02 1001 4.620E+02 6012 5.9E+02 9019 1.744E+03 18000 4.870E+02
      gas=1
m2343 2003 2.5E+01 1001 4.620E+02 6012 5.9E+02 9019 1.744E+03 18000 4.870E+02
      gas=1
m2344 2003 *.*E+0* 2004 *.***E+0* 1001 *.*E+0* 6012 *.***E+0* 18000 *.***E+0*
      9019 *.***E+0* gas=1
C ..... End lanl_gas.trf ..........................................
```

poly_3221.trf

```
C ... Begin poly_3221.trf .........................................
c  polyethelene   density .92-.95 gm/cc
m3221      1001 2 6000 1
           nlib .66c
mt3221     poly.01t
C End poly_3221.trf
C ..... End poly_3221.trf .........................................
```

air_2201_lineC.trf

```
C ... Begin air_2201_lineC.trf ................................................
C Air at LANSCE line 'C'
C 2120m, 21C, 10% Rel. Humidity
C Atmosphere density 9.264E-04 g/cc
m2201 pnlib=99u plib=04p elib=03e hlib=.24h gas=1
        1001    3.31142E-03
        1002    4.96787E-07
        2003    3.58769E-12
        2004    2.61875E-06
        6012    1.87820E-04
        6013    2.08900E-06
        7014    7.77545E-01
        7015    2.88760E-03
        8016    2.10878E-01
        8017    8.45543E-05
        8018    4.22771E-04
       10020    8.23427E-06
       10021    2.45718E-08
       10022    8.41811E-07
       18036    1.57304E-05
       18038    2.94070E-06
       18040    4.64910E-03
       36078    1.99405E-09
       36080    1.28189E-08
       36082    6.60884E-08
       36083    6.55187E-08
       36084    3.24745E-07
       36086    9.85629E-08
       54124    4.34792E-11
       54126    3.91313E-11
       54128    8.30453E-10
       54129    1.14785E-08
       54130    1.78265E-09
       54131    9.21760E-09
       54132    1.16959E-08
       54134    4.52184E-09
       54136    3.86965E-09
C #       mx2201:n    mx2201:p    mx2201:h
C  1001       j
C  1002       j
C  2003
C  2004
C  6012
C  6013
C  7014
C  7015
C  8016
C  8017
C  8018
C 10020
C 10021
C 10022
C 18036
C 18038
C 18040
C 36078
C 36080
C 36082
C 36083
C 36084
C 36086
C 54124
C 54126
C 54128
C 54129
```

```
C 54130
C 54131
C 54132
C 54134
C 54136
C ..... End air_2201_lineC.trf ................................................
```

concrete_lanl_m5.trf

```
C ... Begin concrete_lanl_m5.trf ..............................................
c concrete (los alamos)    density = 2.3 gm/cc
m5      pnlib=99u  hlib=.24h
       1001    8.47509e-2
       1002    1.27145e-5
       8016    6.02636e-1
       8017    2.41634e-4
       8018    1.20817e-3
      11023    9.47250e-3
      12024    2.36833e-3
      12025    2.99826e-4
      12026    3.30108e-4
      13027    2.48344e-2
      14028    2.23067e-1
      14029    1.12949e-2
      14030    7.49766e-3
      19000    6.85513e-3
      20040    1.98543e-2
      20042    1.42511e-4
      20043    2.76491e-5
      20044    4.27229e-4
      20046    8.19232e-7
      20048    3.82991e-5
      26054    2.74322e-4
      26056    4.26455e-3
      26057    9.76401e-5
      26058    1.30187e-5
mx5:p       0 j j j j j j j j j j j j j model
            j j j j j j j j j j
mx5:h    j j j 8016 8016 model model model model j
         j j j model j 20040 20040 20040 20040 20040
         j j j j
C ..... End concrete_lanl_m5.trf ...............................................
```

304.trf

```
C ... Begin 304.trf ............................................................
c  SS304  8.03 gm/cc
m1     6000     -0.08
      25055     -2.00
      15031     -0.045
      16032     -0.030
      14028     -0.75
      24052    -19.0
      28058    -10.0
       7014     -0.10
      26056    -67.995
C ..... End 304.trf .............................................................
```

cf252_unbiased.trf

```
C ... Begin cf252_unbiased.trf ................................................
C Cf-252 Neutron Energy Spectrum
#      si1      sp1
        A        D
       0.199     0
       0.20    1.983E-02
       0.21    2.017E-02
       0.22    2.050E-02
       0.23    2.081E-02
       0.24    2.111E-02
       0.25    2.139E-02
       0.26    2.166E-02
       0.27    2.191E-02
       0.28    2.216E-02
       0.29    2.239E-02
       0.30    2.261E-02
       0.31    2.282E-02
       0.32    2.302E-02
       0.33    2.321E-02
       0.34    2.339E-02
       0.35    2.356E-02
       0.40    2.431E-02
       0.50    2.530E-02
       0.60    2.581E-02
       0.70    2.595E-02
       0.80    2.583E-02
       0.90    2.551E-02
       1.00    2.504E-02
       1.10    2.445E-02
       1.20    2.377E-02
       1.30    2.304E-02
       1.40    2.226E-02
       1.50    2.145E-02
       1.60    2.063E-02
       1.70    1.980E-02
       1.80    1.897E-02
       1.90    1.814E-02
       2.00    1.733E-02
       2.10    1.654E-02
       2.20    1.576E-02
       2.30    1.500E-02
       2.40    1.427E-02
       2.50    1.356E-02
       2.60    1.287E-02
       2.70    1.221E-02
       2.80    1.158E-02
       2.90    1.097E-02
       3.00    1.039E-02
       3.10    9.836E-03
       3.20    9.304E-03
       3.30    8.797E-03
       3.40    8.314E-03
       3.50    7.854E-03
       3.60    7.416E-03
       3.70    7.000E-03
       3.80    6.605E-03
       3.90    6.230E-03
       4.00    5.874E-03
       4.10    5.537E-03
       4.20    5.218E-03
       4.30    4.916E-03
       4.40    4.630E-03
       4.50    4.359E-03
       4.60    4.104E-03
       4.70    3.862E-03
```

```
        4.80    3.634E-03
        4.90    3.419E-03
        5.00    3.215E-03
        5.50    2.359E-03
        6.00    1.724E-03
        6.50    1.256E-03
        7.00    9.117E-04
        7.50    6.603E-04
        8.00    4.771E-04
        8.50    3.441E-04
        9.00    2.477E-04
        9.50    1.781E-04
       10.00    1.278E-04
       10.50    9.166E-05
       11.00    6.564E-05
       11.50    4.696E-05
       12.00    3.356E-05
       12.50    2.397E-05
       13.00    1.710E-05
       13.50    1.219E-05
       14.00    8.687E-06
       14.50    6.186E-06
       15.00    4.402E-06
C ..... End cf252_unbiased.trf ..............................................
```

Appendix B: Californium-252 neutron source

# B.1: Characteristics of Cf-252 neutron emission

The majority of experiments presented herein used various Californium-252 neutron sources at Los Alamos National Laboratory. Cf-252 is produced in nuclear reactors and has a half-life of 2.645 years. Cf-252 undergoes alpha decay with a branching ratio of 96.91% and spontaneous fission with a branching ratio 3.09% [19]. The average neutron multiplicity for fission events is 3.76 [20, 21]. The mass neutron emission rate for a fission source is given by:

$$\mu = \frac{\ln 2}{t_{1/2}} \cdot \frac{f \bar{v} N_A}{A},$$

where $t_{1/2}$ is the half-life of the isotope, f is the fission branching ratio, $\bar{v}$ is the average neutron multiplicity, A is the atomic mass, and N_A is Avogadro's number. For Cf-252, the mass neutron emission rate is 2.314×10^6 $n \cdot s^{-1} \cdot \mu g^{-1}$ [22]. The energy of the emitted neutrons is well approximated by a Maxwellian distribution having average energy $\bar{E} = 2.13 MeV$: $N(E) = \sqrt{E} \exp[-E/T]$, where the temperature $T = 2/3 \bar{E} = 1.42 MeV$ [23].
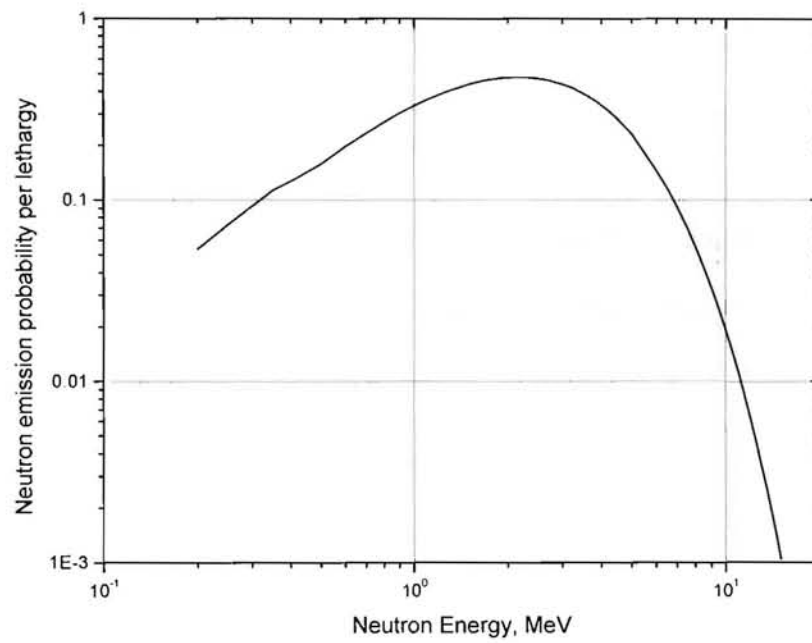
Figure 60: Cf-252 neutron energy spectrum

B.2: Cf-252 source aging effects

The activity of a Cf-252 source does not obey exponential decay over an indefinitely long period of time. This is due to the buildup of secondary neutron emitters that have lifetimes longer than Cf-252. Two other nuclei in particular begin to dominate as a Cf-252 source ages: Cf-250, which is usually present as an impurity from the manufacturing process, and Curium-248, which is the product of Cf-252 alpha decay. Cf-250 has a half-life of 13.1 years and a neutron emission rate of 1.72×10^4 n$\cdot$s$^{-1}\cdot\mu$g^{-1}, while Cm-248 has a half-life of 340,000 years and an emission rate of 40.9 n$\cdot$s$^{-1}\cdot\mu$g^{-1}. Both of these radionuclides have low emission rates compared to Cf-252 and their activities are negligible for the first few decades of a Cf-252 source's lifetime. However, at least one of these isotopes always becomes a factor as the source weakens after many half-lives. The increase in the effective activity of the Cf-252 source by these isotopes is summarized in Table 5:

	Years to reach fractional increase, by isotope		
Fractional Increase in Cf-252 activity	Cm-248	Cf-250 at 1% initial impurity level	Cf-250 at 0.1% initial impurity level
10%	33.1	36.2	47.2
100%	41.9	47.2	58.2

Table 5: Effect of secondary isotopes on Cf-252 source activity

Cm-248 is always present in a Cf-252 source, as it is a natural product of the Cf-252 alpha decay[31]. Therefore, Cm-248 buildup establishes the practical limit on

.

---

[31] The half-life of Cm-248 is essentially infinite relative to human lifetime, and as 96.91% of the original Cf-252 ultimately becomes Cm-248 through alpha decay, one can consider Cm-248 to yield a constant terminal activity of an extinguished Cf-252 source of 39.6 n$\cdot$s$^{-1}\cdot\mu$g$^{-1}_{Cf252}$.

UNCLASSIFIED – ADC Review by Alexander Saunders, P-25, on 3/23/2009

the amount of time a Cf-252 source can be used before buildup effects must be considered. The effective lifetime when simple exponential decay can be used is roughly 30 years. Furthermore, for sources older than about 35 years, one should make a serious attempt to determine the initial quantity of Cf-250 that was present. This information is not always available and thus, for many Cf-252 sources, 35 years represents the maximum age that the original calibration data can be considered valid. In theory, the amount of Cf-250 present could be determined if the source activity were monitored over several years. However, in practice this determination would likely be more troublesome and expensive than simply obtaining a new source. The oldest Cf-252 source used in these experiments was 21 years old; thus simple exponential decay still applies.